ABSTRACT

JENSEN, MARK JAY. Fast Neutron Capture by ^{13}C. (Under the direction of D.R. TILLEY.)

The $^{13}C(n,\gamma_0)^{14}C$ reaction yield was measured at 90° for neutron lab (excitation) energies from 5.6 (13.4) to 14 (21.2) MeV. Angular distributions of cross section and analyzing power were measured at five energies, E_n = 7.75, 9.2, 10.2, 11 and 12 MeV. The cross section was measured over an angular range of 30°-35° to 150°. The analyzing power was measured over an angular range of 45° to 140°. The target sample consisted of 32.4 g of 96.4 % isotopically enriched ^{13}C powder. The finite-geometry corrections were applied to the data. The angular distributions were expanded in terms of Legendre functions. They were also analyzed in terms of E1-E2 and E1-E2-M1 transition matrix elements. Existing shell model calculations are in good agreement with the mean energy and standard deviation of the T=0 component of the dipole absorptive strength distribution. A direct-semidirect model fit to the data suggests the presence of an isoscalar E2 resonance.

FAST NEUTRON CAPTURE BY ^{13}C

by

Mark Jay Jensen

A thesis submitted to the Graduate Faculty of
North Carolina State University
in partial fulfillment of the
requirements for the Degree of
Doctor of Philosophy

DEPARTMENT OF PHYSICS

RALEIGH

1 9 8 1

APPROVED BY:

Chairman of Advisory Committee

BIOGRAPHY

Name: Mark J. Jensen

Birth: May 17, 1949
Corvallis, Oregon

Education: B.S. Computer Science with Honors, May, 1970
North Carolina State University

M.S. Nuclear Engineering, May, 1978
North Carolina State University
Thesis: Optimum Design of Alpha-Particle Transmission, Gas Composition and Density Gauges

Positions: Research Assistant, 1977 - 1981
Triangle Universities Nuclear Laboratory
Duke Station, Durham, NC

Teaching Assistant, 1973 - 1977
Physics and Nuclear Engineering Departments
North Carolina State University
Raleigh, NC

Programmer, 1973
Institute of Modern Procedures
Washington, DC

Specialist/5, Systems Programmer, 1970 - 1973
U.S. Army Security Agency
Arlington, VA

Information Systems Designer, 1970
Western Electric Co., Inc.
Burlington, NC

Consultant, 1969 - 1970
N.C. Academy of General Practitioners
Research Triangle Park, NC

Junior Programmer, 1969 - 1970
International Business Machines, Corp.
Research Triangle Park, NC

Lab Instructor, 1968 - 1969
Computer Science Department
North Carolina State University
Raleigh, NC

Memberships:

American Physical Society
Association for Computing Machinery
National Society of Professional Engineers
Sigma Pi Sigma (Physics Honor Society)
Software Tools Users Group
Upsilon Pi Epsilon (Computer Science Honor Society)

Publications and Abstracts:

Angular Distribution Measurements for the $^{40}Ca(n,\gamma)^{41}Ca$ Reaction.
with S.A. Wender, N.R. Roberson, H.R. Weller, M. Potokar and D.R. Tilley
Bul. Am. Phys. Soc. 23 (1978) 507.

E2 Strength in the GDR Region Observed with Polarized Neutron Capture on ^{40}Ca.
with D.R. Tilley, S.A. Wender, N.R. Roberson and H.R. Weller.
Bul. Am. Phys. Soc. 24 (1979) 646.

Fast Neutron Capture Studies of the GDR Region of ^{15}N.
with S.A. Wender, M. Potokar, N.R. Roberson, H.R. Weller and D.R. Tilley.
Bul. Am. Phys. Soc. 24 (1979) 646.

Polarized-Neutron Capture in the Giant-Resonance Region of ^{41}Ca.
with D.R. Tilley, H.R. Weller, N.R. Roberson, S.A. Wender and T.B. Clegg.
Phys. Rev. Lett. 43 (1979) 609.

Proposed Computing Facilities for Triangle Universities Nuclear Laboratory.
with C.R. Gould, N.R. Roberson, S.E. Edwards, and S.A. Wender.
IEEE Tran. Nucl. Sci. 26 (1979) 4373.

Radiative Capture of Polarized Neutrons on ^{13}C.
with D.R. Tilley, S.A. Wender, N.R. Roberson and H.R. Weller.
Bul. Am. Phys. Soc. 25 (1980) 603.

Neutron Capture in the Giant Resonance Region of ^{14}C.
with D.R. Tilley, S.A. Wender, N.R. Roberson and H.R. Weller.
in Giant Multipole Resonances.
Fred E. Bertrand, Ed.
Harwood Academic Publishers, New York, 1980, 447.

TABLE OF CONTENTS

1 THEORETICAL BACKGROUND

1-a Photonuclear Review. The nuclear photoabsorption cross section as a function of photon energy can be divided into three regions. See Figure 1-1 for a schematic representation of its general features. In region 1 the photon energy is less than the binding energy of a particle (neutron or proton) and the nuclear levels are narrow. In region 2 the photon energy is greater than the particle binding energy, E_B, but there is still structure in the cross section. In region 3 the cross section is smooth. Very low energy γ rays can only interact with the nucleus as a whole. This process is called Thomson scattering. Photons with higher energies can excite the nucleus to a particular level. In region 2 photons with an energy greater than the particle binding energy can eject a proton or a neutron from the nucleus. In this region the nuclear levels broaden and blend together so that the states loose their individuality. However, just above the particle binding energy, region 2, the individual states are still narrow enough to produce structure in the photoabsorption cross section. For some light nuclei region 2 may contain the majority of the photoabsorption strength [Full62].

The absorption cross section in region 3, where the nuclear levels have blended together, depends upon the shape and size of the nucleus and not upon the nature of any nuclear level. For example, in heavy nuclei the center of this giant resonance is given by ~ 80 $A^{-1/3}$ MeV. In light nuclei the center of the strength is ~ 20 MeV. The widths of these resonances vary from three to ten MeV [Hayw70]. The majority of

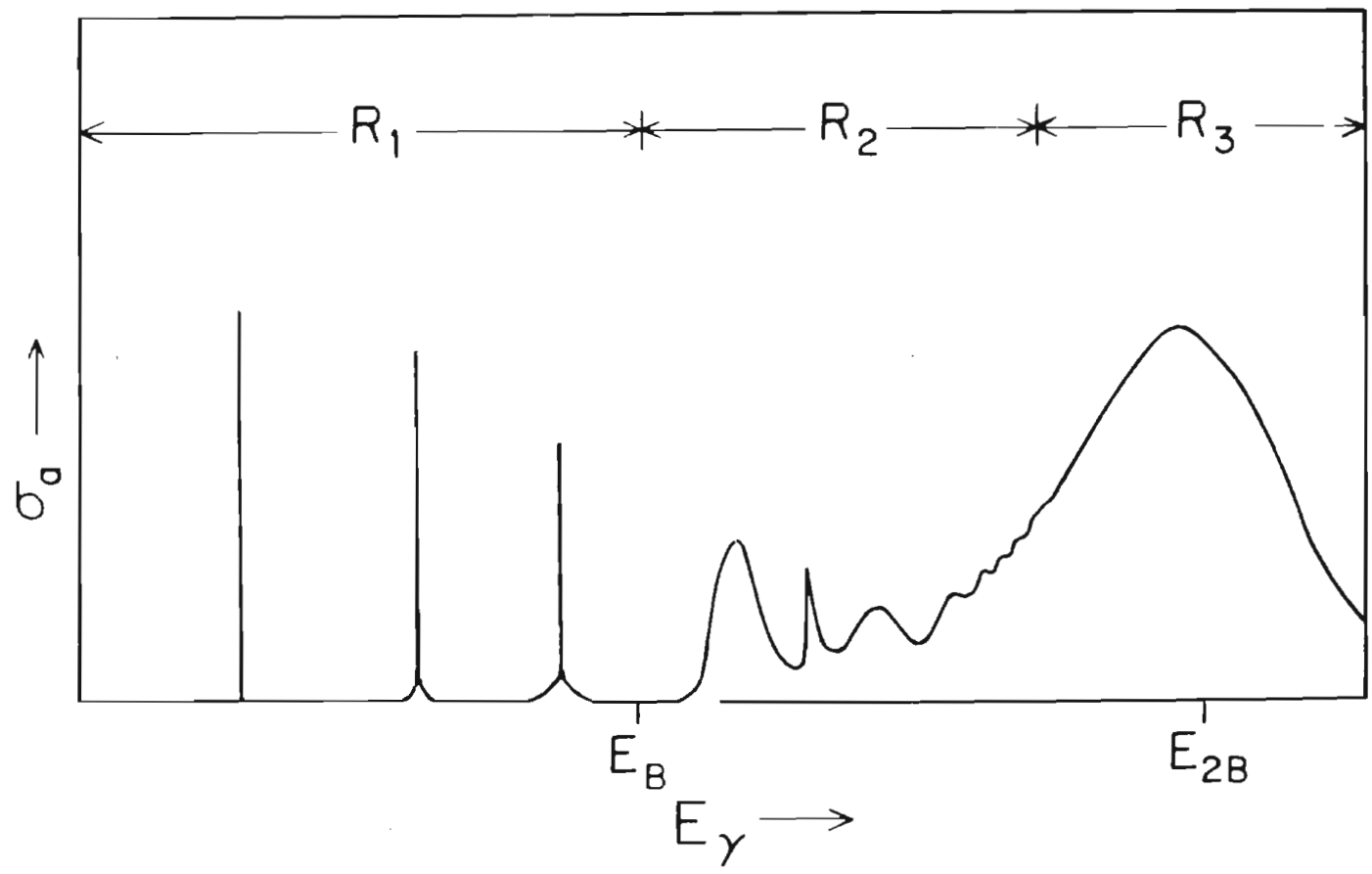

Figure 1-1 The photoabsorption cross section for an ideal nucleus. The three regions are described in the text.

the cross section is electric dipole in nature as can be seen from the measured angular distributions of cross section. This giant dipole resonance (GDR) exhausts the majority of the expected electric dipole strength in the nucleus. The classical electric dipole sum rule [Hayw70], the measure of photoabsorption, is given in Equation 1-1.

1-1
$$\int \sigma_{\gamma}(E1)\, dE_{\gamma} = 60 \frac{N\,Z}{A} \quad mb \cdot MeV$$

Although the majority of the absorption strength is electric dipole (E1), higher multipolarities also exist. The amount and location of electric quadrupole (E2) strength was of particular interest in this study.

The γ rays encountered in nuclear physics studies with less than 100 MeV, can be separated into different multipolarities [Pres75]. Each γ-ray quantum has an angular momentum, $\underline{L}\hbar$, where $|\underline{L}|^2 = L(1+1)$ and where L is a positive integer. The order of the multipolarity is given by 2^L. Thus for L = 1, the radiation is referred to as dipole radiation. Likewise, for L = 2 and 3 the radiation is labeled quadrupole and octupole respectively. Each multipole order can further be subdivided by the parity change into two classes, electric and magnetic. If the nuclear change in parity can be characterized by $(-1)^L$, the radiation is labeled electric. If the nuclear change in parity can be characterized by $(-1)^{L+1}$, the radiation is labeled magnetic. The γ-ray multipolarity

is generally abbreviated by the parity change and by the angular momentum. For example, electric dipole radiation is abbreviated as E1, magnetic dipole radiation as M1, and electric quadrupole as E2.

Some features of the giant resonance can be illustrated by the vibration of the nucleus [Hann80]. In isoscalar electric modes, the protons and the neutrons vibrate in phase, i.e., the nucleus vibrates as a whole. In isovector electric modes, the protons and the neutrons vibrate out of phase. For the isovector magnetic mode, the protons with spin up and the neutrons with spin down vibrate out of phase with the protons with spin down and the neutrons with spin up. Figure 1-2 shows a schematic representation of the vibrations for isovector electric dipole (E1), isoscalar electric quadrupole (E2) and isovector magnetic dipole (M1).

As the gross shape of the giant resonances became better understood through numerous experimental and theoretical studies, interest shifted toward the structure of the resonance. Individual channel cross sections instead of the total absorption cross section provide more stringent tests of the models used to describe the giant resonances. Many different reactions other than photon absorption have been used to study giant resonances, for example, electron scattering, inelastic proton and alpha particle scattering, heavy ion scattering, and charge exchange reactions [Bert80].

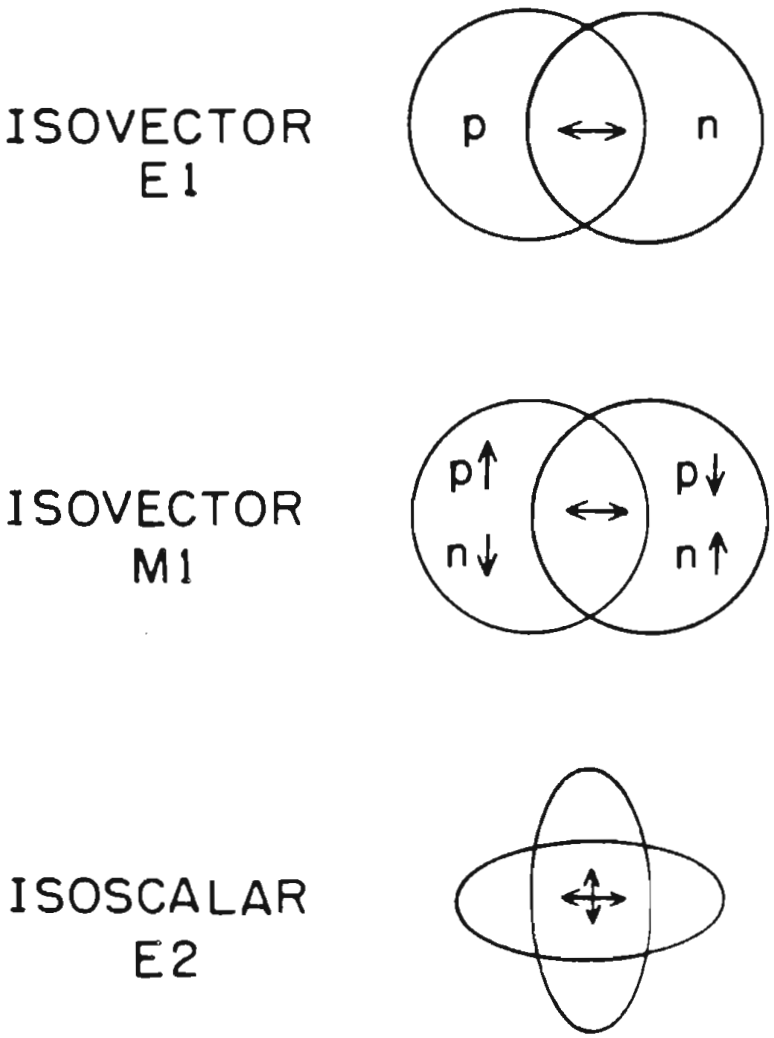

Figure 1-2 Schematic representations of some giant nuclear oscillations.

Radiative capture, e.g., (n,γ_0) or (p,γ_0), also is useful in that it examines a single channel of the giant resonance. The radiative capture process is just the time-reversed particle-emission process, and the cross section for either process may be converted to the other through detail balance [Hayw70], see Equation 3-2. Indeed by measuring radiative capture to an excited state in the resultant nucleus, one can study photoabsorption by an excited nucleus, which is impossible to measure directly. Capture reactions initiated by polarized beams of protons are a good tool in probing the E1 components of the giant resonance and in measuring the non-collective part of the E2 components.

The capture process can be decomposed into two parts [Brow64]: a collective (semidirect) part illustrated in Figure 1-2 and a non-collective (direct) part where the incident particle falls from the continuum into the nuclear potential well and the γ ray is emitted without the nuclear vibrations discussed above. The direct capture cross section is proportional to the square of the recoil effective charge, ε_L [Hayw70]. For E1 radiation from proton capture, $\varepsilon_{1,p} = N/(1+A)$, and from neutron capture, $\varepsilon_{1,n} = -Z/(1+A)$, i.e., both effective charges are approximately equal. However for E2 radiation, $\varepsilon_{2,p} = (A^2+Z)/(1+A)^2$ and $\varepsilon_{2,n} = Z/(1+A)^2$. The direct E2 radiation from proton capture will be significantly enhanced over that of neutron capture. This direct E2 radiation must be removed from proton capture data before the collective electric quadrupole (E2) contribution can be studied. In neutron capture, on the other hand, this direct E2

radiation may safely be ignored. This outstanding advantage of neutron capture motivated this capture study of $^{13}C(n,\gamma_0)^{14}C$.

The Triangle Universities Nuclear Laboratory (TUNL) capture group has performed successful polarized, proton beam capture studies [Wel180] on $^{13,14}C$, ^{30}Si, ^{88}Sr, $^{54,56,58}Fe$ and ^{59}Co. The first neutron capture measurements at TUNL were conducted with a target of ^{40}Ca. Angular distributions of cross section for neutron capture on ^{40}Ca were measured [Wel178, Wend78] and analyzed in terms of a direct-semidirect model, §1-d. However the angular distribution of cross section alone does not contain enough information to obtain the transition matrix elements, §1-b, desired. Therefore, the first fast polarized neutron beam capture measurements was conducted with a target of ^{40}Ca [Jens79]. The angular distributions of cross section and analyzing power, §4-a, for capture on ^{40}Ca were measured. Transition matrix elements were extracted, but the $^{40}Ca(n_{pol},\gamma_0)^{41}Ca$ reaction has too many unknowns to be determined without the direct-semidirect model being used to eliminate some of the transition matrix elements from the analysis.

The $^{13}C(n,\gamma_0)^{14}C$ reaction was chosen as the second fast polarized neutron beam reaction for several reasons: (1) There was a possibility of doing a model independent analysis of the data. (2) Proton capture to the isobaric analogue of the ground state in ^{14}C, i.e., $^{13}C(p_{pol},\gamma_1)^{14}N^*$ (0^+ T=1), had previously been measured [Turn78, Turn80], and would allow the comparison of two different isospin components of the giant dipole resonance. (3) Shell model calculations

of Vergados [Verg75] and Kissner and others [Kiss73, Kiss79] suggested that in the energy region available, there should be observable absorptive strength. (4) The cost of isotopically separated ^{13}C dropped to ~ $70 per gram, making a large, > 30 g, target affordable.

1-b Transition Matrix Elements. The transition matrix elements used in the capture process describe the transition of an unbound particle in the continuum to a bound state in the resultant nucleus. Refer to Figure 1-3 for the following discussion. The j-j coupling notation is from E. Hayward [Hayw70]. The incident particle with spin $\underline{s}$ and orbital angular momentum $\underline{l}$ is captured by a nucleus with spin $\underline{I}_0$. The angular momenta $\underline{l}$ and $\underline{s}$ couple to form $\underline{j}$ and then $\underline{j}$ and $\underline{I}_0$ couple to form the spin of the excited state, $\underline{I}_k$. This state decays through the emission of a γ ray with multipolarity L to the final state with spin $\underline{I}_f$. This transition must comply with the triangular selection rule, $| I_k - I_f | \leq L \leq I_k + I_f$. The matrix elements for a particular multipolarity are labeled with "l" and "j", the incident particle's orbital angular momentum and spin.

As an example, the method for determining the allowed spins and angular momentum for E2 radiation in the $^{13}C(n,\gamma_0)^{14}C$ will be detailed below, see Figure 1-4. Working backwards, the ground state of ^{14}C has a spin and parity of 0^+. The triangular selection rule yields the allowable values for the spin, I_k, and the parity of the excited state. For E2 radiation, L = 2 so that $| I_k - 0 | \leq 2 \leq I_k + 0$ or $I_k = 2$. The parity of the excited state is determined from the previously mentioned electric transition characterization of $(-1)^L = (-1)^2 = 1$.

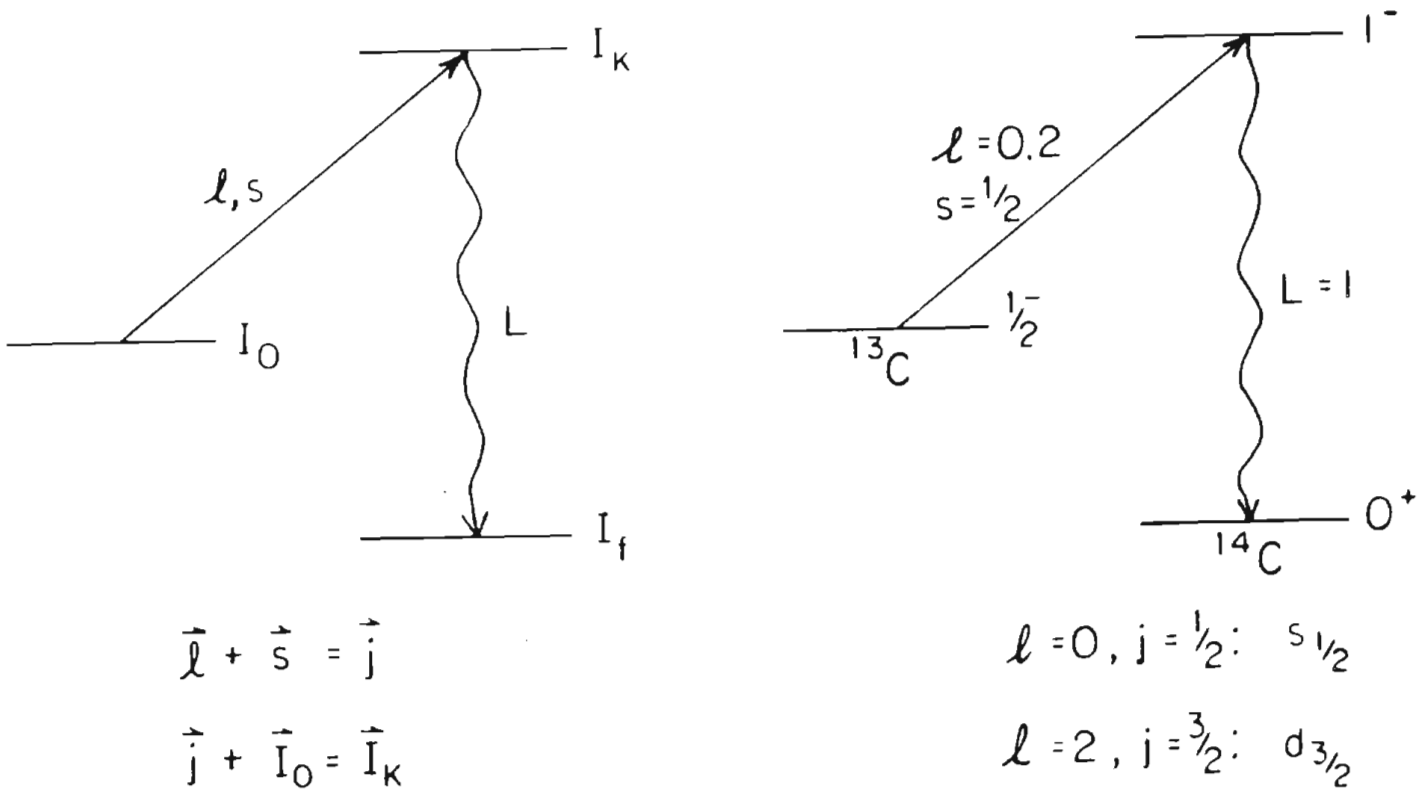

Figure 1-3 Schematic representation of radiative capture in the j-j coupling scheme. The E1 transition j-j coupling scheme for the $^{13}C(n,\gamma_0)^{14}C$ reaction.

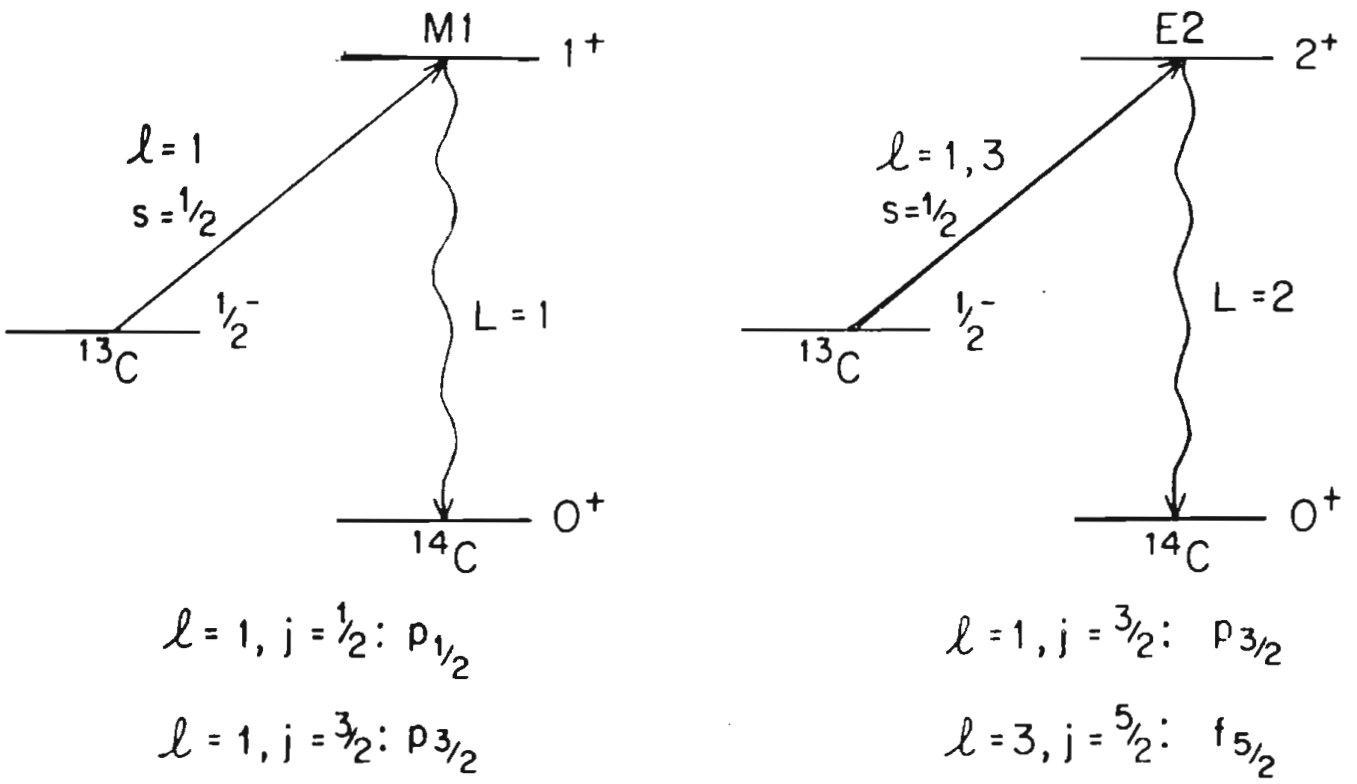

Figure 1-4 The M1 and E2 transition j-j coupling scheme for the $^{13}C(n,\gamma_0)^{14}C$ reaction.

Thus the excited state must have the same parity as that of the ground state, i.e., $\pi_k = +1$. The allowable particle spins are determined from $\underline{j} + \underline{I}_0 = \underline{I}_k$, where $I_0 = 1/2$ is the ground state spin of the ^{13}C target. Thus $| \underline{j} | + 1/2 = 2$ implies that $j = 3/2$ and $5/2$. The allowable particle orbital angular momenta are determined from $\underline{l} + \underline{s} = \underline{j}$, where $\underline{s}$ is 1/2 for a neutron or proton. Hence "l" may be 1 and 3. The E2 transition matrix elements are labeled $p_{3/2}$ and $f_{5/2}$.

Glavish [Glav74] and more recently Seyler and Weller [Sey179] have shown that the measured angular distributions of γ-ray cross section and analyzing power may be related to complex valued transition matrix elements. In the case of the $^{40}Ca(n_{pol},\gamma_0)^{41}Ca$ reaction the $7/2^-$ spin and parity of the ground state of ^{41}Ca resulted in three matrix elements for E1 radiation and five matrix elements for E2 radiation. The fifteen unknowns (eight amplitudes and seven relative phases) make even an E1-E2 model independent analysis impossible. In the case of the $^{13}C(n_{pol},\gamma_0)^{14}C$ reaction the $1/2^-$ spin and parity of ^{13}C results in only two E1 and two E2 matrix elements. M1 radiation has been ignored because it is expected to be concentrated at the lower energies [Uber71]. The presence of only seven unknowns results in the possibility of a model independent E1-E2 analysis of the $^{13}C(n_{pol},\gamma_0)^{14}C$ reaction angular distributions.

1-c Comparison of Isospin Components of the GDR. Just as the γ-ray transitions can be characterized by their multipolarities, they can also be characterized by the isospin changes in the nucleus they affect. Warburton and Wenesner [Warb69] develop the isospin selection rules for electromagnetic transitions. Isospin, T, like spin angular momentum, is a vector with a z-component of $T_z = (N - Z) / 2$. Any state within a nucleus thus has the same T_z, and thus for γ-ray transitions, $\Delta T_z = 0$. Another isospin selection rule states that $\Delta T = 0$, and ± 1. The exception to this last selection rule is that $\Delta T = 0$, E1 transitions in self-conjugate nuclei are forbidden. For an example, see Figure 1-5, in ^{14}C, $T_z = 1$. The ground state of a nucleus has $T = T_z$. The allowed isospin transitions are $\Delta T = 0$ and 1. $\Delta T = -1$ is forbidden because the resulting T = 0 isospin vector cannot have a projection of $T_z = 1$.

To compare the strength of the $^{13}C(n,\gamma_0)^{14}C$ reaction to the strength of the $^{13}C(p,\gamma_1)^{14}N^*$ (0^+ T=1) reaction one can use the isospin arguments of Fallieros and Goulard [Fal170] and Vergados [Verg75]. The GDR built on the ground state of ^{14}C and the first excited state in $^{14}N^*$ can be decomposed into two isospin components, see Figure 1-5. The isospin components of $^{14}N^*$ are T=0 and T=2, of which only the T=0 component is populated by the $^{13}C(p,\gamma_1)^{14}N^*$ (0^+ T=1) reaction. The isospin components of ^{14}C are T=1 and T=2, of which only the T=1 component is populated by the $^{13}C(n,\gamma_0)^{14}C$ reaction. Thus one can compare the T=0 and the T=1 strength.

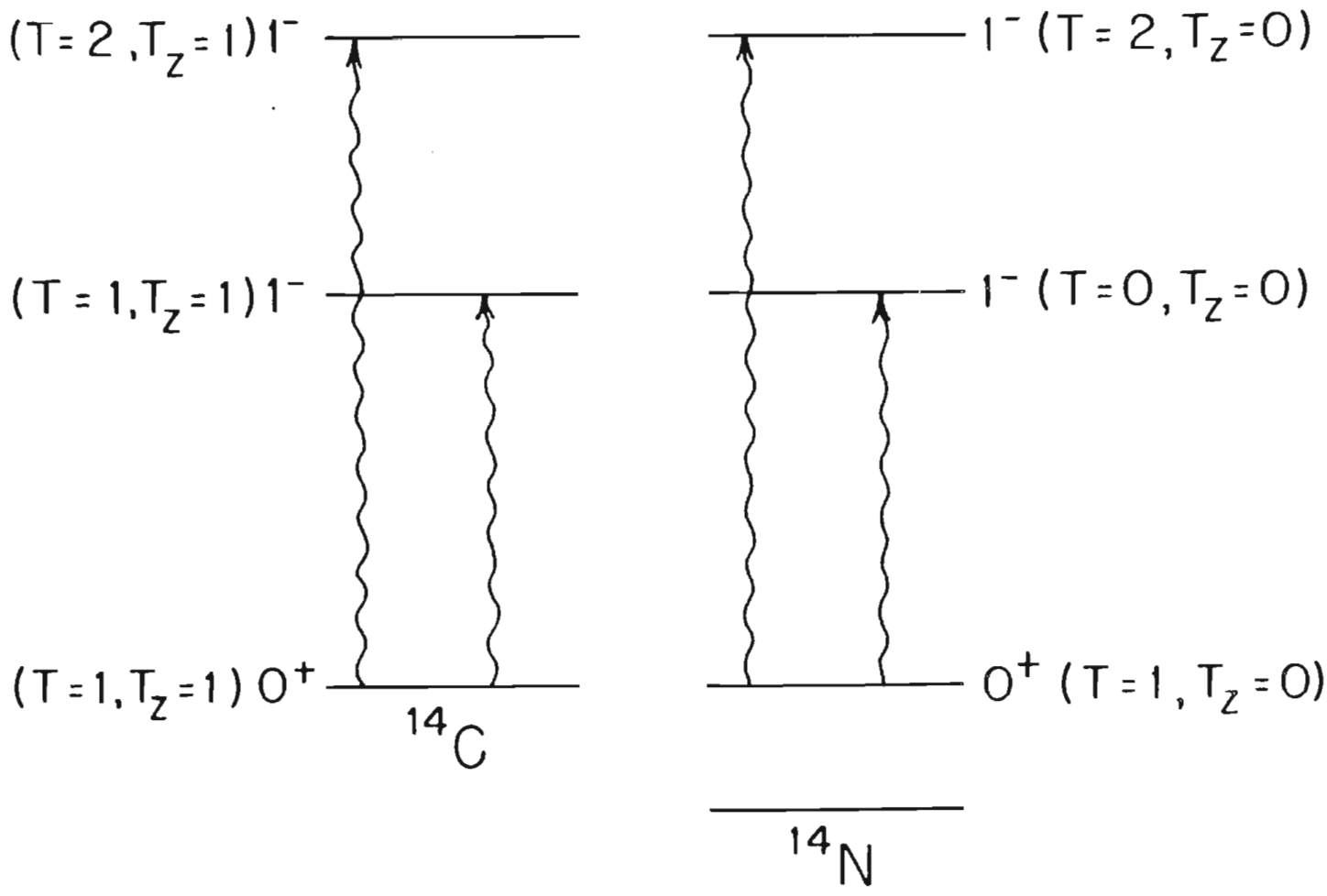

Figure 1-5 Isospin components of the giant dipole resonance built on the T=1 state in ^{14}C and $^{14}N^*$.

To determine the T=0 strength in $^{14}N^*$ one must calculate the ratio of the T=0 to the T=2 strength as shown in Equation 1-2 [Fall70].

1-2 $$\frac{S_0(^{14}N^*)}{S_2(^{14}N^*)} = \frac{1}{2}\,\frac{|b_0|^2}{|b_2|^2}$$

The strength in the T' component of the GDR is $S_{T'}$, and b_0 and b_2 are reduced matrix elements. Fallieros gives an estimate (Equation 1-3) of the ratio of the reduced matrix elements.

1-3 $$\frac{|b_0|^2}{|b_2|^2} = \frac{1 + 2\alpha}{1 - \alpha} = 2; \text{ where } \alpha = 3/2\ A^{-2/3}$$

This results in a ratio of strengths, S_0/S_2, of one.

The ratio of the T=2 to the T=1 strength in ^{14}C is given by similar arguments in Equation 1-4.

1-4 $$\frac{S_2(^{14}C)}{S_1(^{14}C)} = \frac{1 - \alpha}{1 + \alpha} = 0.6$$

The S_2 strength may be directly expressed in terms of the reduced matrix element, b_2, and an isospin Clebsch-Gordan coefficient [Verg75] as shown in Equation 1-5.

1-5 $$S_2 = \langle T\ T_z\ 1\ 0 |\ 2\ T_z \rangle^2\ |b_2|^2$$
$$S_2(^{14}C) = \langle 1\ 1\ 1\ 0 |\ 2\ 1 \rangle^2\ |b_2|^2 = 1/2\ |b_2|^2$$
$$S_2(^{14}N^*) = \langle 1\ 0\ 1\ 0 |\ 2\ 0 \rangle^2\ |b_2|^2 = 3/2\ |b_2|^2$$

Only the ratios are of interest, therefore $|b_2|^2 = 1$. Thus $S_0(^{14}N^*) = 0.67$ and $S_1(^{14}C) = 0.83$ yielding 1.24 as the S_1/S_0 ratio.

This S_0 and S_1 strength is the strength of the full GDR. One also needs to factor in the probability of forming the particle, neutron or proton. This is another pair of isospin Clebsch-Gordan coefficients as shown in Figure 1-6. The ratio of these coefficients is expressed in Equation 1-6.

$$1\text{-}6 \qquad \frac{\langle\, 1/2\ 1/2\ 1/2\ \ 1/2 \mid 1\ 1 \,\rangle^2}{\langle\, 1/2\ 1/2\ 1/2\ -1/2 \mid 1\ 0 \,\rangle^2} = \frac{1}{1/2} = 2$$

The ratio of the integrated cross sections, $\Sigma(^{14}C) \ / \ \Sigma(^{14}N^*) = 2.5$, is a factor of two larger than the strength ratio.

1-d Direct-Semidirect Model. One successful reaction model of fast nucleon capture is the direct-semidirect model [Brow64, Clem65a, Clem65b, Lush65]. The model decomposes the capture process into two components, direct (non-collective) and semidirect (collective). The direct part represents a single-step process in which a nucleon falls from the continuum into the potential well of the resultant nucleus and radiates the γ ray. The semidirect or collective part represents a two-step process in which a nucleon falls from the continuum into the potential well of the resultant nucleus exciting the nucleus into a collective state. The nucleus then decays, radiating the γ ray. The direct-semidirect reaction model allows one to calculate the radial transition matrix elements via

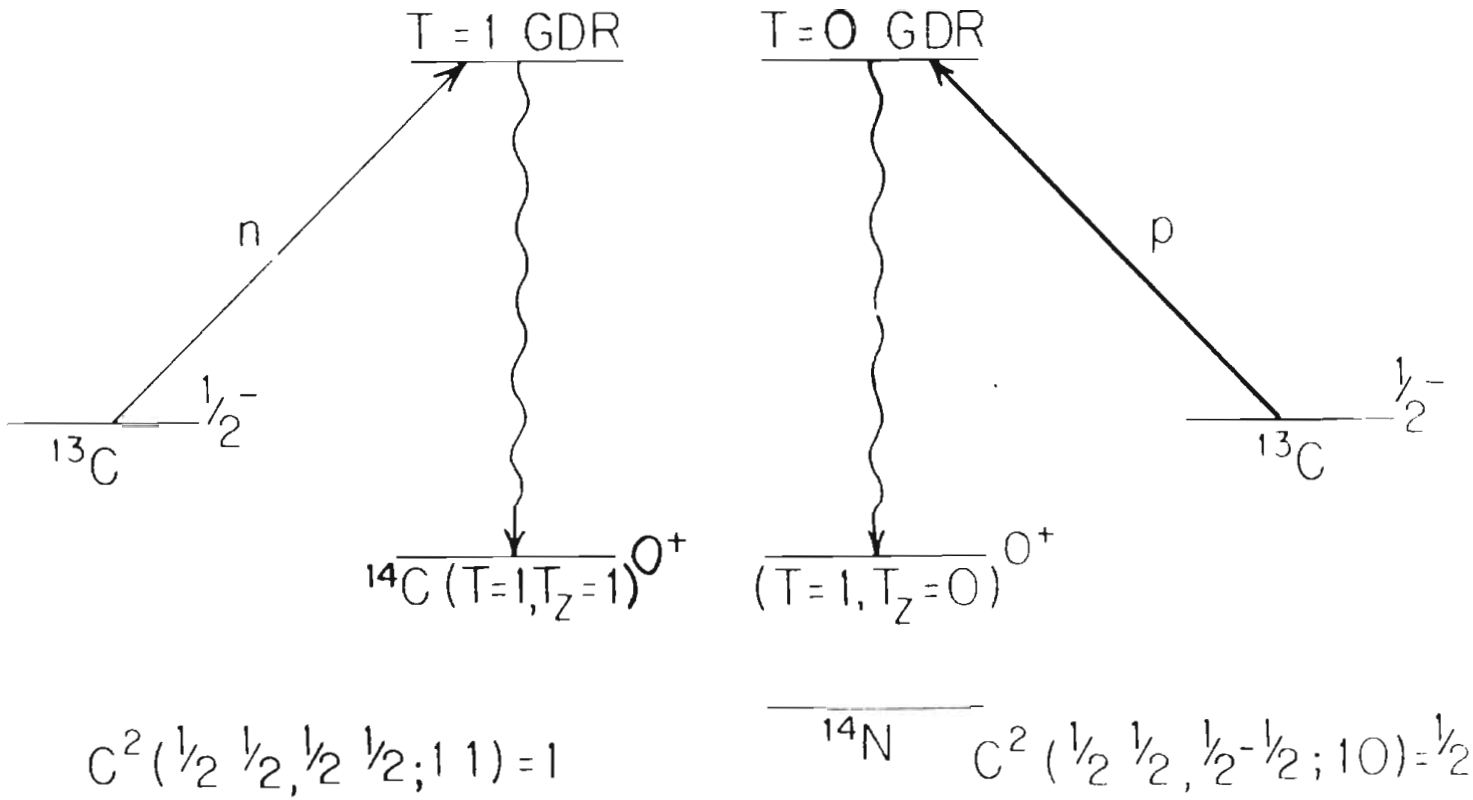

Figure 1-6 Isospin coupling coefficients for neutron and proton production from the giant dipole resonance built on the T=1 state in ^{14}C and $^{14}N^*$.

$$\langle \varphi_{n,l,j} \mid V \mid \chi_{l',j'} \rangle$$

where $\chi_{l',j'}$ is the continuum wave function of the incoming particle and $\varphi_{n,l,j}$ is the bound state wave function of the particle in the resultant nucleus. For a particular multipolarity the transition matrix elements are labeled with the quantum numbers of the incoming particle, e.g., in E1 radiation $d_{3/2}$ implies $l' = 2$ and $j' = 3/2$. The incoming wave function is obtained from the scattering wave function via an optical model. The bound particle wave function is obtained by solving the Schroedinger wave equation and iterating on the well depth until the particle has the correct binding energy.

For electric multipole radiation with the long-wavelength approximation [Pres75], the radial part of the operator V is generally decomposed [Poto77, Lika76] into the two terms found in Equation 1-7.

1-7
$$V = r^L + \frac{V_c^L(r)}{E_\gamma - E_r + 1/2\ i\ \Gamma_r}$$

For each multipolarity, L, the two terms are a direct part, r^L, and a semidirect part, the last term in Equation 1-7. $V_c^L(r)$ is the collective coupling function or the form factor. E_r is the position of the resonance and Γ_r is the width of the resonance. The position and width along with the form factor may be varied to fit the observed data.

1-e Shell Model. The shell model provides an alternate description of photoexcitation. The bound state shell model calculations involve construction of a Hamiltonian matrix, converting it into diagonal form, rejecting any spurious states, and matching the single particle level energies with known values [Bert72]. The shell model wave functions must be coupled with a reaction theory to account for the captured particle. From the shell model wave functions and the electromagnetic operators, the reduced transition probabilities, the B's, can be calculated with energy weighted sum rules. There are two shell model calculations for the A = 14 mass nuclei, one by Vergados [Verg75] and another by Kissner and others [Kiss73, Kiss79]. Both include $1\hbar\omega$ excitations and are E1 transition calculations. They differ in their choice of the Hamiltonian, Kuo-Lee for Vergados and Cohan-Kurath for Kissner. Vergados calculates the reduced transition probabilities, B(E1), for each E1 dipole transition. Kissner calculates the fraction of the sum rule strength for each E1 transition. In addition Kissner has coupled his shell model wave functions with an R-matrix theory to calculate the branching ratios and spreading widths of the dipole states.

2 EXPERIMENTAL EQUIPMENT AND METHODOLOGY

2-a Overview. The neutron is electrically neutral and makes an excellent nuclear probe. Its effects are not confounded by the nuclear Coulomb field as are the effects of protons and α particles. However, from an experimentalist's view, this attribute which makes the neutron a good nuclear probe also makes it more difficult to work with in the laboratory. Where protons can be made by ionizing hydrogen, neutrons must be made by a nuclear reaction, e.g., fission or a light ion reaction. Likewise protons may be shielded by a small amount of matter, but neutrons are not only exponentially attenuated, they may be scattered back into the room by scattering from the walls, ceiling or floor. Thus the experimental room becomes saturated with neutrons. The method of neutron production used here was the $^{2}H(d,n)^{3}He$ reaction, where the deuterium was kept in a gas cell, §2-b. It produces a larger neutron flux than alternative reactions and the neutrons are monoenergetic in the energy region measured.

There is no good spectrometer for energetic neutrons as the NaI and surface barrier detectors are good spectrometers for γ rays and protons. One method to measure the energy of neutrons is to measure the time it takes from when it is produced until when it is detected. If the distance which the neutron travelled is known, the neutron's velocity is known and hence its energy. This is the time-of-flight method. The time of neutron detection can be determined from the neutron detector. Knowing the time of production is more difficult. The solution to this problem is to chop the deuteron beam into packets

and then compress the packets into narrow pulses. Around ninety percent of the deuteron beam is chopped away. By detecting the deuteron beam packet just before it enters the gas cell of deuterium, the time of neutron production is known, and thus the neutron's energy. Also in using the $^{2}H(d,n)^{3}He$ reaction the neutron energy may be obtained via kinematics when the energy of the deuteron is known.

The detection of ten to twenty MeV γ rays is also difficult. The detection of these γ rays is generally handled by using large NaI crystals. The size of these detectors results in high cosmic ray count rates and also in high neutron background count rates. To reduce this background the detector is surrounded by an anticoincidence shield. The time-of-flight method may also be used to reduce this background count rate, §2-e.

Radiative capture cross sections are small, typically on the order of 10^{-6} b·sr^{-1}. Thus large targets are needed. Indeed, the gas cell, the target and the NaI detector are all large enough to preclude the use of point geometry assumptions. The effects of the size of the components of the system cannot simply be included in the analysis of the experimental results. These effects are deferred until §5.

2-b Neutron Beam Production. A pulsed deuteron beam was accelerated by the TUNL FN tandem Van de Graff and transported to a deuterium gas cell. The $^{2}H(d,n)^{3}He$ reaction was then used to produce a pulsed beam of neutrons. See Figure 2-1 for a schematic diagram of the experimental environment.

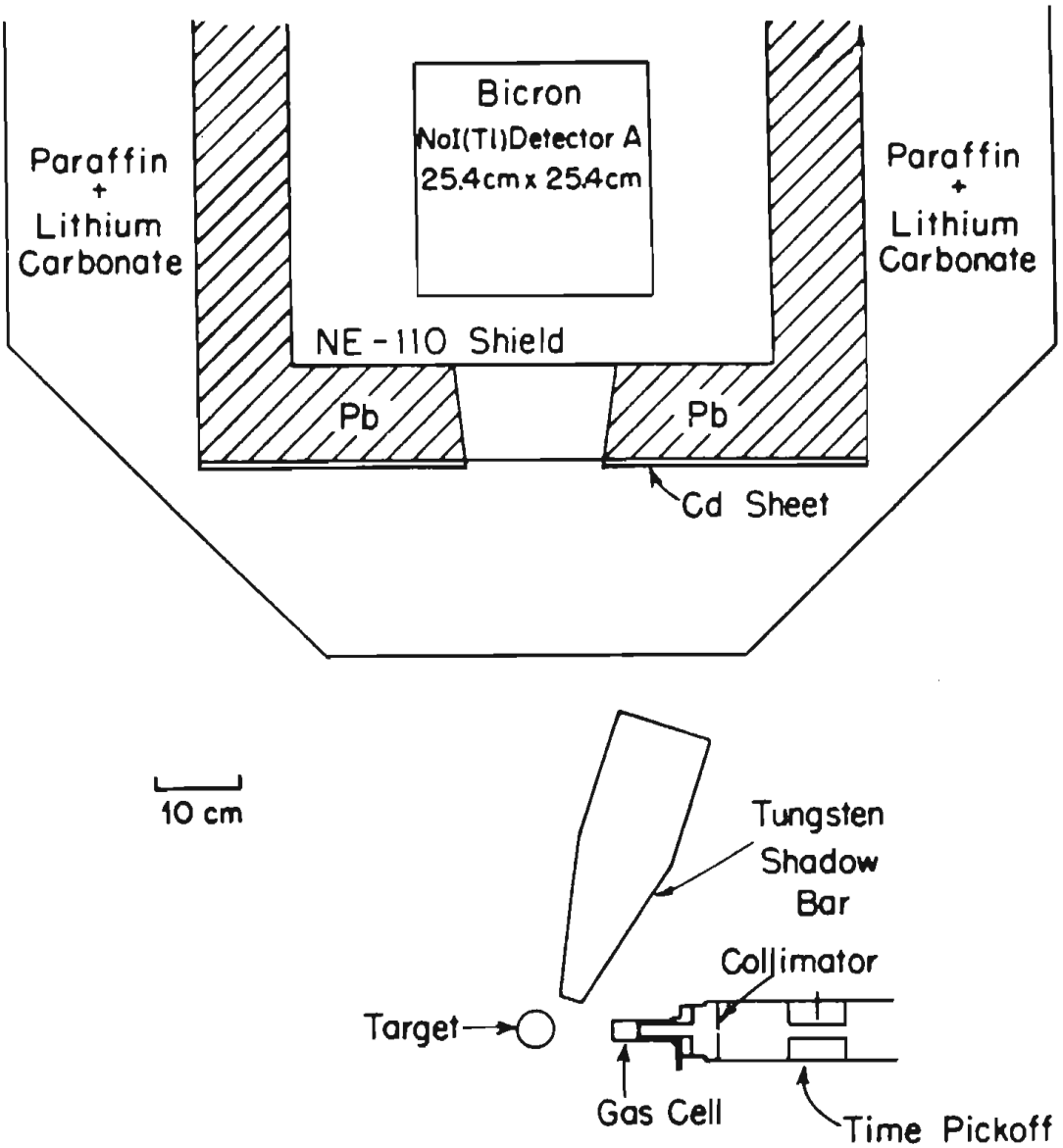

Figure 2-1 TUNL experimental environment used in neutron capture studies.

This investigation of neutron capture on ^{13}C required the use of both unpolarized and polarized beams. The unpolarized deuteron beam was produced by a direct extraction negative ion source and passed through the standard HVEC RF chopper which swept the deuteron beam across a 3/8 inch hole. The deuteron beam pulse was then bunched in a two-gap klystron buncher. The resulting pulsed beam had a frequency of 2 MHz with a full width at half maximum of 2 ns. Deuterium beam currents for unpolarized measurements were typically 350 nA.

Polarized deuteron beams were provided by the TUNL Lamb-shift polarized ion source [Cleg70]. A new ramping and bunching system designed and installed by S.A. Wender [Wend80] was used to pulse the polarized deuteron beam. The resulting pulsed beam had a frequency of 4 MHz and a full width at half maximum of 2 ns. Pulsed polarized beam currents range from 80 to 140 nA. Previously at TUNL, pulsed polarized beam currents of only a few nanoamperes were available [Wend81] and were not satisfactory for neutron capture experiments. A typical polarization of the deuteron beam was 0.70(5). The beam polarization was measured after each capture measurement before the spin was flipped or the detector angle was changed - about every two hours - using the quench ratio method [Trai74]. The polarized ion source was monitored regularly during its operation for quenchable unpolarized beam.

Figure 2-2 is a diagram of the beam line near the deuterium gas cell. The deuteron beam was transported through a capacitive pick-off unit consisting of a 3/8 inch diameter, 3 inch long piece of copper tubing. This provided a timing pulse for time-of-flight

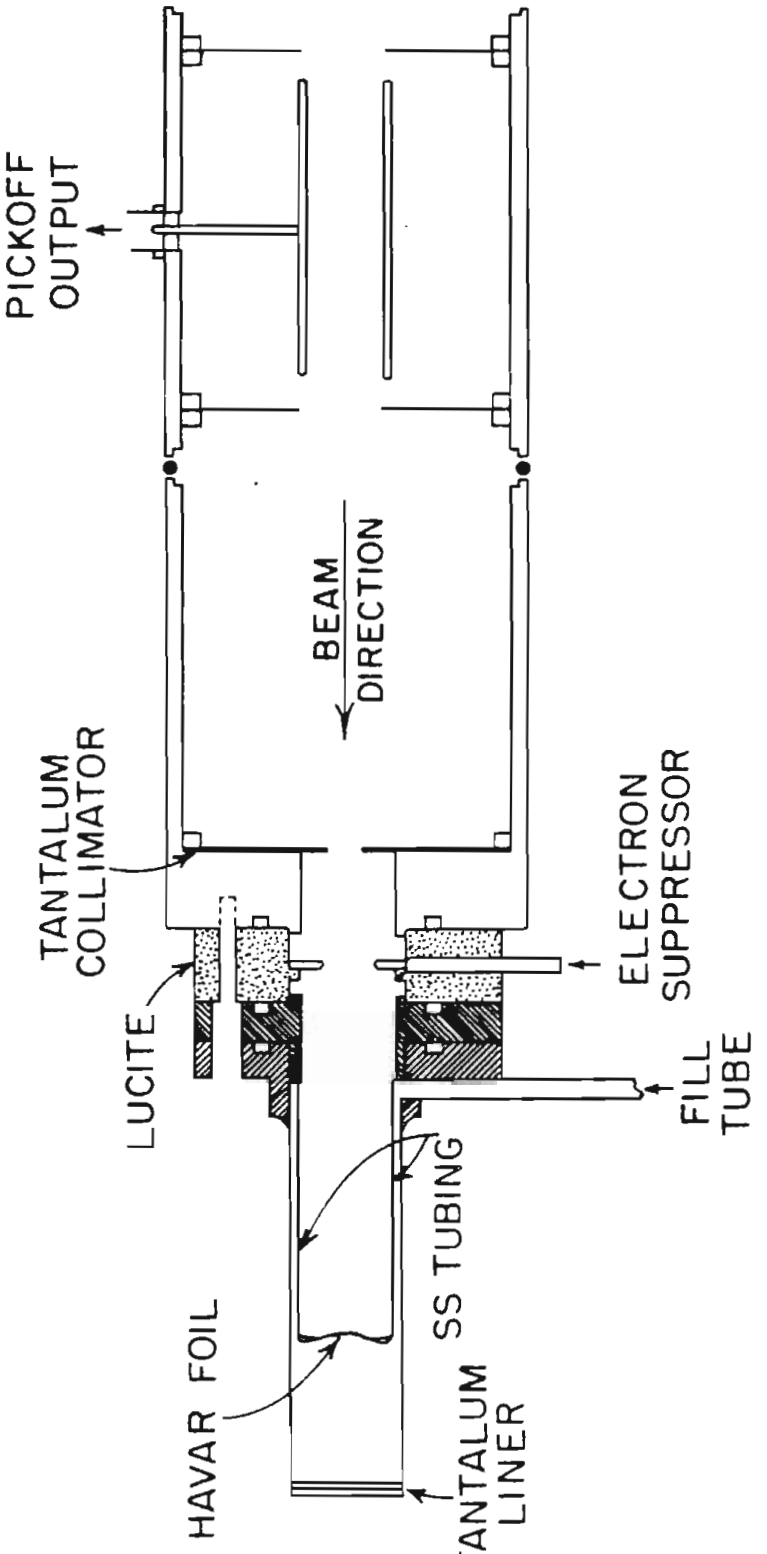

Figure 2-2 The neutron production facility used in neutron capture studies.

discrimination. The beam then passed through a tantalum collimator and electron suppressor ring to the entrance window of the gas cell. For low pressure measurements ($\leq$ 15 psig) the window consisted of 4 $mg \cdot cm^{-2}$ thick Mo foil and for high pressure measurements the window consisted of 5.7 $mg \cdot cm^{-2}$ thick Havar foil. The gas cell is lined with tantalum to reduce the neutrons produced by the (d,n) reaction with the cell walls. The beam passed through the deuterium gas and was stopped in a tantalum beam stop at the end of the gas cell. The charge deposited in the beam stop was integrated to monitor the number of deuterons passing into the gas cell.

As the deuteron beam passed through the gas cell it slowed down so that the neutrons produced at the entrance window and at the tantalum beam stop of the gas cell had different energies. Hogue and Kadi [Hogu79] have written a code, Kadel, to calculate this energy difference and the incident deuteron beam energy necessary to produce the desired 0^{o} neutron energy at the center of the gas cell. Kadel integrates the stopping power of deuterium as the beam passed through the entrance window and then through the gas. Using fixed point iteration the incident deuteron beam energy is modified until the desired 0^{o} neutron energy is produced at the center of the gas cell.

The $^{2}H(d,n)^{3}He$ cross section is forward peaked, sending most of the neutrons into a cone with an angle of $< 20^{o}$. Figure 2-3 shows the $^{2}H(d,n)^{3}He$ cross section as a function of angle at an incident energy of E_{d} = 7 MeV with a resulting 0^{o} neutron energy of E_{n} = 10 MeV. The cross sections were taken from M. Drosg [Dros78].

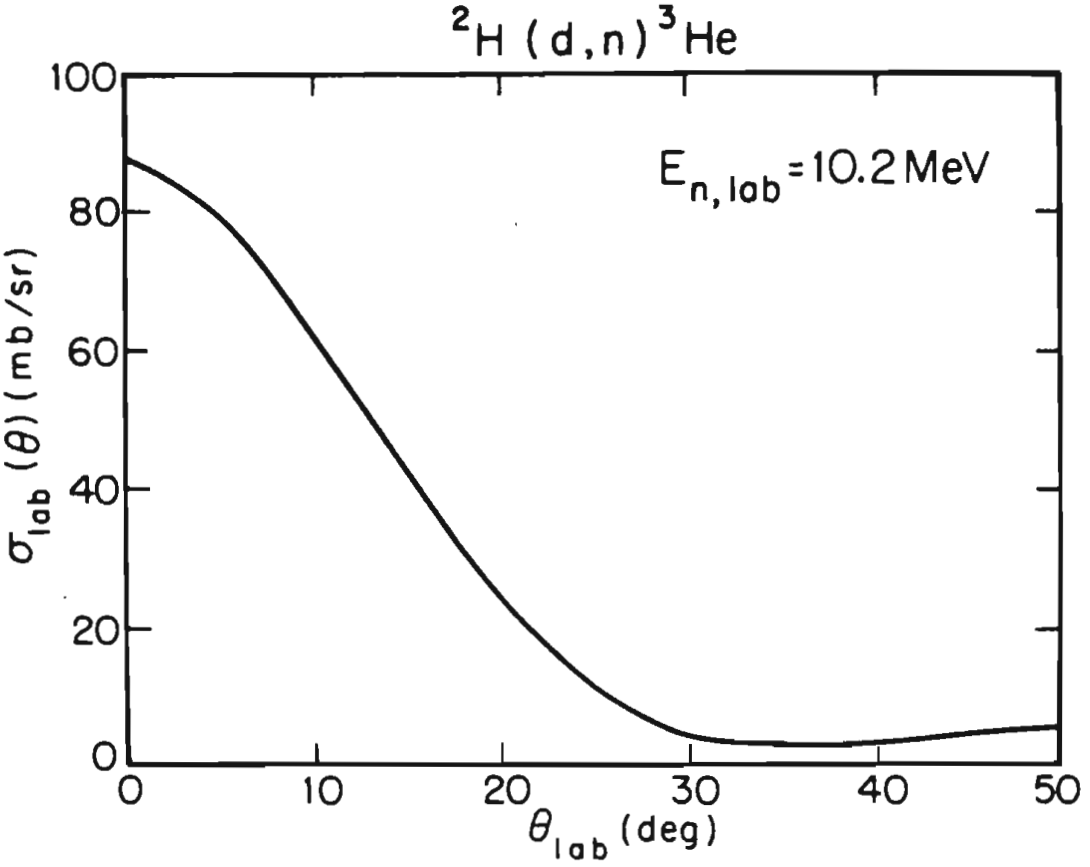

Figure 2-3 The $^2H(d,n)^3He$ cross section from 0° to 50°. The deuteron beam energy is 9.0 MeV, yielding a 0° neutron energy of 10.2 MeV.

Lisowski [Liso73, Liso75] investigated the polarization transfer characteristics of the $^{2}H(d,n)^{3}He$ reaction. The polarized ion source produced a deuteron beam which was both vector and tensor polarized. The deuteron beam was aligned to produce the maximum neutron beam polarization. The 0° cross section is greater than that of an unpolarized beam because of this tensor polarization so that

$$2\text{-}1 \qquad \sigma(0^{\circ}) = \sigma_{u}(0^{\circ}) \left[1 - 1/4\, A_{zz}(0^{\circ})\, P_{zz} \right]$$

where A_{zz} is the tensor analyzing power of the $^{2}H(d,n)^{3}He$ reaction and P_{zz} is the tensor polarization of the deuteron beam. The neutron polarization is also affected by the tensor nature of the polarized deuteron beam.

$$2\text{-}2 \qquad P_{ny} = \frac{3/2\, K_{y}^{y}(0^{\circ})\, P_{z}}{1 - 1/4\, A_{zz}(0^{\circ})\, P_{zz}}$$

where K_{y}^{y} is the polarization transfer coefficient of the $^{2}H(d,n)^{3}He$ reaction and P_{z} is the vector polarization of the deuteron beam. Throughout this work the polarized ion source was operated such that the tensor and vector beam polarizations were equal, i.e., $P_{z} = P_{zz} = P_{d}$. Lisowski measured both $A_{zz}(0^{\circ})$ and $K_{y}^{y}(0^{\circ})$ to be constant over the energy region $3.5 \leq E_{d} \leq 15$ MeV. $A_{zz}(0^{\circ})$ and $K_{y}^{y}(0^{\circ})$ were found to be -0.462 and 0.636. Substituting into Equations 2-1 and 2-2 the values for A_{zz} and K_{y}^{y} one is left with simple numeric expressions found in Equations 2-3 and 2-4.

2-3 $$\sigma(0^{\circ}) = \sigma_u(0^{\circ}) \left[1 + 0.12\, P_d \right]$$

2-4 $$P_{ny} = \frac{0.95}{0.12 + P_d^{-1}} = P_n$$

For example, a deuteron beam with a polarization of 0.68 would produce a yield 8 % greater than that produced by an unpolarized beam. The resulting 0° neutron polarization would be 0.60.

2-c Sample. The target sample consisted of 32.4 g of 96.4 % isotopically enriched ^{13}C powder. The powder could not easily be made into a self-supporting sample so it was pressed into a thin-walled Lucite can. The powder was introduced into the can in one to two gram quantities and then pressed in an effort to maintain a uniform density throughout the sample. The inside dimensions of the Lucite can were 1 1/2 inches in diameter and 1 1/2 inches in height. An identical Lucite can was constructed to be used for sample-out measurements. Initial sample-out measurements showed that the Lucite can had no effect on the capture γ-ray spectra from the $^{13}C(n,\gamma_0)^{14}C$ reaction. Therefore, in general sample-out measurements were not made.

2-d Detectors. The neutron flux from the gas cell was monitored by an NE213 time-of-flight detector placed at 0° to the beam and at 2.6 m from the gas cell. Pulse shape discrimination was used to separate neutron and γ-ray events occurring in the detector.

Another NE213 time-of-flight detector was set level to the beam, at an angle of ~ 45°, and at a distance of ~ 3 m from the gas cell. This side detector was used to monitor the deuteron beam polarization. The side detector was also used as a timing monitor to adjust the bunching systems to produce a 2 ns pulse. To adjust this timing, the pulse shape discrimination system was set to observe γ rays. The bunching system was then adjusted to produce a narrow and symmetric γ-ray time-of-flight peak.

The capture γ rays were detected by a 254 by 254 mm Bicron NaI crystal. The crystal was viewed by six RCA 8575 photomultiplier tubes arranged in a ring behind the crystal. The crystal was encased in a cylindrical-well anticoincidence shield [Suff68] made of NE110 plastic. The shield is viewed by eight XP1031 photomultiplier tubes.

The crystal and anticoincidence shield were encased on five sides with 100 mm of lead and were encased on all six sides with 200 mm of paraffin and lithium carbonate blocks. The front of the assembly also contained a 3 mm sheet of cadmium between the paraffin and lead. A tapered lead collimator – designed to illuminate the entire back face of the crystal at a radial distance of 1.02 m – was used to define the solid angle of the NaI detector. Measurements of the 90° yield curve, and angular distributions of cross section and analyzing power were made with the back of the crystal at a radial distance of 1.02 m. In this position the angular distributions were measured with an angular range of 45°-141° and with an angular acceptance of 14°. The detector was

rolled back until the back of the crystal was at a radial distance of 1.45 m. Angular distributions of cross section were measured with an angular range of 30^{o}-150^{o}. The collimator used for the measurements at 1.02 m was also used for the 1.45 m measurements.

2-e Electronics and Data Acquisition. The two monitor-detector photomultipliers produced both a linear signal and a fast timing signal. The fast signal was routed to a constant fraction discriminator to produce a fast logic signal. This signal was used to start a time-to-amplitude converter. The stop signal for the time-to-amplitude converter was produced by the capacitive time pick-off unit. The linear signal from the time-to-amplitude converter is the time-of-flight signal. This start-stop sequence was chosen to minimize the dead time in the time-to-amplitude converter.

Pulse shape discrimination was used to distinguish between neutron and γ-ray events in the neutron monitor. Neutron and γ-ray events in the scintillator produce bursts of light with different decay rates. The linear signal from the photomultiplier was amplified and then analyzed by a timing single-channel analyzer. The lower level of the single-channel analyzer was set to the Compton edge of the 677 keV γ ray from ^{137}Cs. This corresponds to the scintillator response of ~ 2 MeV neutrons. The logic pulse form the single-channel analyzer was timed with the zero crossing of the bipolar linear signal. The pulse is used to start another time-to-amplitude converter. The stop pulse for the time-to-amplitude converter comes from the constant fraction discriminator. Thus, this time-to-amplitude converter produces a linear

signal with an amplitude proportional to the time difference between the leading edge of the pulse from the constant fraction discriminator and the zero crossing of the linear signal from the timing single-channel analyzer. The linear signal from the time-to-amplitude converter was analyzed by a single-channel analyzer with its window set on the γ-ray group for bunching system adjustments or on the neutron group for monitoring the neutron flux. The logic pulse from this single-channel was used to gate the time-of-flight signal. The time-of-flight signal was then passed to an analogue-to-digital converter interfaced to a Honeywell DDP-224 computer. The computer was used to store, display and write the acquired data upon magnetic tape.

The capture γ-ray electronics processed the signals from the crystal, anticoincidence shield, and the time pick-off unit. The data of interest included the time-of-flight spectrum for events in the NaI crystal, energy spectra of events in the crystal, and diagnostic information, e.g., count rates.

The linear signal from the gain-matched photomultiplier tubes of the NaI detector were summed and the signal was clipped to ~ 350 ns. The signal is then passed through a linear gate with a gate width of 400 ns to reduce pile-up. The signal was then amplified and sent to an analogue-to-digital converter for processing by the computer. The linear signal is split before the linear gate and is analyzed by a fast leading edge discriminator. The logic pulse from this discriminator was used to gate off the detection system for 10 μs, reducing pile-up. The

fast logic pulse was used to start a time-to-amplitude converter. The stop pulse came from the time pick-off unit. The linear signal from the time-to-amplitude converter was the time-of-flight signal for the events in the crystal. The time-of-flight signal was passed to an analogue-to-digital converter for processing by the computer.

The output from the shield photomultiplier tubes was amplified and summed. The signal was then analyzed by a fast leading edge discriminator. The fast logic pulse from the discriminator was split. Both signals were sent to coincidence circuits, one to measure coincident events with the crystal, and one to measure random coincident events with the crystal. The coincidence signals, e.g., from an escape event, cosmic ray, or accidental coincidence, were sent to the computer for proper sorting into energy and time-of-flight spectra. The random coincident events were counted in a scalar.

The dead times for the crystal and neutron monitors were measured by accumulating the deuteron beam charge in three scalars. Two of the scalars were gated off when their respective detectors were dead. The third scalar simply accumulated the digital output pulses from the beam integrator.

A sample NaI time-of-flight spectrum is shown in Figure 2-4. The separation of the neutron and γ-ray events was very good and allowed the placing of a window about the γ-ray events. The NaI energy events were sorted into separate spectra according to their time-of-flight. The resulting separation can be seen in Figure 2-5.

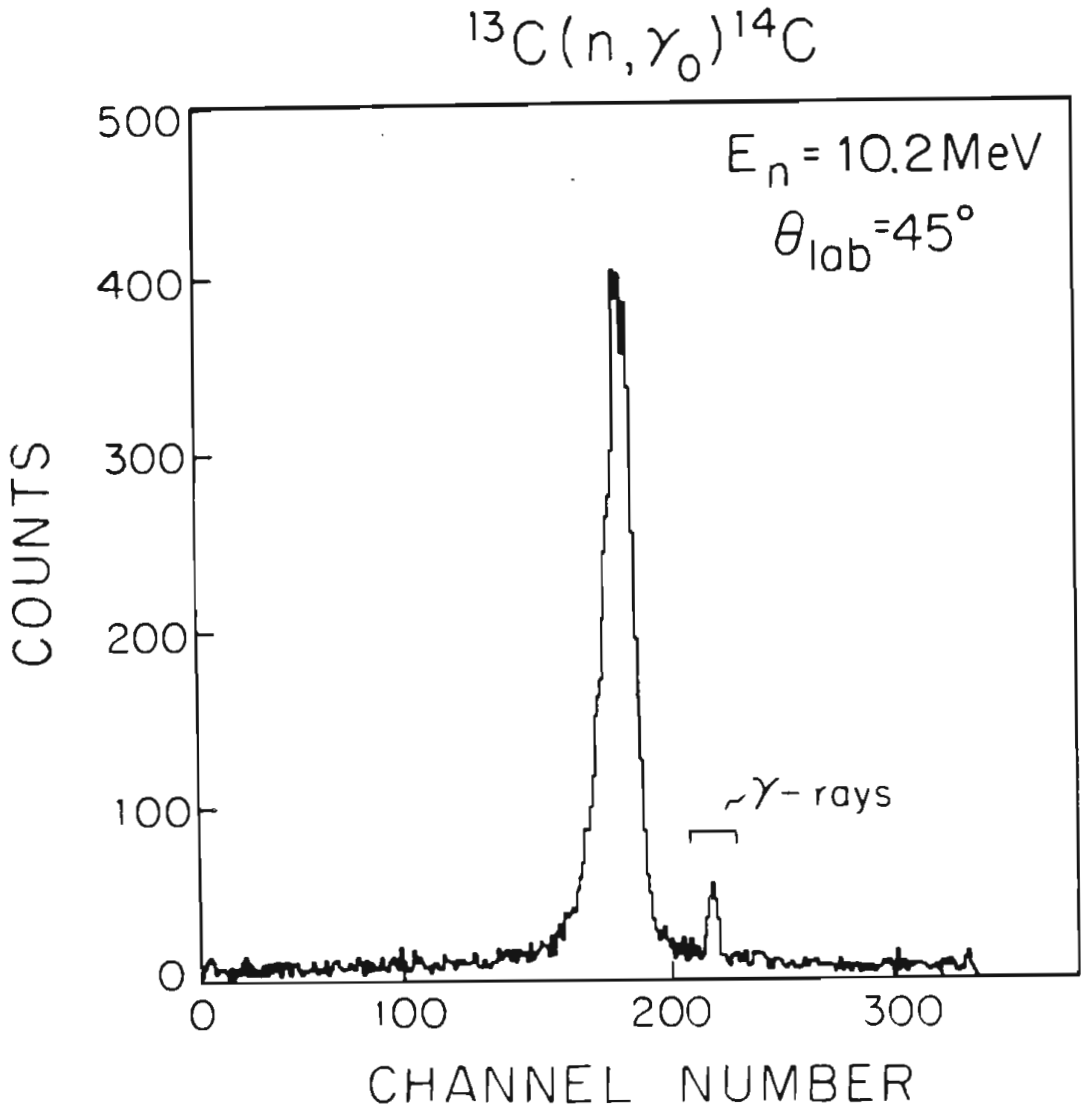

Figure 2-4 Typical time-of-flight spectrum of events in the NaI crystal. This spectrum was accumulated at a neutron energy of 10.2 MeV and with the detector at a lab angle of 45°.

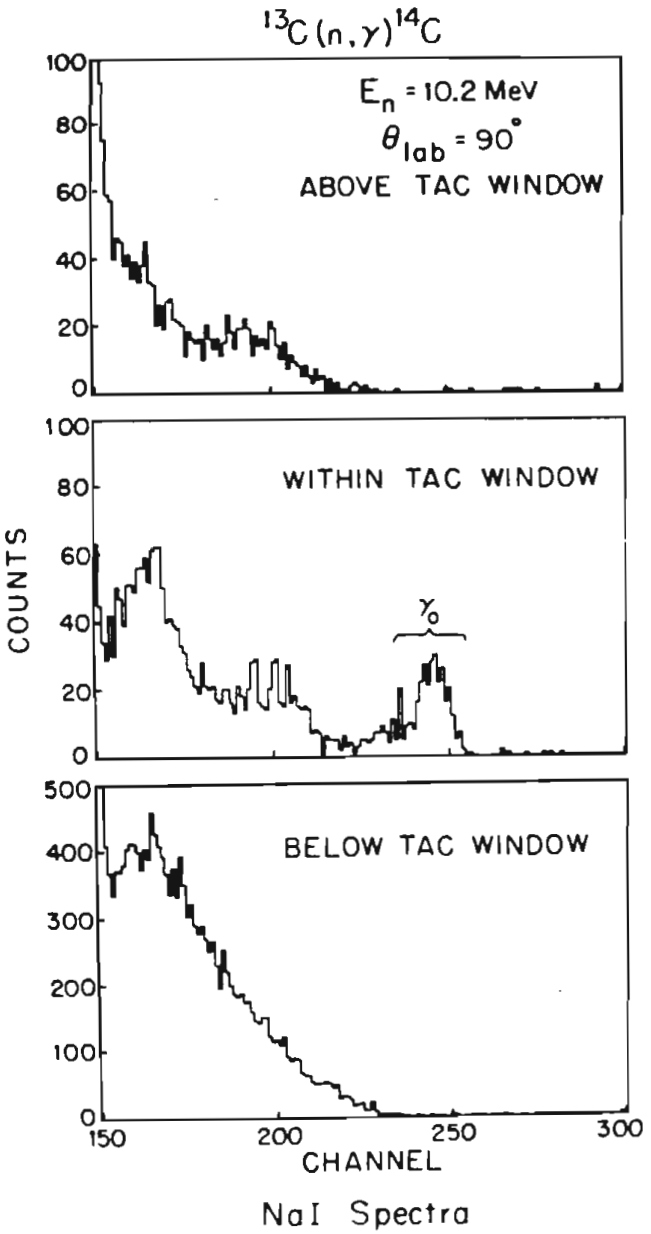

Figure 2-5 The time separated energy spectra from the NaI crystal. Refer to Figure 2-4 for typical γ-ray TAC window setting. The spectra were accumulated at a neutron energy of 10.2 MeV and with the detector at a lab angle of 90°

The NaI detection system was operated in two different modes, high-rejection and low-rejection. These two modes differed in the energy level of the discrimination in the anticoincidence shield circuit. The two modes result in different efficiencies and resolution and required two different functions for fitting the γ-ray spectra. The low-rejection line shape was designed by R.C. McBroom [McBr77]. The high-rejection line shape was designed by J.D. Turner [Turn78]. The line-shape fitting functions used in fitting the γ-ray spectra can be found in Table A-1 and in Figure 2-6. S. King [TUNL80] has redesigned both the high-rejection and low-rejection line-shape fitting functions. His line-shape functions should be used for future peak fitting.

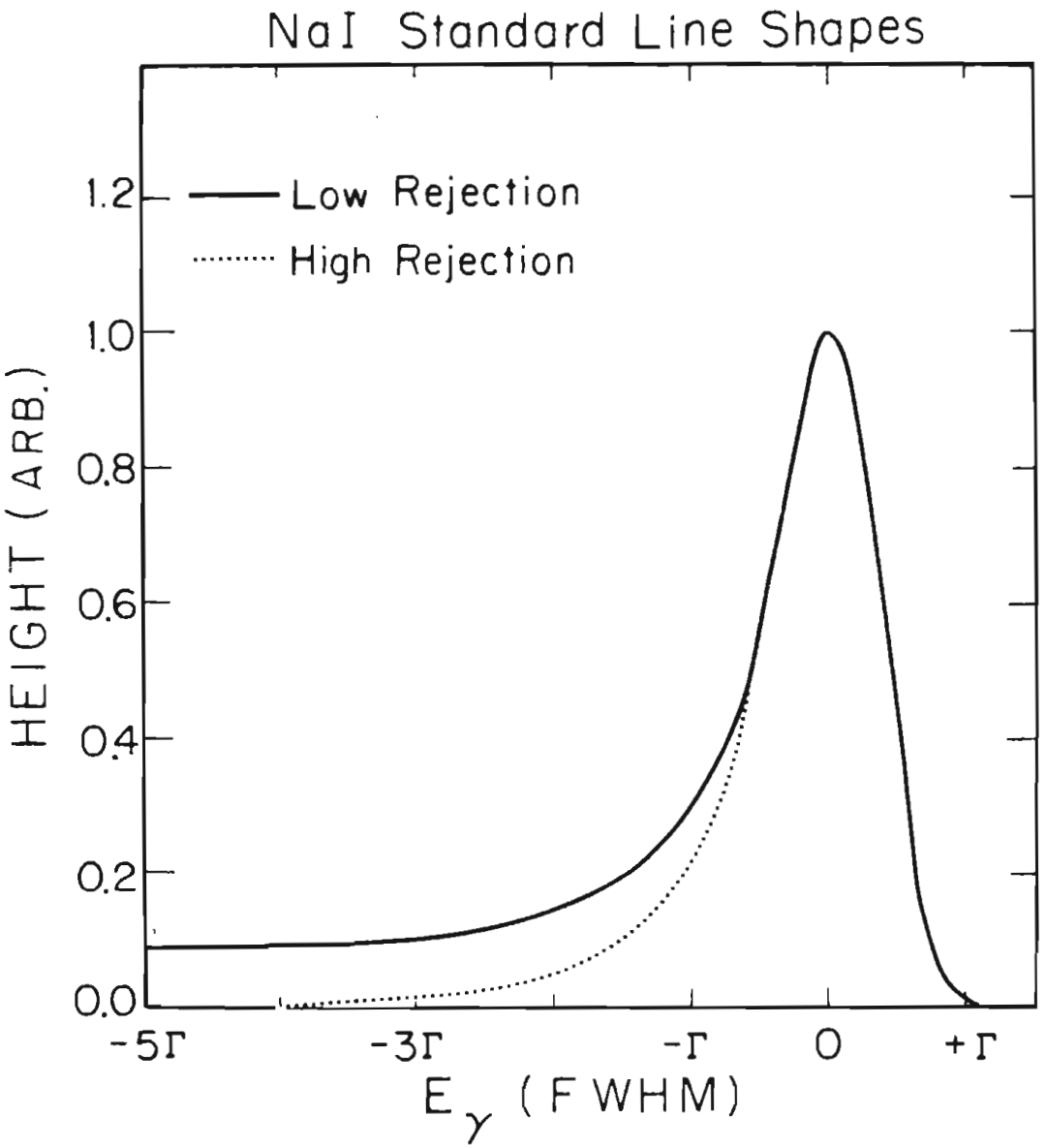

Figure 2-6 The high-rejection and low-rejection line-shape fitting functions used to fit peaks in the NaI energy spectra.

3 EXCITATION FUNCTION

3-a Peak Stripping and Summing. The $^{13}C(n,\gamma_0)^{14}C$ reaction yield was measured at 90^{o} for neutron lab (excitation) energies from 5.6 (13.4) to 14 (21.2) MeV. The analysis of the yield involved fitting each γ-ray spectrum with the appropriate standard line shape [McBr77, Turn78]. The higher energy (7 - 14 MeV) data were taken in low-rejection mode and the lower energy (5.6 - 7 MeV) data was taken in the high-rejection mode. The increased background at the lower energies was compensated by using the mode with better resolution, but with a lower efficiency. The spectra at 7 and 7.4 MeV were taken in both modes to provide a normalization between the low-rejection and high-rejection modes.

The standard line shape is a vector function of three variables; the position of the peak, the width of the peak, and the maximum value of the peak. The Rotofeed fitting code was used to minimize the chi-square between the data and the standard line shape. Unfortunately there was too much variability in the values of the peak width at adjacent energies. This problem was solved by applying a physical constraint to the values of the widths. The widths were constrained by imposing a constant fractional resolution, i.e., $\Gamma = c\ E_\gamma$. Two separate values of "c" were required, one for the high-rejection line shape and one for the low-rejection line shape.

The fitting code returned peak position and width in terms of channels. To convert the width into energy, the NaI detection system was calibrated using the neutron beam energy and kinematics. The

detection system suffered a gain shift about half way through the run so two calibrations were maintained for each rejection mode. The value of "c" used was formed by averaging the values of Γ / E_γ for each data point, taken with the same rejection rate and the same gain.

The widths were constrained and the spectra were refit, searching on only peak position and height. The raw sums with their backgrounds, beam charge and accidental coincidence rates are presented in Table B-1. The yield curve with the data corrected for background, beam charge and accidental coincidence rate is shown in Figure 3-1. The uncertainties shown represent one standard deviation of the statistical error.

The gas cell was pressurized to ~ 1 atm. (gauge) of deuterium gas and used a 4 $mg \cdot cm^{-2}$ thick Mo foil window. The code Kadel (§2-b) was used to calculate the energy spread of the resulting neutron beam, which is plotted in Figure 3-2.

3-b Cross Section. The number of observed γ rays at 90° may be written as

$$3\text{-}1 \qquad N = 1.13\ 10^{18}\ \sigma_{n,\gamma}(90^\circ)\ \sigma_{d,n}(0^\circ)\ Q_b\ \frac{M_s}{A_s}\ t\ r_{gs}^{-2}\ \varepsilon_d\ \Omega_d\ R(90^\circ)$$

where N is the total number of counts observed for an accumulated beam charge Q. The remaining symbols used are described in Table 3-1.

The factors ε_d, $R(90^\circ)$ and $\sigma_{d,n}$ are functions of energy. The NaI efficiency was previously measured for 15 MeV γ rays from the $^{12}C(p,p'\gamma)$ reaction with the same rejection rate and the same gain [Robe78]. The

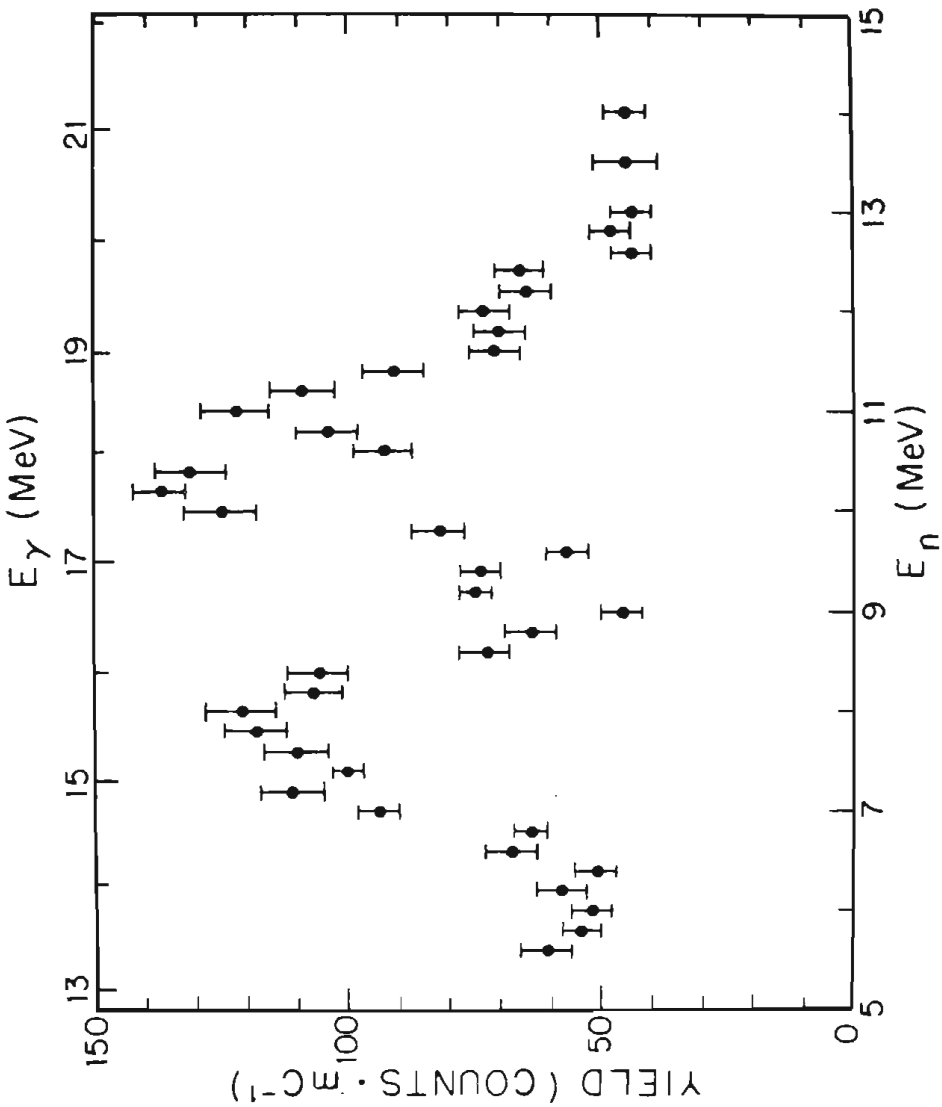

Figure 3-1 The yield curve for the $^{13}C(n,\gamma_0)^{14}C$ reaction. The data points have been corrected for beam charge, background, gas cell pressure and accidental coincidences.

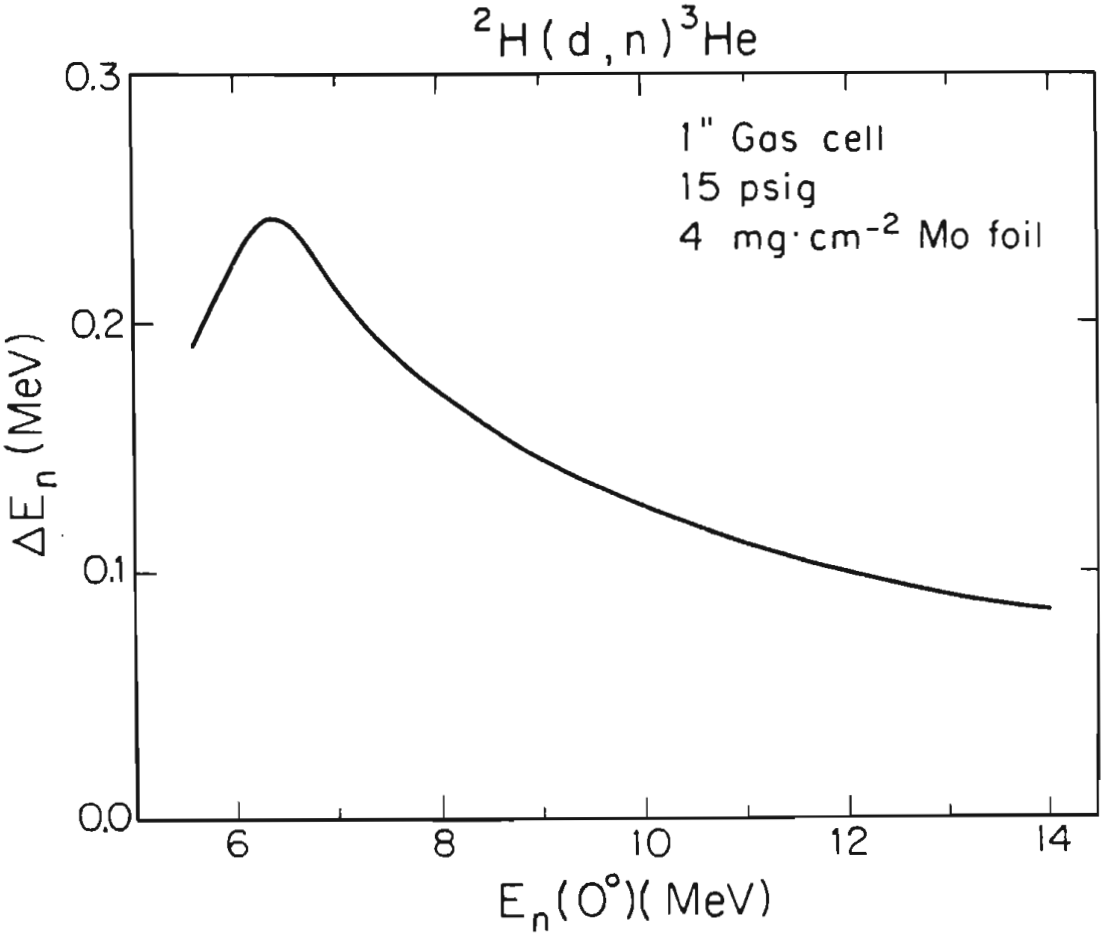

Figure 3-2 Neutron beam energy spread from the gas cell used for measuring the yield curve. E_n is the neutron energy for 0° neutrons produced at the center of the gas cell. ΔE_n is the difference in energy between the 0° neutrons produced at the front and back of the gas cell. This function was calculated by the code Kadel.

Table 3-1 Description of the symbols with units used in Equation 3-1.

Symbol	Description
A_s	- Atomic mass of target nuclei (^{13}C) in the sample
N	- Number of observed capture γ rays (counts)
ε_d	- NaI detector efficiency
M_s	- Mass of target (^{13}C) in sample (31.1 g)
Ω_d	- NaI detector solid angle (45.1 msr)
Q_b	- Total charge of deuterium beam that passed through the gas cell (C)
R(90°)	- 90° correction ratio for finite-geometry
r_{gs}	- Distance from the center of the gas cell to the center of the sample (8 cm)
$\sigma_{d,n(0^o)}$	- 0° cross section for the $^2H(d,n)^3He$ reaction ($mb \cdot sr^{-1}$)
$\sigma_{n,\gamma(90^o)}$	- 90° cross section for the $^{13}C(n,\gamma_0)^{14}C$ reaction ($\mu b \cdot sr^{-1}$)
t	- Thickness of deuterium in the gas cell ($g \cdot cm^{-2}$)

efficiency was factored into two parts, $\varepsilon_d(E_\gamma) = \varepsilon_d(15\ \text{MeV})\ f(E_\gamma)$, where $f(E_\gamma)$ contains the energy dependent factors in the detection system efficiency. These factors include the NaI detector response function, the front shielding attenuation, and the anticoincidence shield rejection rate [Well80]. $f(E_\gamma)$ was normalized to one at 15 MeV. The values of $1 - f(E_\gamma)$ were fit to a quadratic polynomial to provide efficiency values at non-integer energies, see Figure 3-3.

The 90° finite-geometry correction ratio, $R(90^\circ)$, is discussed in §5-c and shown in Figure 3-4. The data points were well fit by a straight line. This straight line was used as the correction ratio in Equation 3-1.

The 0° cross section for the $^2H(d,n)^3He$ reaction [Dros78] was interpolated as a function of energy using cubic splines [deBo78]. The data points and the cubic spline function are plotted in Figure 3-5. Note that this factor varies by fifty percent over the domain of the excitation function.

The resulting 90° cross section can be found in Table B-2 and Figure 3-6. The excitation function shows the typical structure found in the Giant Resonance Region of light nuclei [Ful162].

The total cross section for neutron capture is dependent upon the angular distribution of the cross section. The angular distributions of cross section were only measured at five energies, §4-b. The Legendre expansions of the measured angular distributions were integrated over θ to yield A_0, where $\sigma_{n,\gamma} = 4\ \pi\ A_0$. To provide the $\sigma(90^\circ)/A_0$ ratio over

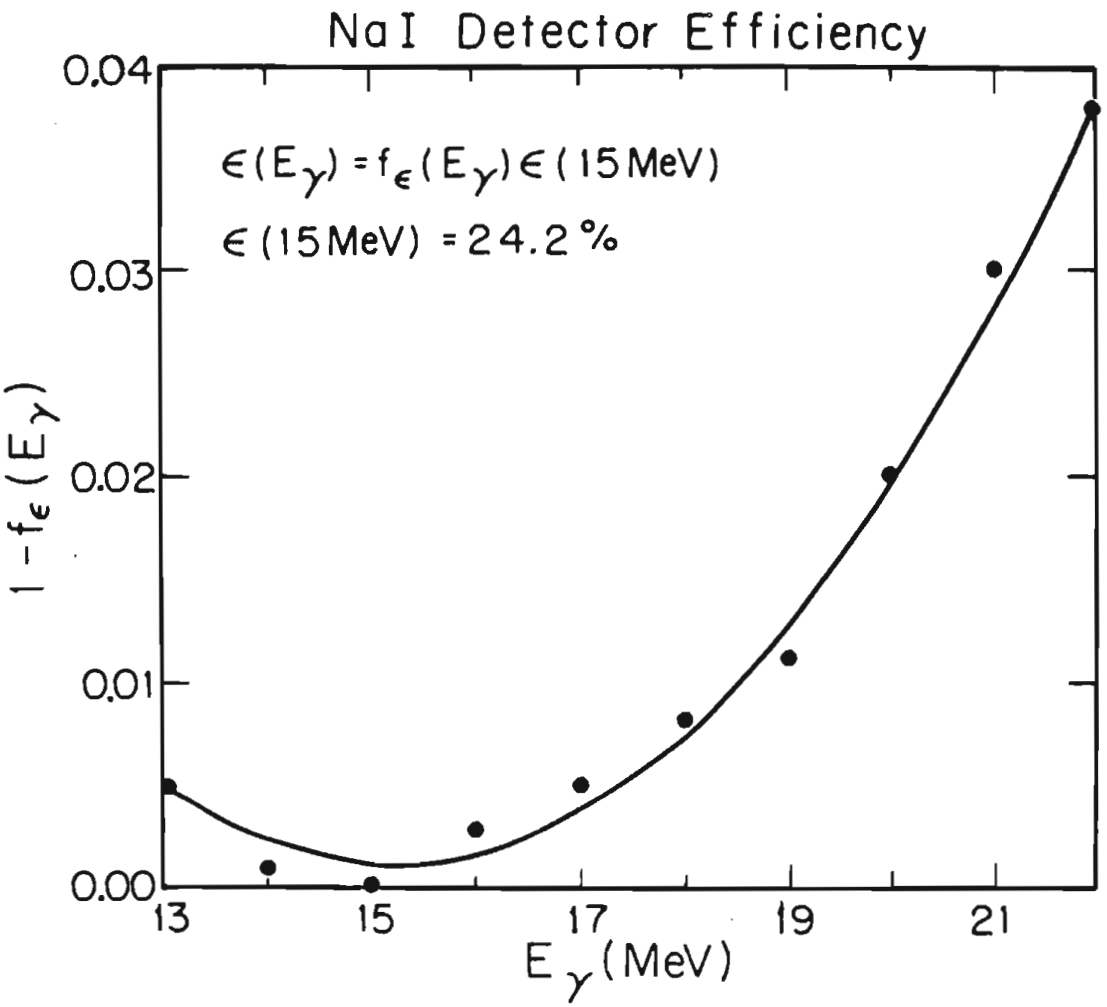

Figure 3-3 The efficiency function for the NaI detection system. The points are ratios of the γ-ray absorption cross sections at E_γ to the 15 MeV cross sections. The solid line is a quadratic fit to $1 - f(E_\gamma)$.

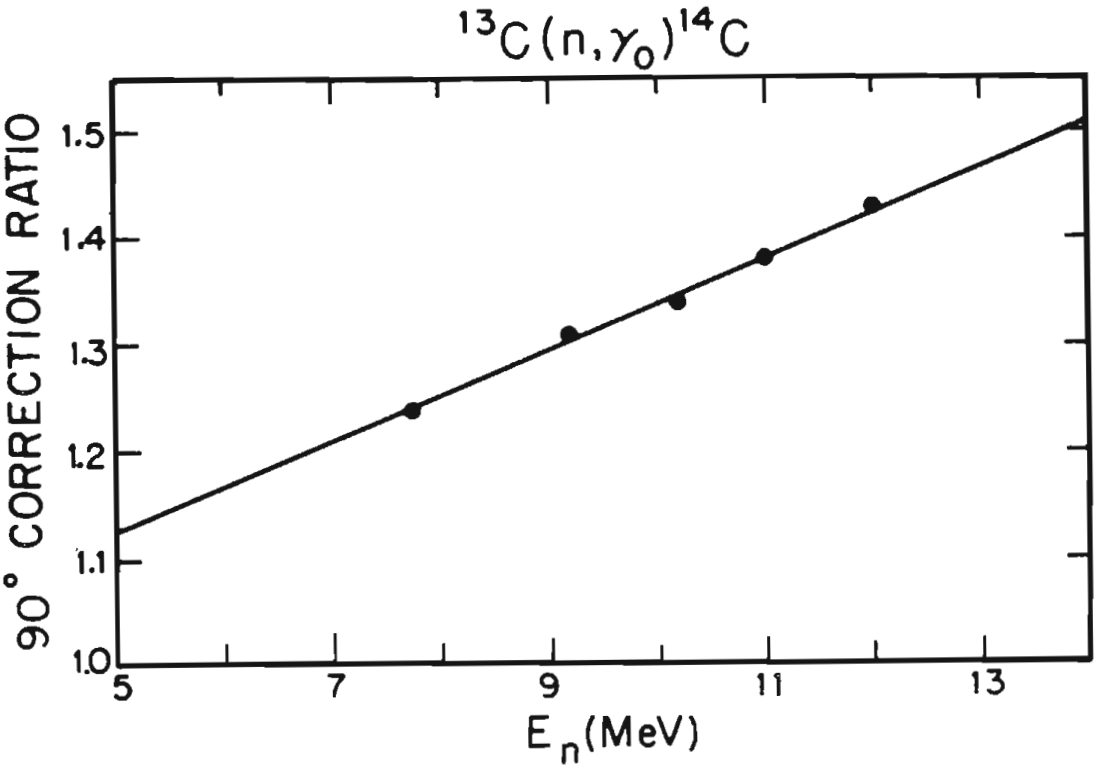

Figure 3-4 The 90° finite-geometry correction ratio. The points were calculated from the measured angular distributions, see §5-c. The solid line is a linear fit to the data.

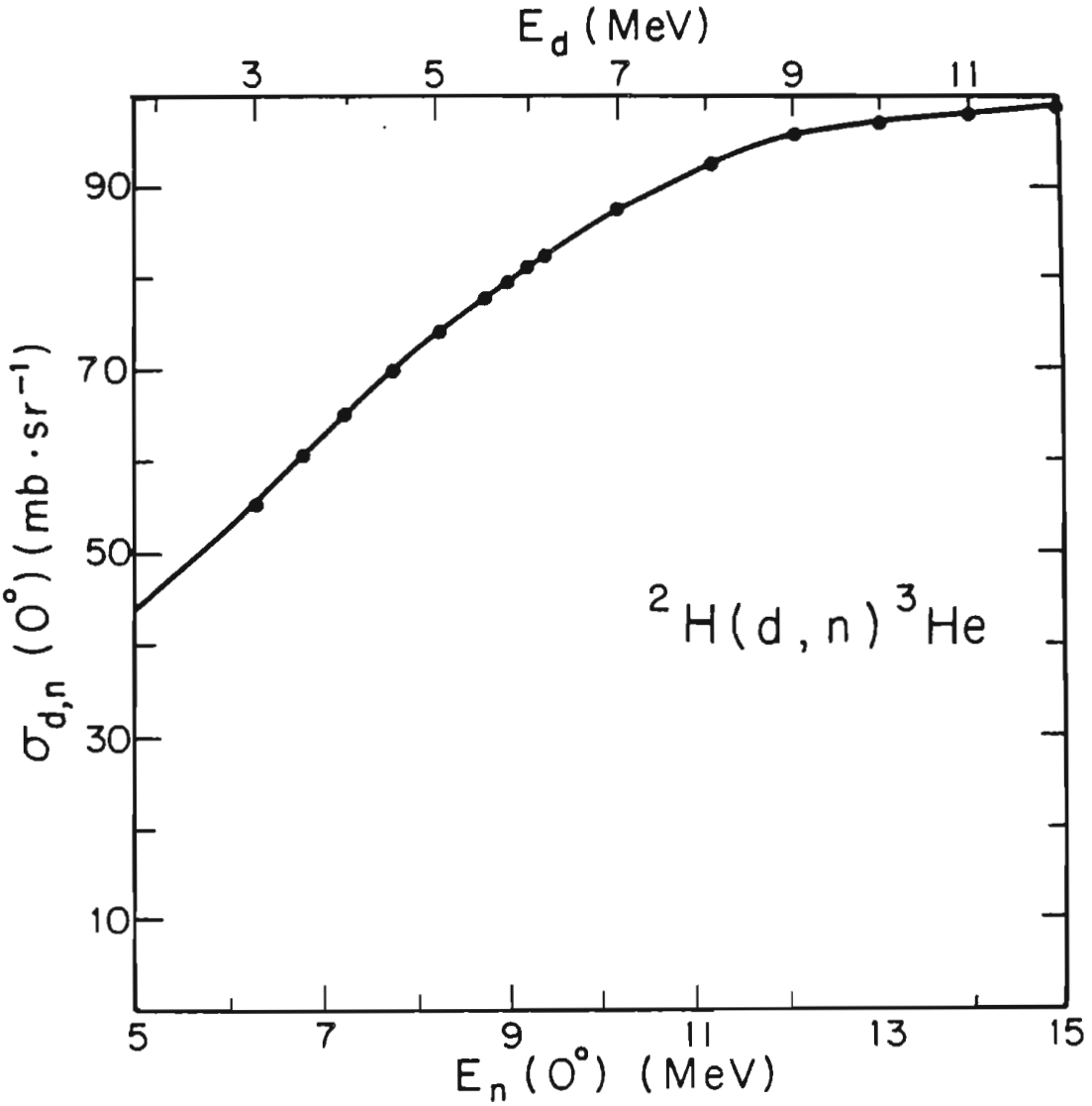

Figure 3-5 The 0° cross section of the $^{2}H(d,n)^{3}He$ reaction as a function of the 0° neutron energy [Dros78].

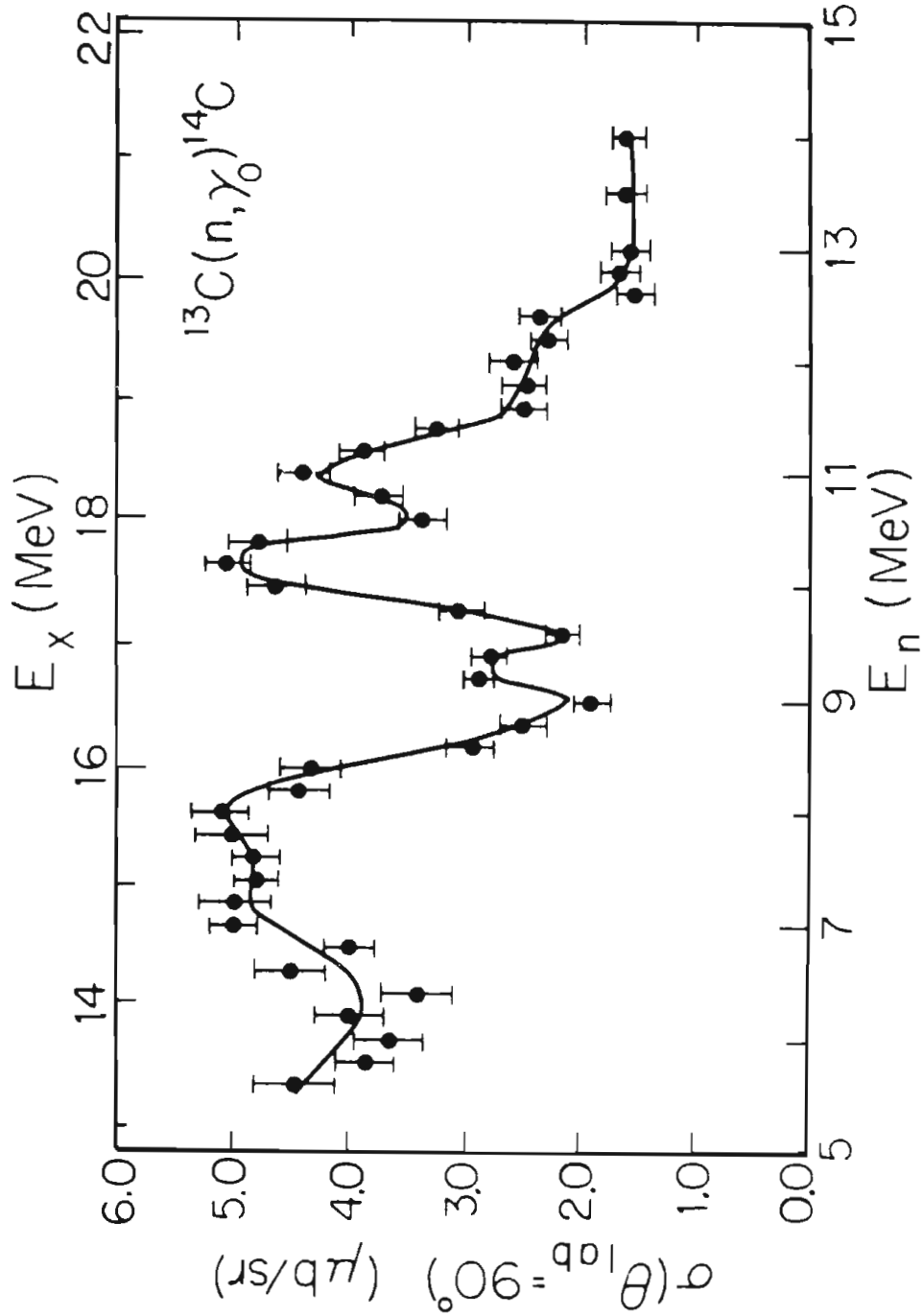

Figure 3-6 The 90° cross section of the $^{13}C(n,\gamma_0)^{14}C$ reaction.

the excitation function's domain, a direct-semidirect calculation of $\sigma(90^{o})/A_{0}$ was normalized to the data as seen in Figure 3-7. This normalized function was used to convert the 90^{o} cross section into the total cross section found in Table B-3 and in Figure 3-8.

Radiative capture and photonuclear emission are time-reversed inverses; hence, the cross sections are related in the center of mass to the spins of the nuclei and the neutron and γ ray momenta. The detail balance relation between radiative capture and photonuclear emission is derived in [Hayw70]:

$$\sigma_{\gamma,n_0} = 2 \frac{2J_A + 1}{2J_{A+1} + 1} \frac{A}{A+1} \frac{E_x - Q}{E_\gamma^2} Mc^2 \sigma_{n,\gamma_0} \qquad 3\text{-}2$$

where J_A and J_{A+1} are the spins of the neutron target and resultant nuclei, Q is the q-value of the capture reaction, and Mc^2 is the energy equivalent of the rest mass of the neutron. For the $^{13}C(n,\gamma_0)^{14}C$ reaction, A = 13, J_A = 1/2, J_{A+1} = 0, Q = 8.2 MeV and Mc^2 = 939.6 Mev. For example, at $E_n(E_\gamma)$ = 10.2 (17.7) MeV the conversion factor is 106. The $^{14}C(\gamma,n_0)^{13}C$ reaction cross section was obtained via detail balance and is presented in Table B-4 and Figure 3-9. The σ_{γ,n_0} cross section will be used in §7-a in comparing the measured cross section with the photonuclear absorptive strength sum rules.

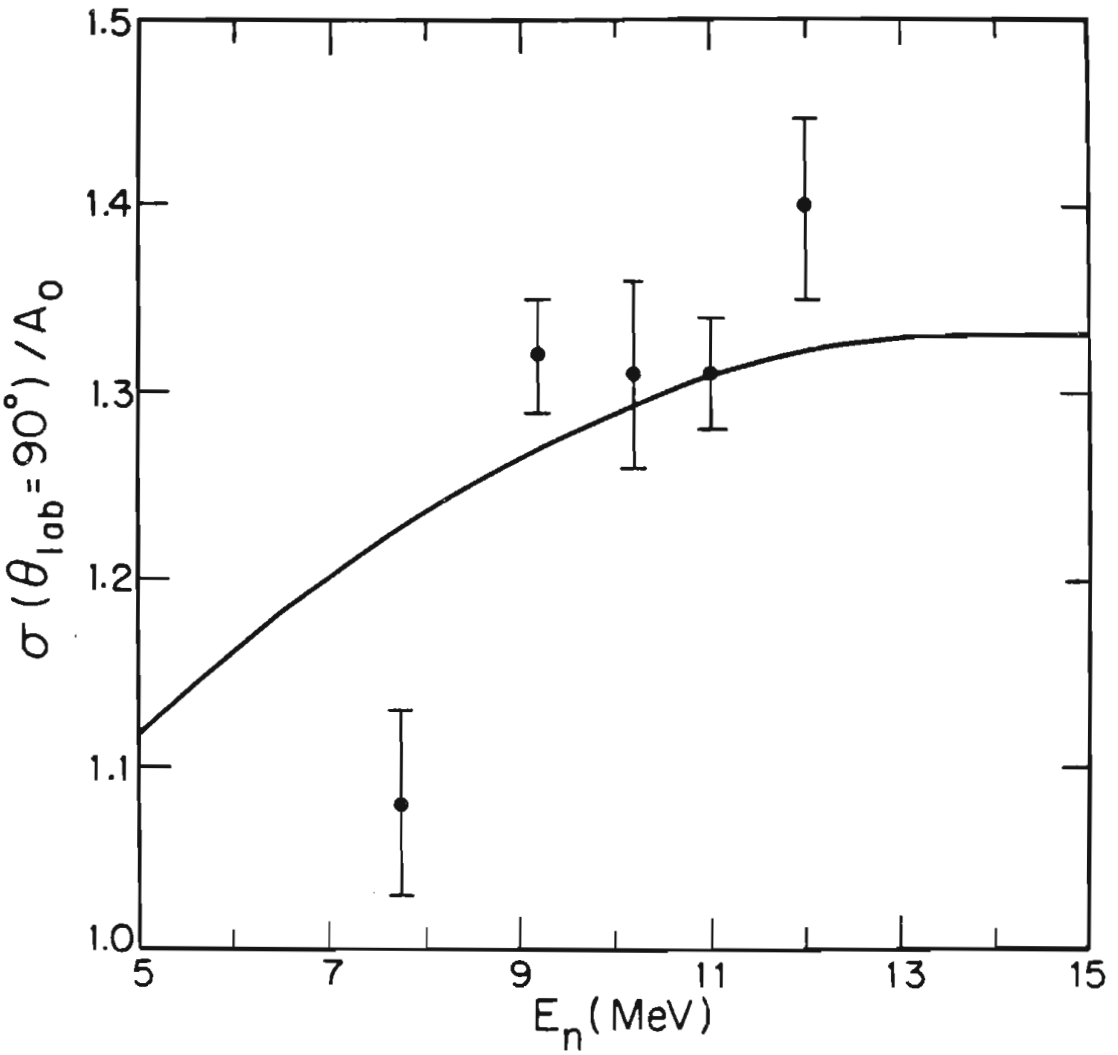

Figure 3-7 The ratio of $\sigma(90°)$ to A_0. The points are the observed data. The solid line is a direct-semidirect calculation normalized to the data.

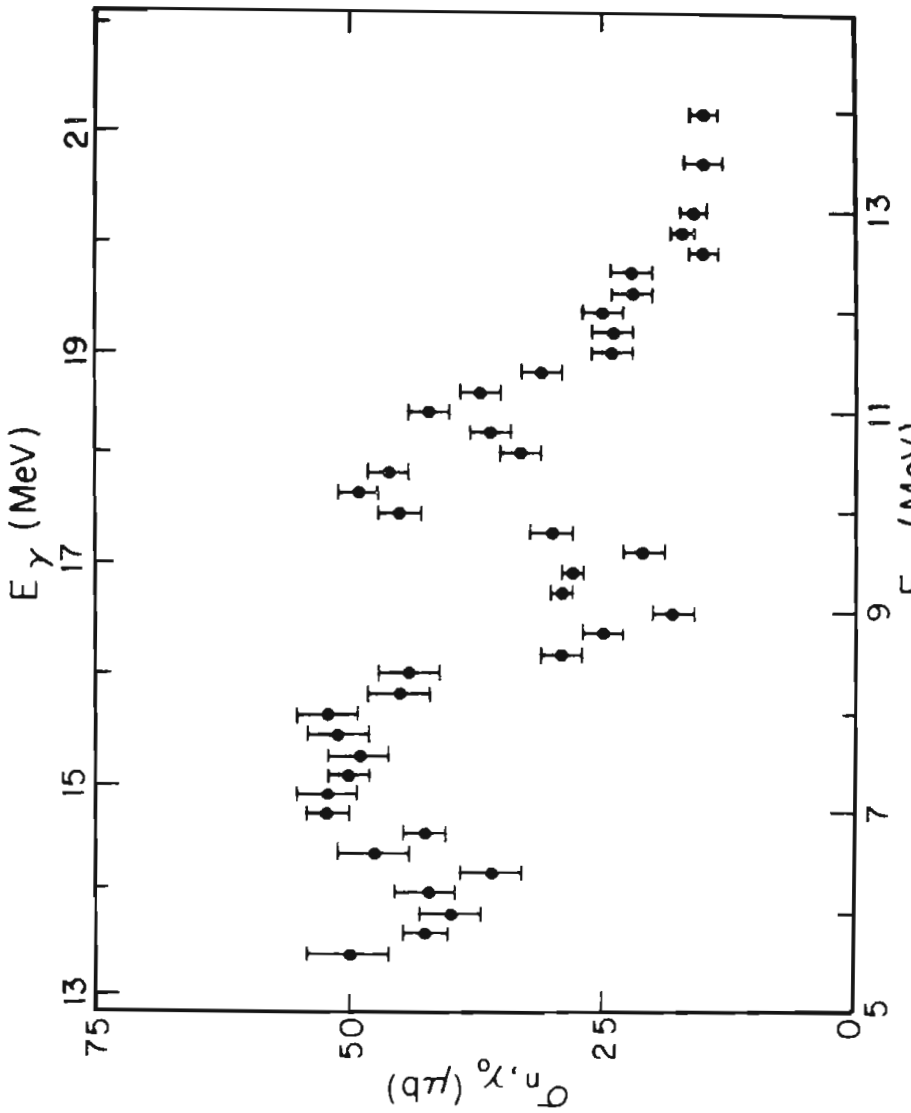

Figure 3-8 The total cross section of the $^{13}C(n,\gamma_0)^{14}C$ reaction.

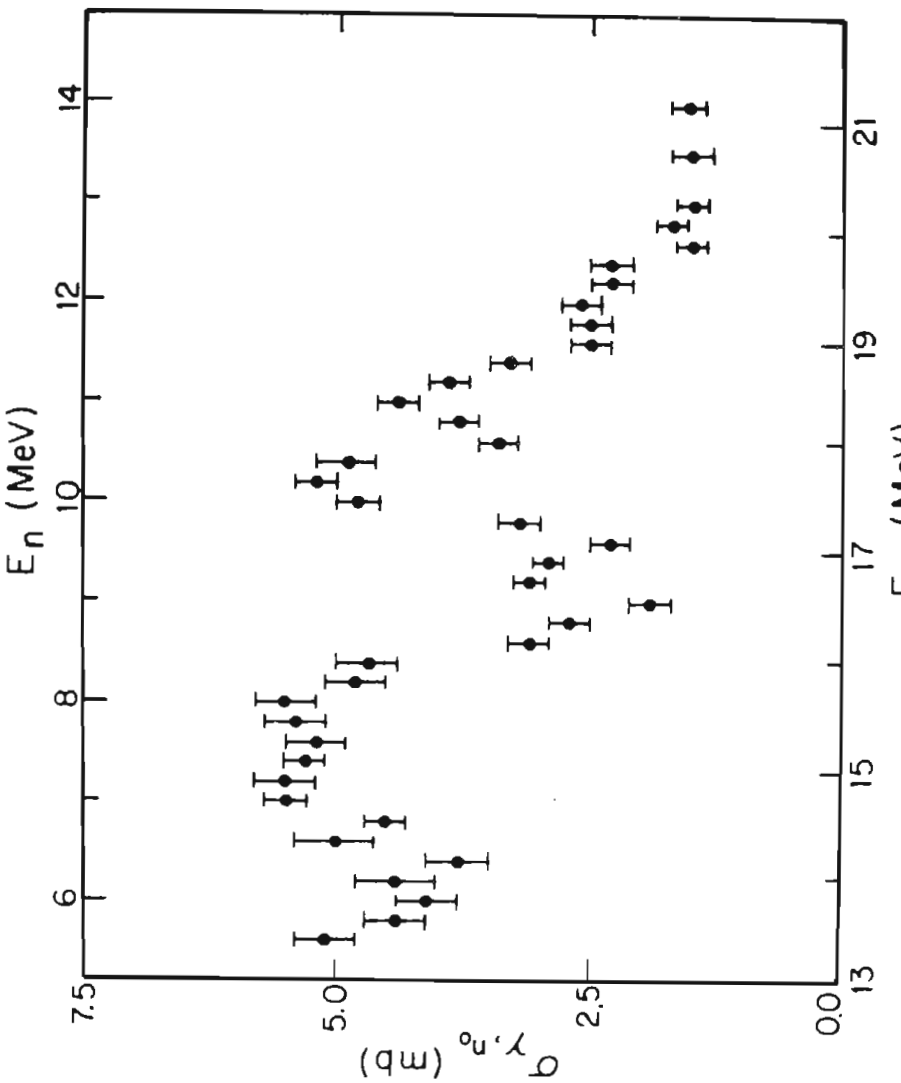

Figure 3-9 The total cross section of the $^{14}C(\gamma,n_0)^{13}C$ reaction obtained through detail balance.

4 ANGULAR DISTRIBUTIONS

4-a Peak Stripping and Summing. Angular distributions of cross section and analyzing power were measured at five energies, E_n = 7.75, 9.2, 10.2, 11 and 12 MeV. The cross section was measured over an angular range of 30^o-35^o to 150^o. The analyzing power was measured over an angular range of 45^o to 140^o. The low-rejection mode was used to increase the efficiency of the NaI detection system, at the expense of detector resolution.

The γ-ray spectra were fit using the low-rejection standard line shape, §2-e. As discussed in §3-a the fitting of the three variables - position, width and height - produces an unreliable area. Here, again, the solution was the application of a physical constraint on the values of the widths. The γ-ray spectra of one angular distribution measurement were fit using all three variables and the resulting widths were averaged. This mean width was held constant and the γ-ray spectra were refit. The yields were obtained by integrating the fitted line-shape function. Several measurements of the angular distributions were made at each energy. They were combined by expanding the cross section in terms of three Legendre polynomials - $P_0(x)$, $P_1(x)$ and $P_2(x)$ - as discussed in §4-b, and then normalizing the separate angular distributions to have the same coefficient for $P_0(x)$, the constant term.

To increase the yield and decrease the resulting counting error, higher pressures were used in the deuterium gas cell when measuring angular distributions than when measuring the excitation function. The pressures and neutron energy spread are listed in Table C-1.

With unpolarized beam, the cross section is proportional to the yield, i.e.,

$$4\text{-}1 \qquad \sigma(\theta) \propto N_u(\theta),$$

and with polarized beam, the cross section is proportional to the sum of the yields from the spin-up and spin-down beams, i.e.,

$$4\text{-}2 \qquad \sigma(\theta) \propto N_+ + N_-.$$

The analyzing power of a reaction is defined as

$$4\text{-}3 \qquad A_y(\theta) = \frac{1}{P_n(\theta)} \frac{N_+ - N_-}{N_+ + N_-},$$

where $P_n(\theta)$ is the neutron beam polarization, §2-b. The data points of cross section, $\sigma(\theta)/A_0$, are listed in Table C-2 and displayed in Figure 4-1. The data points of analyzing power, $A_y(\theta)$, are also listed in Table C-2 and displayed in Figure 4-2. The uncertainties represent one standard deviation of the statistical error.

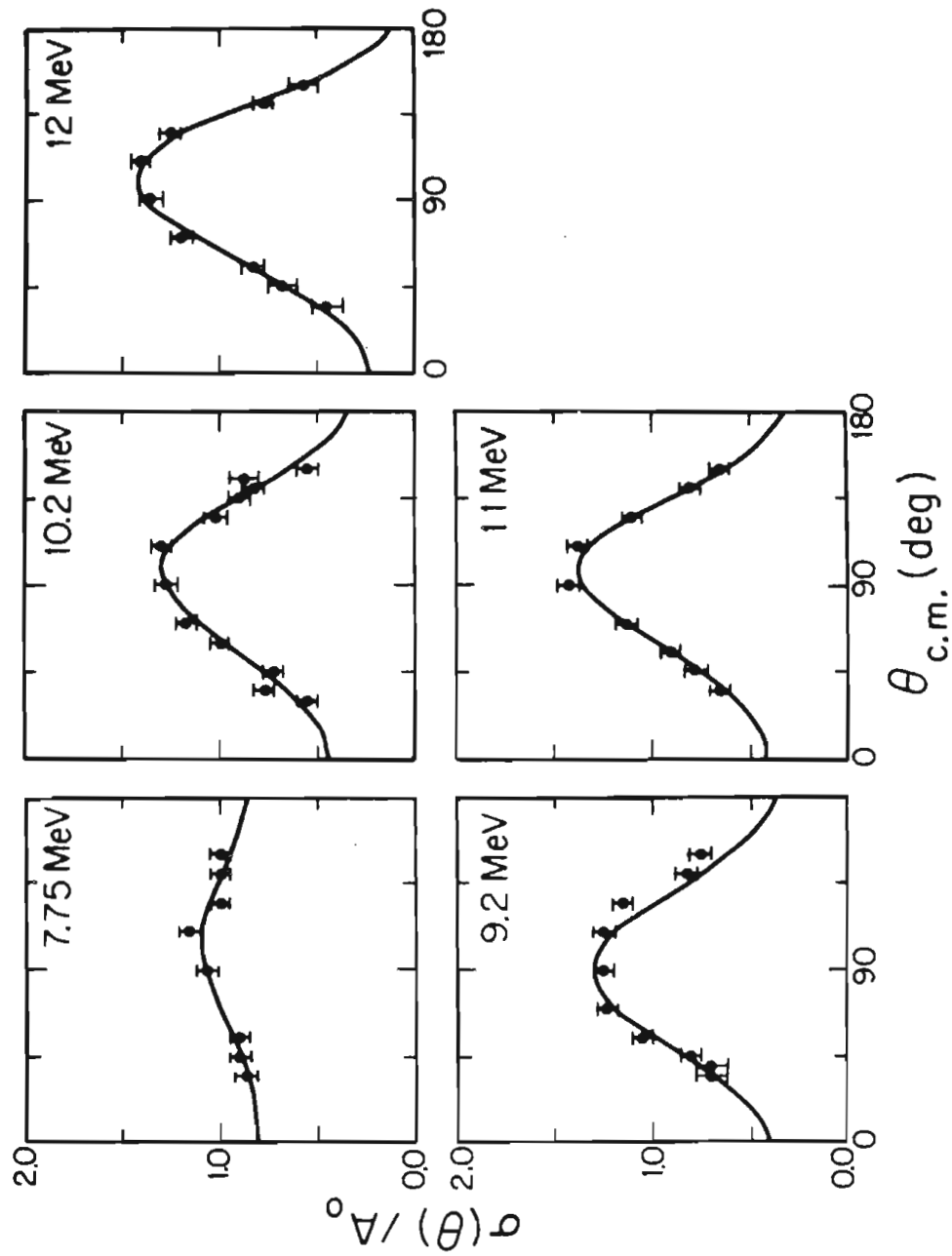

Figure 4-1 Observed angular distributions of cross section for the $^{13}C(n,\gamma_0)^{14}C$ reaction at neutron energies of 7.75, 9.2, 10.2, 11 and 12 MeV. The fits are through $n_{max} = 3$.

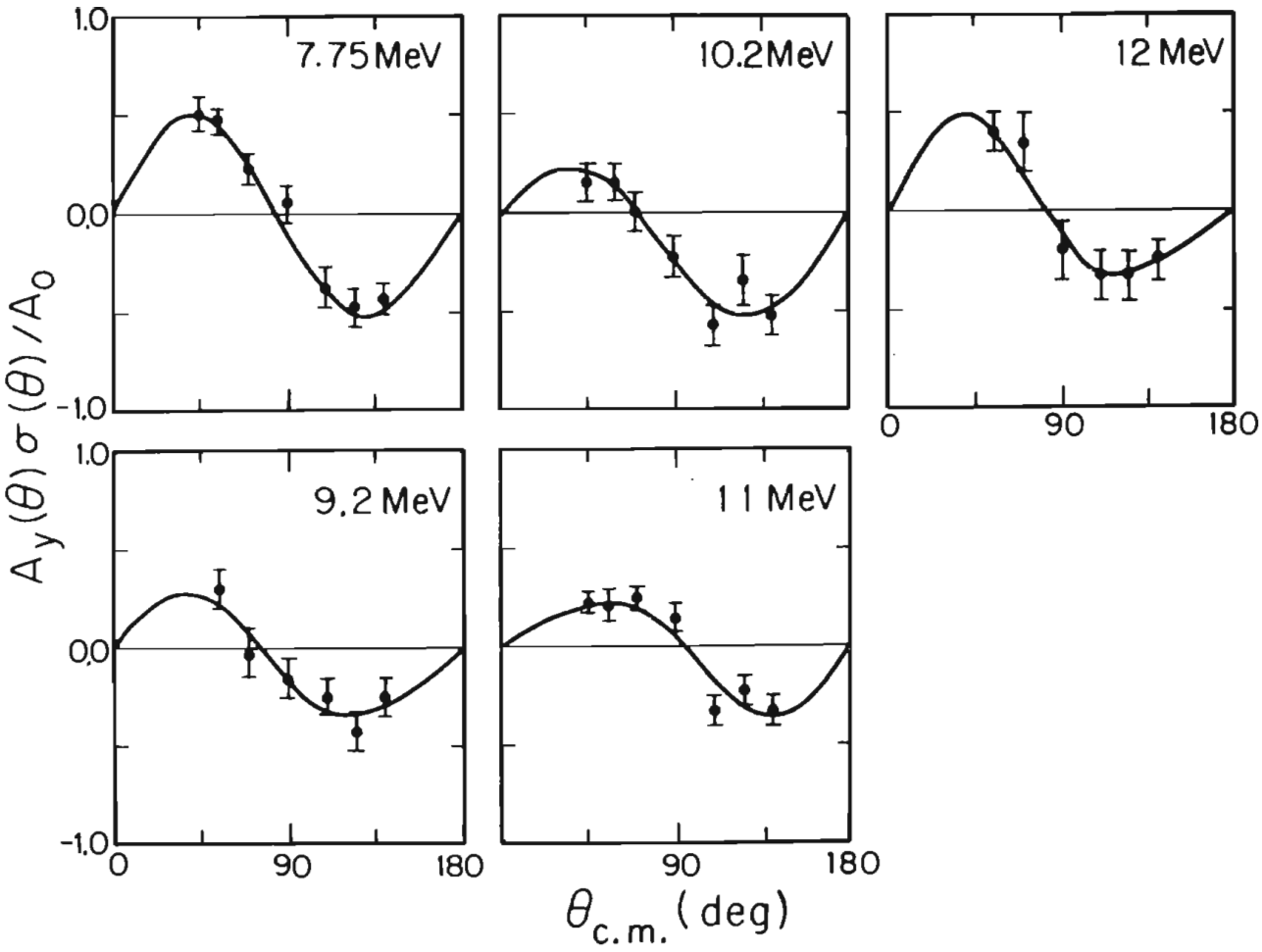

Figure 4-2 Observed angular distributions of analyzing power for the $^{13}C(n_{pol},\gamma_0)^{14}C$ reaction at neutron energies of 7.75, 9.2, 10.2, 11 and 12 MeV. The fits are through $k_{max} = 3$.

4-b Legendre Function Expansions of Cross Section. The center-of-mass angular distributions of cross section were fit by a Legendre function expansion via a weighted least squares [Bevi69]. The expansion was of the form

$$4\text{-}4 \qquad \sigma(\theta) = \sum_{n=0}^{n_{max}} A_n P_n(\cos\theta)$$

where the A_n's are the fitting coefficients and the $P_n(\cos\theta)$'s are the Legendre functions defined in AMS-55 [Abra64 22.7.10]. The shape of the angular distribution was of major interest here so the cross section was normalized to A_0 to yield:

$$4\text{-}5 \qquad \frac{\sigma(\theta)}{A_0} = \sum_{n=0}^{n_{max}} a_n P_n(\cos\theta)$$

where $a_n = A_n/A_0$, e.g., $a_0 = 1$.

The multipolarity (L) of the radiation determines the maximum possible non-zero Legendre coefficients such that $n_{max} \leq 2L$. Thus for quadrupole radiation $n_{max} \leq 4$. One could set nmax to four and blindly accept the least squares coefficients, however, one can test the significance of these coefficients. The cross section over the angular range $0^o \leq \theta \leq 180^o$ must be non-negative, thus at 12 MeV the fit with n_{max} of four was rejected because it produced negative cross sections as θ approaches zero. The uncertainties of the coefficients can suggest if

a term should be included. For example, at 11 MeV the P_4 coefficient was 0.04(6) so that the uncertainty in the coefficient overlaps with zero, suggesting that the P_4 term may be dropped from the analysis.

Bevington [Bevi69, p. 201] describes an F-test to determine if an additional term in a fit is statistically significant. The F-test measures the improvement in chi-square with the addition of a term. The level of the test must be specified, say 5 %. This means that 5 % of the time the F-test will accept a term in the fitting function when it does not exit in the parent or true function. As an example one can test the significance of the $n_{max} = 3$ term at 11 MeV. The fit with $n_{max} = 2$ has a reduced chi-square of 1.6. The fit with $n_{max} = 3$ has a reduced chi-square of 0.2. The ratio of of the difference in chi-squares over the latter chi-square is 7., with 5 degrees of freedom. From Table C-5 [Bevi69] the 5 % F-value for 5 degrees of freedom is 6.6. Because $7 \geq 6.6$ the a_3 term is accepted as statistically significant. If the chi-square ratio was less than the F-value found in Bevington's Table C-5, the a_3 term would be rejected. The only F-test significant a_3 term is the one measured at 11 MeV. At the other energies the angular distribution of cross section fits are F-test significant only through $n_{max} = 2$.

The Legendre coefficients for the angular distributions of cross section for the fits with $n_{max} = 2$ through 4 can be found in Tables C-3 through C-5. The cross section was also corrected for finite-geometry effects, §5-b. The corrected Legendre coefficients are also shown in Tables C-3 through C-5. The reduced chi-square of the fits may be found

in the tables as well. The solid lines through the angular distribution of cross section data in Figure 4-1 are the Legendre function expansions. Figure 4-3 shows the Legendre coefficients as a function of energy with n_{max} set to 3. This value was chosen for convenience in comparing the $^{13}C(n,\gamma_0)^{14}C$ angular distribution data with Turner's $^{13}C(p,\gamma_1)^{14}N^*$ (0^+ T=1) angular distribution data [Turn80].

4-c Legendre Function Expansions of the Analyzing Power, Cross Section Product. The angular distributions of the analyzing power-cross section product were fit by an expansion of the form

$$4\text{-}6 \qquad \frac{A_y(\theta)\ \sigma(\theta)}{A_0} = \sum_{k=1}^{k_{max}} b_k\ P_k^1(\cos\theta)$$

where the b_k's are the fitting coefficients and the $P_k^1(\cos\theta)$ are the Legendre functions of order 1 (also known as the associated Legendre polynomials) as defined by Baldin [Bald61]. It should be noted that Abramowitz in AMS-55 [Abra64] has included a factor of $(-1)^m$ in his definition of P_n^m [8.8.6] that is missing in Baldin's.

As in §4-b the multipolarity (L) of the radiation determines the maximum possible non-zero Legendre coefficient such that $k_{max} \leq 2L$. With quadrupole radiation $k_{max} \leq 4$. The angular distributions of analyzing power over the angular range $0^o \leq \theta \leq 180^o$ must be between -1 and 1. Thus at 12 MeV the fit with k_{max} of 3 was rejected because it produced an analyzing power greater than 1 in the region about 30^o. The uncertainties of the coefficients can suggest if a term should be

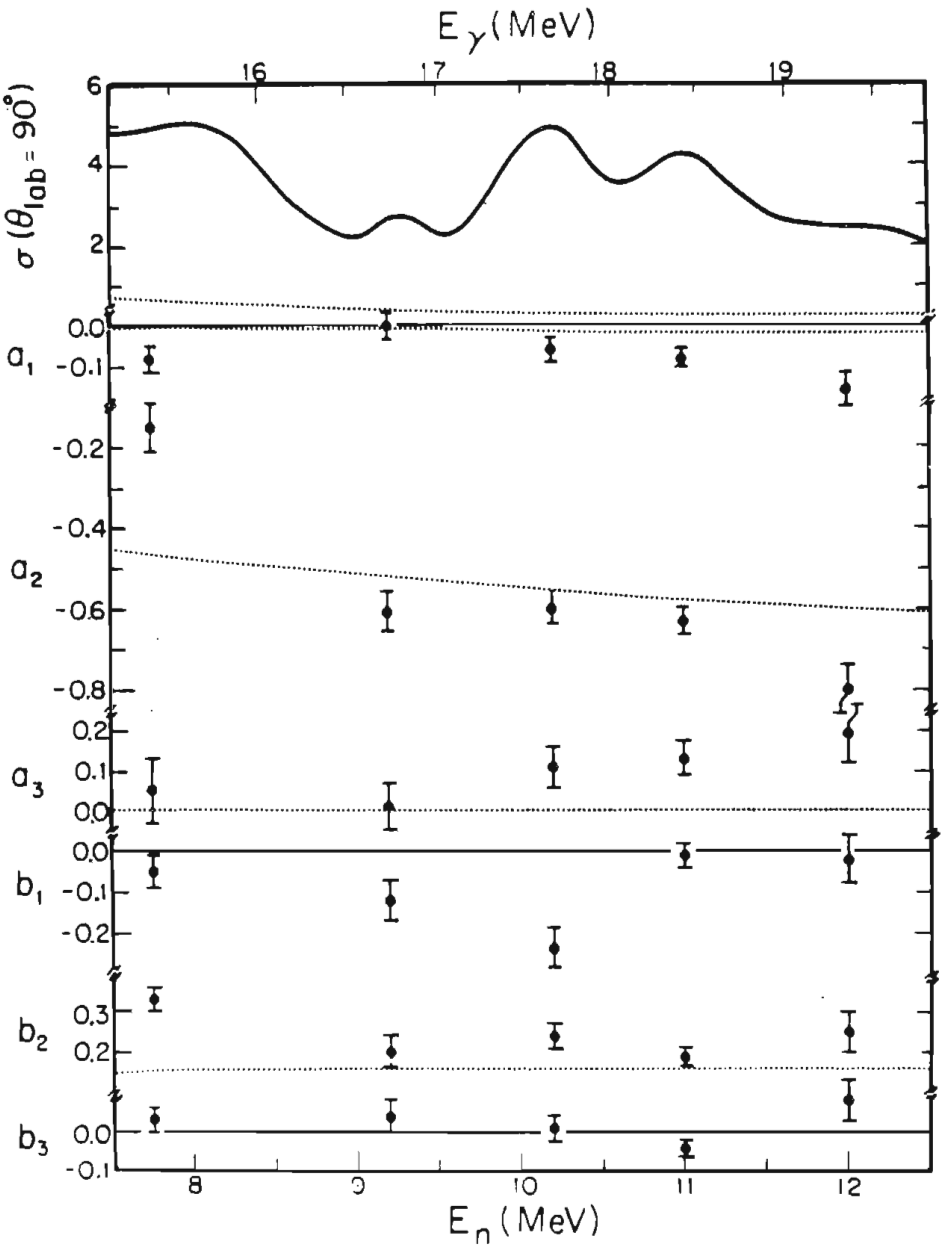

Figure 4-3 Legendre expansion coefficients for the measured angular distributions for the $^{13}C(n_{pol},\gamma_0)^{14}C$ reaction. The dotted lines are a direct, §7-b, calculation of the coefficients.

included in the fitting function. For example at 9.2 MeV the b_4 coefficient was found to be 0.03(5). This suggests that the $k_{max} = 4$ term should be dropped from the fitting function. The F-test described in §4-b may be also be applied to the analyzing power, cross section product fits. At all energies the angular distributions of the analyzing power-cross section product fits are F-test significant only through $k_{max} = 2$.

The Legendre coefficients for the angular distribution of the analyzing power, cross section product for fits with $k_{max} = 2$ through 4 can be found in Tables C-3 though C-5. The analyzing power was also corrected for finite-geometry effects, §5-b. The corrected coefficients are also shown in Tables C-3 though C-5. The reduced chi-square of the fits may also be found in the tables. The solid lines though the analyzing power, cross section product data in Figure 4-2 are its Legendre function expansions. Figure 4-3 shows the Legendre coefficients as a function of energy with $k_{max} = 3$. This value was chosen for convenience in comparing the $^{13}C(n_{pol},\gamma_0)^{14}C$ data with Turner's $^{13}C(p_{pol},\gamma_1)^{14}N^*$ (0^+ T=1) data [Turn80].

In §5-b the analyzing power was needed instead of the product $A_y(\theta)\ \sigma(\theta)$. From Equation 4-6 one may obtain $A_y(\theta)$:

$$A_y(\theta) = \frac{A_0}{\sigma(\theta)} \sum_{k=1}^{k_{max}} b_k P_k^1(\cos\theta). \qquad 4\text{-}7$$

The Legendre expansion for the cross section may now be substituted into Equation 4-7 to yield A_y in terms of the measured expansions alone, see Equation 4-8.

4-8

$$A_y(\theta) = \frac{\sum_{k=1}^{k_{max}} b_k P_k^1(\cos\theta)}{\sum_{n=0}^{n_{max}} a_n P_n(\cos\theta)}$$

The solid line through the data of Figure 5-4 is the evaluation of Equation 4-8 from the Legendre expansion coefficients.

5 FINITE-GEOMETRY CORRECTIONS

5-a Correction Method. To interpret the results of the $^{13}C(n_{pol},\gamma_0)^{14}C$ measurements, several corrections were made to the data. These corrections which were due to the finite extent of the neutron source, sample and detector may be grouped into three categories. First, the neutron flux was averaged over the volume of the sample, and the γ-ray flux was averaged over the volume of the detector. Second, the effect of the neutron and γ-ray attenuation was evaluated. Finally, the multiply-scattered neutron flux was added to the primary flux. The differential γ-ray count rate dg, observed with a detector at an angle of θ_d was expressed as

$$5\text{-}1 \qquad dg = \sigma_{n,\gamma}(\theta_\gamma)\ \sigma_{d,n}(\theta_{d,n})\ \rho_s\ \rho_g\ T_{d,n}\ T_\gamma\ \varphi_d\ \varepsilon_d \cdot r_{gs}^{-2}\ r_{sd}^{-2}\ dV_g\ dV_s\ dA_d$$

where $\sigma_{n,\gamma}(\theta_\gamma)$ was the neutron capture cross section for a γ ray in the θ_γ direction. In general θ_γ was not equal to θ_d, the direction from the center of the sample to the center of the face of the detector. The source reaction cross section, $\sigma_{d,n}(\theta_{d,n})$, was the $^2H(d,n)^3He$ cross section for the production of neutrons in the $\theta_{d,n}$ direction. The nuclear number densities of the deuterium in the gas cell and the sample were represented by ρ_g and ρ_s. The attenuation of the neutron and γ ray flux was accounted for by the transmission functions $T_{d,n}$ and T_γ. The transmission function was evaluated by $T = \exp[\ -\rho_s\ \sigma\ l\ ]$, where σ was the neutron total cross section [Auch79], σ_n, or the γ-ray total cross section [Stor70], σ_γ, and l is the distance in the sample through which

the particle passes. ϕ_d was the deuteron flux in the gas cell. The variable r_{gs} was the distance from the site of the $^2H(d,n)$ reaction in the gas cell to the (n,γ) reaction in the sample. The distance from the site of the (n,γ) reaction in the sample to the site of the interaction in the detector was r_{sd}. Both r_{gs} and r_{sd} accounted for solid angle effects. This differential count rate was integrated over the volumes of the gas cell and sample and the area of the face of the detector.

A Monte Carlo code, Fixer, was written to calculate these finite-geometry effects. The deuteron beam in the gas cell was modeled, see Figure 5-1, by a frustum having an initial radius of $r_{g,i}$ and a final radius of $r_{g,f}$ ($r_{g,i} \leq r_{g,f}$). Although the deuteron beam's cross sectional area increased as it passed through the gas cell, any radial momentum was ignored. The beam slowed in the gas cell, losing an energy of δE_g so that $E_g(z) = E_d - (z/l_g) \delta E_g$. In this expression E_d was the incident deuteron beam energy, l_g was the gas cell length and z is the distance the deuteron passes through the before undergoing the (d,n) reaction. A Gaussian spread in deuteron beam energy was included with a mean energy of $E_g(z)$ and a constant standard deviation of ΔE_g. Only the sample is assumed to attenuate the neutron and γ-ray flux.

The sample was a cylinder of radius r_s and height h_s with its center a distance l_{gs} from the end of the gas cell. It contained a uniform density of ρ_s nuclei per unit volume. The total neutron cross section of the sample element was used to calculate attenuation of the

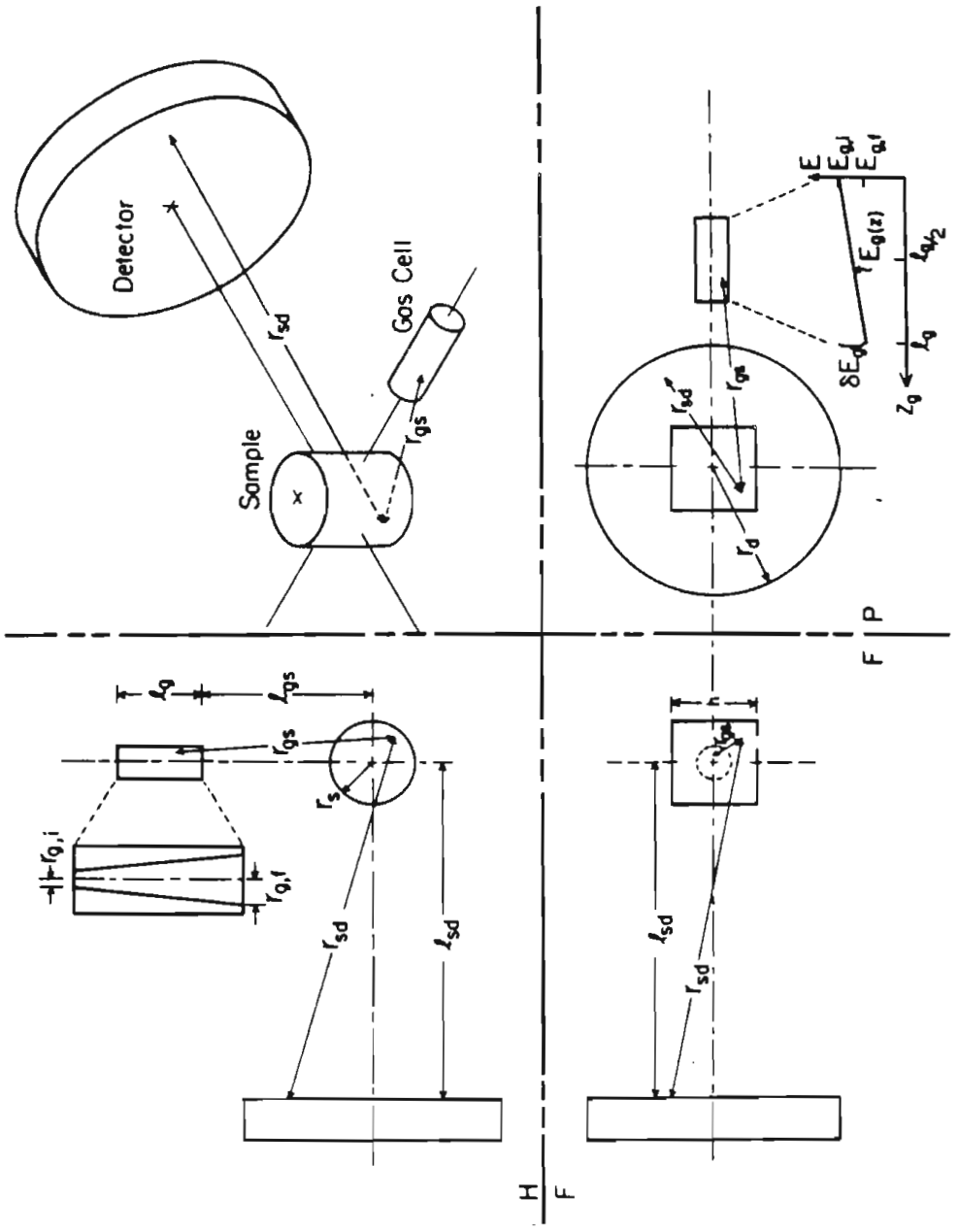

Figure 5-1 Third-angle and isometric projections of the geometry modeled by Fixer.

neutron beam in the sample; however, only elastically scattered neutrons re-entered the calculation by multiple-scattering. Neutrons from all other processes were ignored.

The γ-ray detector was modeled as a disk detector of radius r_d at a distance l_{sd} from the center of the sample. It had a position independent efficiency of ε_d.

The neutron multiple-scattering effects were introduced by including the neutron flux from elastic scattering. Neutrons may undergo several elastic scattering events before the (n,γ) reaction occurs. Each higher order set of scattered neutrons (single, double, triple, etc.) scattered depends upon the previous orders, e.g., the amount of triple scattering depends upon the double scattering flux. The factor [Beye81] used to account for multiple scattering is

$$5\text{-}2 \qquad \sum_{j=1}^{\infty} \prod_{i=1}^{j} T_{n,i}\, \sigma_{n,n}(\theta_{n,i})\, \rho_s\, r_{s_{i-1},s_i}^{-2}\, dV_{s_i}$$

where $\sigma_{n,n}(\theta_{n,i})$ was the neutron elastic scattering cross section for ^{13}C at an angle of $\theta_{n,i}$. The distance from the previous scattering site to the current site was r_{s_{i-1},s_i}. Each order of scattering required another integration over the sample. Thus the differential count rate is

$$5\text{-}3 \qquad dg = \sum_{j=0}^{\infty} \sigma_{d,n}(\theta_{d,n})\ \rho_g\ T_{d,n}\ \phi_d\ r_{gs}^{-2}$$

$$\cdot \prod_{i=1}^{j} \left[\sigma_{n,n}(\theta_{n,i})\ \rho_s\ T_{n,i}\ r_{s_{i-1},s_i}^{-2}\ dV_{s_i} \right]$$

$$\cdot\ \sigma_{n,\gamma}(\theta_\gamma)\ \rho_s\ T_\gamma\ r_{sd}^{-2}\ dV_g\ dV_s\ \varepsilon_d\ dA_d$$

where the j = 0 term represents the γ ray count rate from the primary, unscattered neutron flux.

The neutron capture experiment determined what is called the observed cross section, σ_{obs}, which had all the finite-geometry effects included. The true cross section was deduced from this observation and knowledge of the finite-geometry effects. The process used was similar to that used in neutron scattering studies. A guess was made of the true cross section, σ_{guess}, and the corresponding observed cross section, σ_{pred}, was calculated by Fixer. The predicted cross section was compared with σ_{obs} and a new guess was obtained via

$$5\text{-}4 \qquad \sigma_{guess}^{i+1} = \frac{\sigma_{obs}}{\sigma_{pred}^{i}}\ \sigma_{guess}^{i}.$$

This correction occurred at each angle measured. The iteration continued until $\sigma_{obs} - \sigma_{pred}^{i}$ was small. The initial cross section guess, σ_{guess}^{0}, was taken to be σ_{obs}.

In practice only one iteration was required so that the iteration scheme was modified to be

5-5
$$\sigma_{true} = \frac{\sigma_{obs}}{\sigma_{pred}} \sigma_{obs} = R\,\sigma_{obs}$$

Here σ_{obs} was taken to be the initial Legendre function expansions to the angular distributions of cross section. Each data point was modified by the factor R and the modified angular distributions of cross section was refit to Legendre functions, §4-b, or the transition matrix elements, §6.

5-b Angular Distribution Corrections. The correction factor, $R = \sigma_{obs}/\sigma_{pred}$, was fairly constant as a function of angle for unpolarized beam, see Figure 5-2. Hence, there were no significant effects on the shape of the angular distribution of cross section. The upper plot of Figure 5-3 shows the corrected angular distribution of cross section with its Legendre expansion. The data points on the lower plot show the difference between the corrected and uncorrected data. The scale on the lower plot was expanded by a factor of ten. The mean correction represents five percent of an error bar. The fits in the lower plot do not resemble the data implying that the finite-geometry corrections are smaller than the random behavior of the data points. Finite geometry had no significant effect on the normalized cross section of the $^{13}C(n,\gamma_0)^{14}C$ reaction measurements.

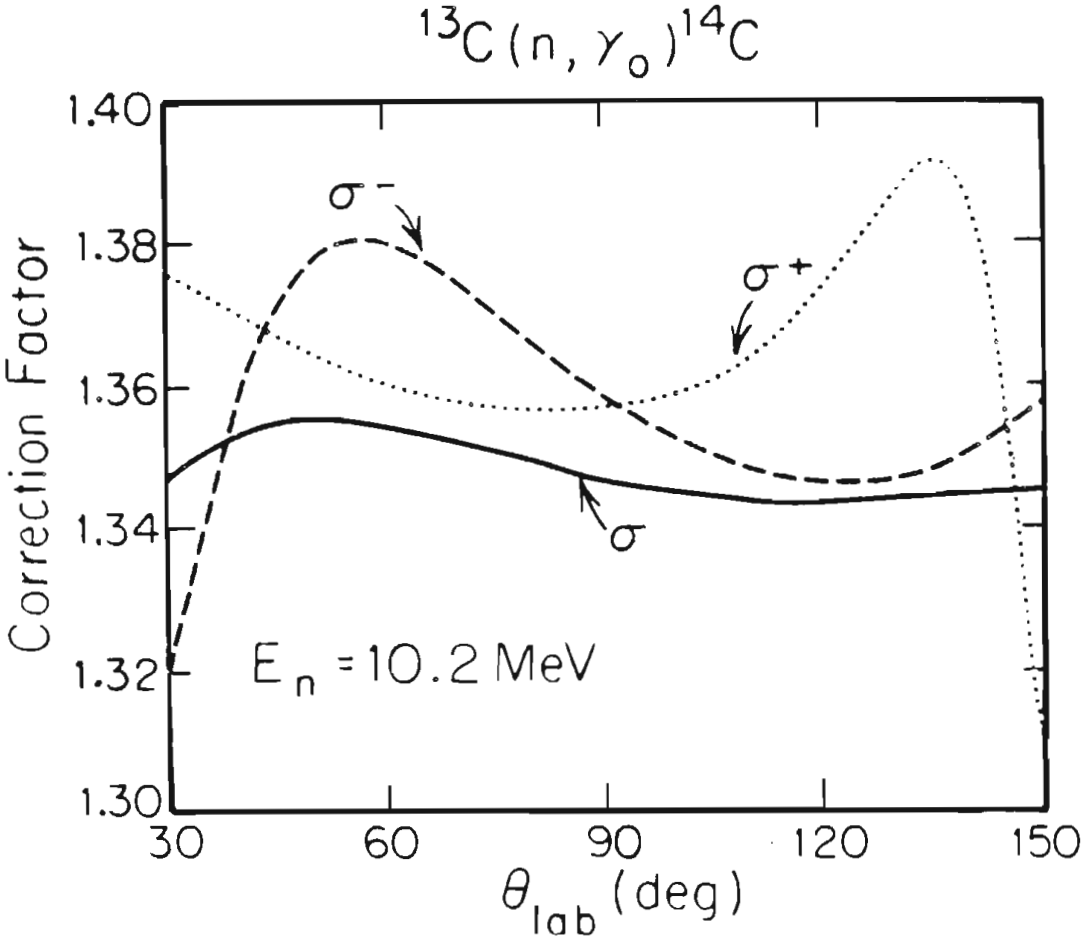

Figure 5-2 Example of the finite-geometry correction ratio as a function of angle. Both polarized and unpolarized beam correction ratios are displayed.

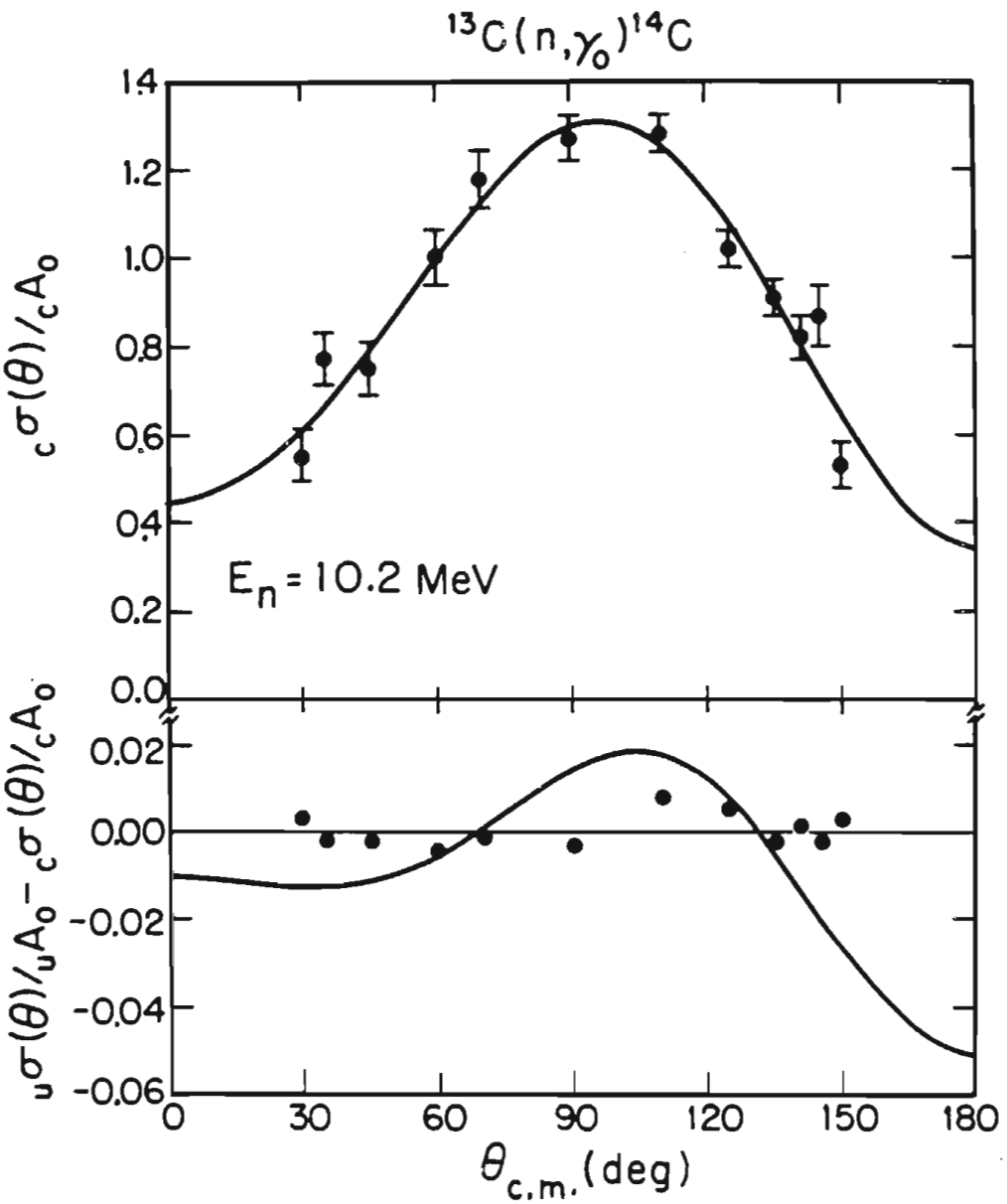

Figure 5-3 Finite-geometry corrected cross section and the difference with the uncorrected data. The curves are a polynomial fit to the data and the difference between the corrected and uncorrected fits.

The finite-geometry effects on analyzing powers were also calculated using Fixer. Fixer only calculates the effects on cross section, so the analyzing power was decomposed into a spin-up cross section, σ^+, and a spin-down cross section, σ^-. The iteration scheme was applied to unpolarized, spin-up and spin-down cross sections. The analyzing power was reformulated from σ^+ and σ^- and refit to associated Legendre polynomials. An example of the correction factor as a function of angle for spin-up and spin-down may be found in Figure 5-2.

The upper plot of Figure 5-4 shows the corrected angular distribution of analyzing power with its Legendre expansion. The data points on the lower plot show the difference between the corrected and uncorrected data. The mean correction represents ten percent of an error bar. As with the angular distributions of cross section, the fit in the lower plot does not resemble the data implying that the finite-geometry corrections to the angular distributions of analyzing power are smaller than the random behavior of the data points. The finite geometry had no significant effect on the analyzing power of the $^{13}C(n_{pol},\gamma_0)^{14}C$ reaction measurements.

5-c Excitation Function Corrections. The correction ratio at $\theta_{lab} = 90^o$ as a function of neutron energy may be found in Figure 3-4. The positive slope corresponded to the narrowing of the forward peak of the neutrons emitted from the $^2H(d,n)^3He$ reaction. The total neutron cross section used to calculate attenuation and multiple scattering was generally constant over the energy region of 6 to 14 MeV. The γ-ray attenuation was falling in this energy region which would have tended to

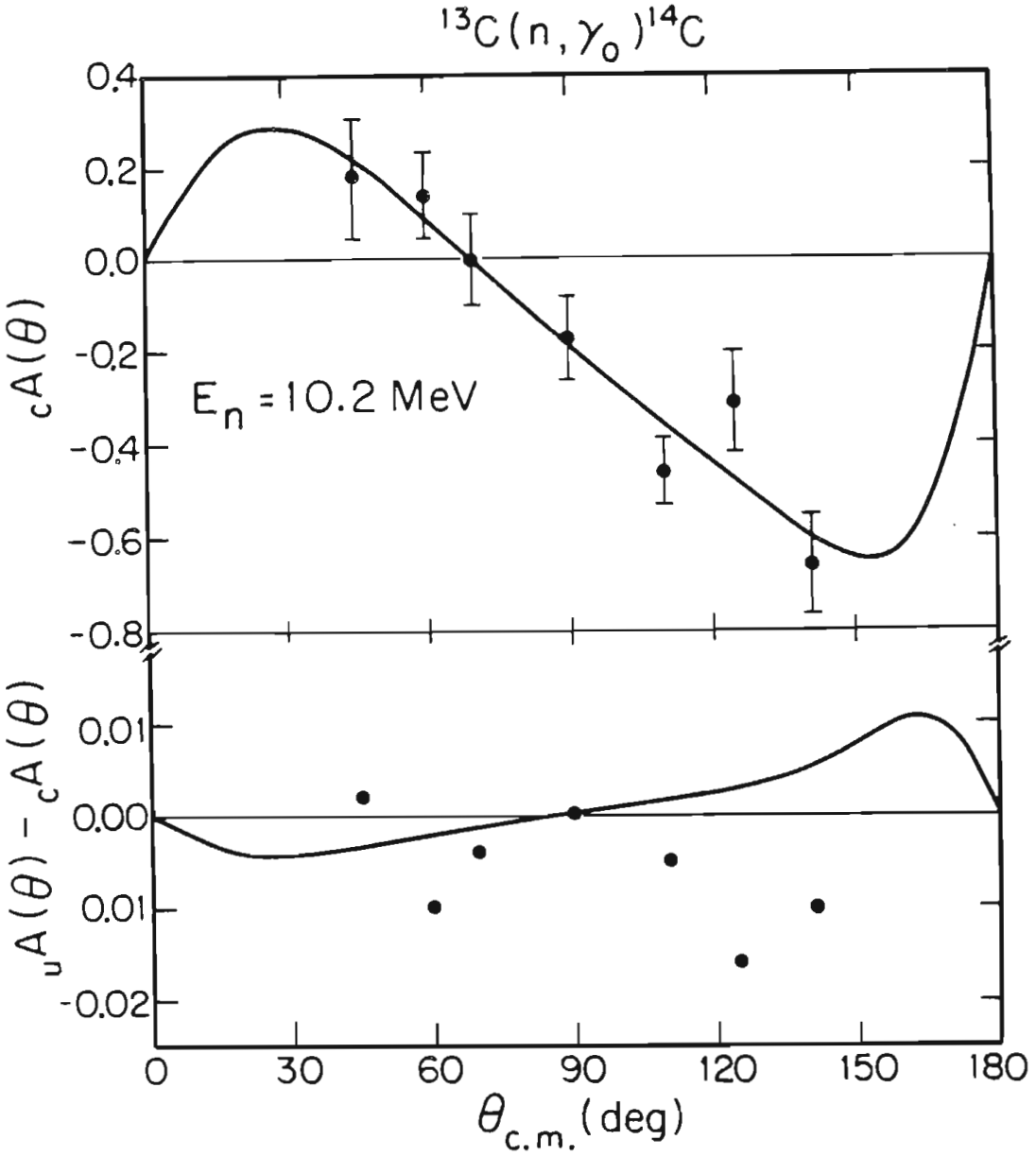

Figure 5-4 Finite-geometry corrected analyzing power and the difference with uncorrected data. The curves are a polynomial fit to the data and the difference between the corrected and uncorrected fits.

counteract the peaking of the $^{2}H(d,n)^{3}He$ reaction; however, the effect was too small to have any observable affect.

6 TRANSITION MATRIX ELEMENT ANALYSIS

6-a Non-Linear Analysis. The Legendre function expansions of the angular distributions of cross section and the product of analyzing power and cross section yield qualitative information about the multipolarity composition of the γ radiation. The non-zero odd terms in the linear expansions of §4 indicate the presence of non-E1 radiation. However, from just those Legendre expansion coefficients it is impossible to determine the magnitude of the non-E1 radiation. That is, the Legendre expansion representation is the wrong representation to infer the magnitude of the different multipolarities of the radiation. A more appropriate representation for decomposing the different multipolarities of the radiation is the transition matrix elements, described most recently by Seyler and Weller [Sey179]. Equations 6-4, 6-5 and 6-6 relate the Legendre expansion coefficients to the transition matrix elements. These matrix elements are complex valued, and will be expressed in polar form with a magnitude and a phase.

Two methods were used to calculate the transition matrix elements. The first method uses the measured Legendre expansion coefficients and solves the equations. For example if the coefficients are labeled y_i and the transition matrix elements are labeled x_j Equation 6-4 may be written schematically as

$$
\begin{aligned}
y_1 &= f_1(x_1, x_2, x_3) \\
y_2 &= f_2(x_1, x_2, x_3) \\
y_3 &= f_3(x_1, x_2, x_3)
\end{aligned}
\qquad 6\text{-}1
$$

where the f_i's are non-linear functions of the x_j's. The set of equations is rearranged so that one solves equations in the form of Equation 6-1 by searching for the zeros of Equation 6-2.

$$
\begin{aligned}
0 &= f_1(x_1,x_2,x_3) - y_1 \\
0 &= f_2(x_1,x_2,x_3) - y_2 \\
0 &= f_3(x_1,x_2,x_3) - y_3
\end{aligned} \qquad 6\text{-}2
$$

The E1 analysis, §6-b, of the measured angular distributions used this method. The non-E1 radiation was assumed to be a perturbation and was ignored for this analysis. The finite-geometry corrected Legendre expansion coefficients were used and the equations were solved.

The above method could be used for any transition matrix element analysis; however, there are some disadvantages in using it for non-E1 analysis. One disadvantage is that the equations may not have any zeros. The "a" and "b" coefficients are independently calculated, thus the two approximations may be inconsistent. Also the Legendre expansions may violate the physical constraints of cross section and analyzing power. The transition matrix elements contain these constraints. In these cases there are no solutions. The best one can do is to find matrix elements that produce acceptably small values for the right-hand-side of Equation 6-2 instead of zeros. In terms of the calculus of variation, this method first optimizes and then applies the constraints. There is also the problem of what terms should be included in the Legendre expansions of the angular distributions. For example,

none of the b_3 terms in the expansions are statistically significant so that using these b_3 coefficients is, at the least, questionable. It is also impossible to interpret the setting of b_3 to zero in terms of the multipolarity of the radiation.

Non-linear least squares [Bevi69] provides a second method to determine the transition matrix elements. As with any least squares procedure one begins by defining the chi-square:

$$6\text{-}3 \qquad \chi^2 = \sum_i \frac{1}{\Delta_i^2} \left[\sigma(\theta_i) - \sigma'(\theta_i) \right]^2 + \sum_j \frac{1}{\Delta_j^2} \left[\frac{A_y(\theta_j)\sigma(\theta_j)}{A_0} - \frac{A'_y(\theta_j)\sigma'(\theta_j)}{A_0} \right]^2$$

Here "i" varies over all the cross section measurements at an energy and "j" varies over all the analyzing power measurements. Δ_i is the uncertainty in the measured cross section at θ_i and Δ_j is the uncertainty in the measured values of $[A_y(\theta_j)\sigma(\theta_j)]/A_0$. The uncertainty in A_0 is small enough that it and any of its covariances are ignored. The fitted value of the cross section, $\sigma'(\theta_i)$, is calculated using Equation 4-4. The fitted value of $[A'_y(\theta_j)\sigma'(\theta_j)]/A_0$ is calculated using Equation 4-6. The process begins by guessing a set of values for the desired matrix elements. The corresponding Legendre expansion coefficients are calculated by Equations 6-4, 6-5 or 6-6. The chi-square is evaluated using Equation 6-3. Note that the reduced chi-square is plotted in the figures and presented in the tables. The matrix elements values are varied by the non-linear least squares code

and the chi-square recalculated. This process is continued until a minimum chi-square is found. This method is implemented by a code, Dataamp, written by C.P. Cameron [Came77].

Non-linear least squares provides a solution to the problems of the first method. The cross section and the product of analyzing power and cross section are fit in one process so there can be no inconsistencies in their fits. The number of terms in the Legendre expansions is fixed by the selection of what matrix elements to include in the fit. This just transfers the problem of statistical significance to the matrix elements themselves. However these uncertainties are in terms of the multipolarities of the radiation, which is just what is desired. Transition matrix elements may be dropped from the fitting function and interpreted directly in terms of the radiation's multipolarities. Finally, by fitting the matrix elements directly to the data, the physical constraints are satisfied before the chi-square is calculated. Thus this method constrains first and then optimizes. The non-linear least squares method picks the solution with the minimum chi-square from all possible physical solutions. The first method finds the minimum chi-square, even if it is not a physical solution, and then applies the physical constraints when solving Equation 6-2. The application of the constraints chooses, in some sense, the closest physical solution to the minimum chi-square. In general there is no reason to expect that the two methods of solution will produce the same result. The preferred order is to first constrain the solution and then to optimize. The non-linear least squares method was used in the analysis of non-E1 radiation.

6-b E1 Analysis. The dominant E1 radiation consists of two complex transition matrix elements, $s_{1/2} \exp[\, i\, \phi_{s_{1/2}}\,]$ and $d_{3/2} \exp[\, i\, \phi_{d_{3/2}}\,]$, where the complex values are expressed in polar form. The resulting angular distribution equations are

6-4
$$a_0 = s_{1/2}^2 + 2\, d_{3/2}^2$$

$$a_2 = -\,2\, s_{1/2}\, d_{3/2} \cos[\, \phi_{d_{3/2}} - \phi_{s_{1/2}}\,] - d_{3/2}^2$$

$$b_2 = -\, s_{1/2}\, d_{3/2} \sin[\, \phi_{d_{3/2}} - \phi_{s_{1/2}}\,]$$

Only the relative phase, $\phi_{d_{3/2}} - \phi_{s_{1/2}}$, may be determined. There are three non-linear quadratic equations with three unknowns, $s_{1/2}$, $d_{3/2}$ and $\phi_{d_{3/2}} - \phi_{s_{1/2}}$.

The equations were solved and the results are presented in Table 6-1 and Figure 6-1. The quadratic nature of the equations results in two solutions. One solution is characterized by a dominant $d_{3/2}$ matrix element and the other solution is characterized by a dominant $s_{1/2}$ element. In Figure 6-1 the dominant $d_{3/2}$ is represented by the circles and the triangles represent the $d_{3/2}$ matrix elements for the dominant $s_{1/2}$ solution. Weller and others [Well78] have shown that a simple direct model provides a method for choosing the correct solution. More recently Snover and others [Snov80a] have shown that this method is valid, at least in this mass region, by measuring the E1 radiation interference with a known narrow M1 resonance. The solid lines in Figure 6-1 were the result of a direct calculation [Cota78] of

Table 6-1 E1 solutions for the $^{13}C(n_{pol},\gamma_0)^{14}C$ reaction. Equation 6-4 was solved for $\sigma(s_{1/2})$, $\sigma(d_{3/2})$ and $\phi_{d_{3/2}} - \phi_{s_{1/2}}$. The quadratic nature of the E1 equations resulted in a pair of solutions for each angular distribution. The cross sections are defined as:

$$\sigma(s_{1/2}) = |s_{1/2}|^2$$

$$\sigma(d_{3/2}) = 2\,|d_{3/2}|^2.$$

E_n (MeV)	$\sigma(s_{1/2})$ (%)	$\sigma(d_{3/2})$ (%)	$\phi_d - \phi_s$ (deg)
7.75	36(9)	64(10)	-104(6)
	68(10)	32(9)	-90(6)
9.2	9(5)	91(5)	-66(6)
	75(7)	25(5)	-36(7)
10.2	14(4)	86(5)	-70(5)
	71(5)	29(5)	-46(5)
11.	10(2)	90(3)	-65(4)
	73(3)	27(3)	-37(4)
12.	25(8)	75(8)	-46(9)
	49(9)	51(9)	-39(9)

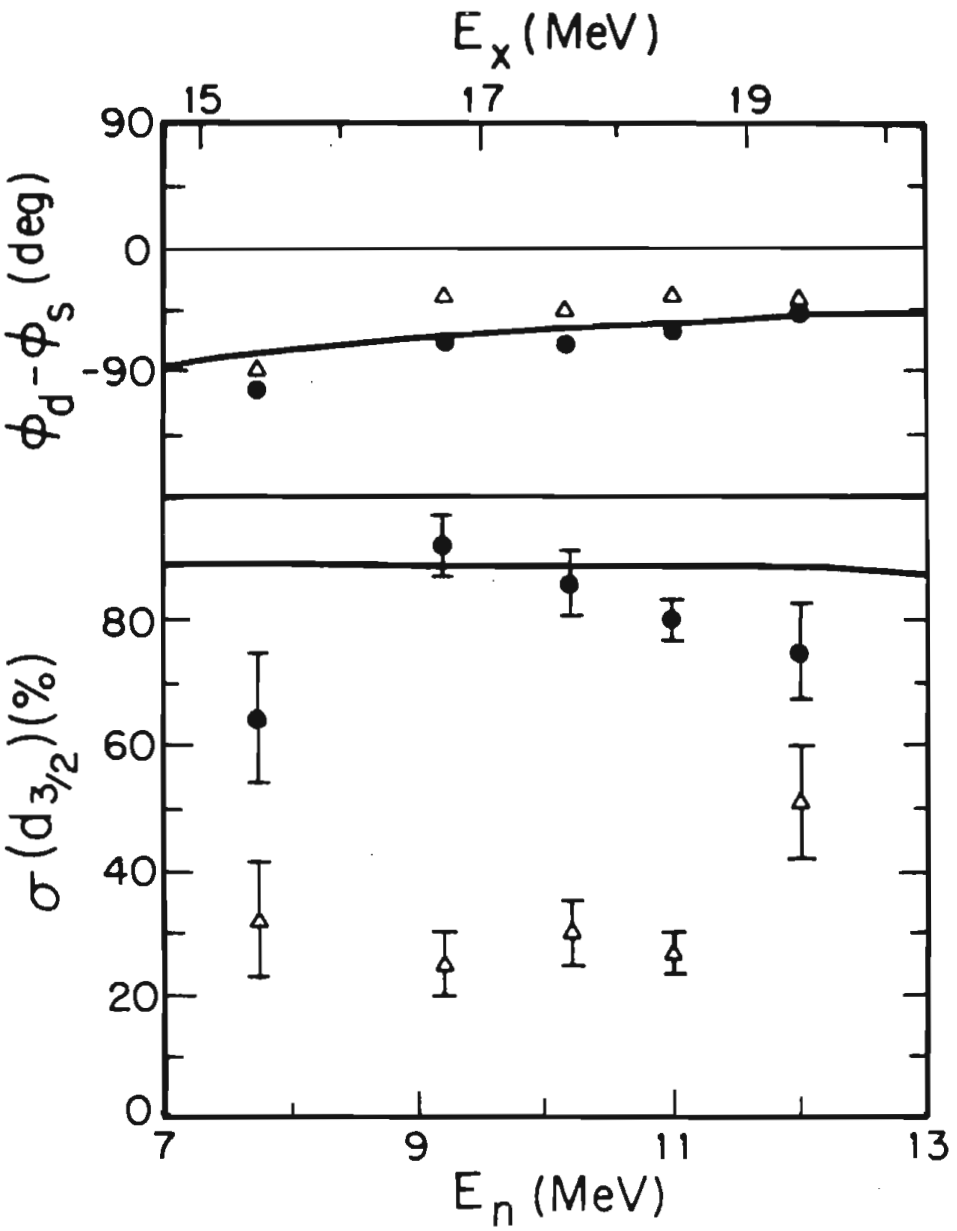

Figure 6-1 E1 solutions for the $^{13}C(n_{pol},\gamma_0)^{14}C$ reaction. Equation 6-4 was solved for $\sigma(s_{1/2})$, $\sigma(d_{3/2})$ and $\phi_{d_{3/2}} - \phi_{s_{1/2}}$. The $d_{3/2}$ cross section is plotted for the pair of solutions. The solid lines are the result of a direct model calculation and indicate the physical solution.

the $^{13}C(n,\gamma_0)^{14}C$ reaction. This clearly indicates that the dominant $d_{3/2}$ solution is the physical solution. For the remainder of the transition matrix element analysis, only the dominant $d_{3/2}$ solution was used.

6-c E2 and M1 Analysis. The finite odd terms in the polynomial expansions, see §4-b, indicated the presence of non-E1 radiation. The maximum multipolarity (L_{max}) of the γ radiation defines the maximum Legendre expansion coefficient, such that, $n_{max} = k_{max} = 2\ L_{max}$. For example, quadrupole radiation (L = 2) would have an n_{max} and a k_{max} of four. The non-zero values of a_3 at E_n = 10.2, 11 and 12 MeV suggested that the next step in the analysis should include E1-E2 interference.

For E2 radiation there exist two complex transition matrix elements, $p_{3/2} \exp[\, i\, \phi_{p_{3/2}}\,]$ and $f_{5/2} \exp[\, i\, \phi_{f_{5/2}}\,]$. The resulting E1-E2 angular distribution equations are

6-5
$$a_0 = s_{1/2}^2 + 2\, d_{3/2}^2 + 2\, p_{3/2}^2 + 3\, f_{5/2}^2$$

$$\begin{aligned} a_1 = {} & 3.464\ s_{1/2}\, p_{3/2} \cos[\, \phi_{p_{3/2}} - \phi_{s_{1/2}}\,] \\ & + 0.6928\ d_{3/2}\, p_{3/2} \cos[\, \phi_{p_{3/2}} - \phi_{d_{3/2}}\,] \\ & + 6.235\ d_{3/2}\, f_{5/2} \cos[\, \phi_{f_{5/2}} - \phi_{d_{3/2}}\,] \end{aligned}$$

$$\begin{aligned} a_2 = {} & - d_{3/2}^2 + p_{3/2}^2 + 1.714\, f_{5/2}^2 \\ & - 2\ s_{1/2}\, d_{3/2} \cos[\, \phi_{d_{3/2}} - \phi_{s_{1/2}}\,] \\ & + 0.8571\ p_{3/2}\, f_{5/2} \cos[\, \phi_{f_{5/2}} - \phi_{p_{3/2}}\,] \end{aligned}$$

6-5 Continued.

$$a_3 = -3.464\, s_{1/2}\, f_{5/2} \cos[\phi_{f_{5/2}} - \phi_{s_{1/2}}]$$
$$- 4.157\, d_{3/2}\, p_{3/2} \cos[\phi_{p_{3/2}} - \phi_{d_{3/2}}]$$
$$- 2.771\, d_{3/2}\, f_{5/2} \cos[\phi_{f_{5/2}} - \phi_{d_{3/2}}]$$

$$a_4 = -1.714\, f_{5/2}^2$$
$$- 6.857\, p_{3/2}\, f_{5/2} \cos[\phi_{f_{5/2}} - \phi_{p_{3/2}}]$$

$$b_1 = -1.732\, s_{1/2}\, p_{3/2} \sin[\phi_{p_{3/2}} - \phi_{s_{1/2}}]$$
$$- 1.386\, d_{3/2}\, p_{3/2} \sin[\phi_{p_{3/2}} - \phi_{d_{3/2}}]$$
$$+ 3.118\, d_{3/2}\, f_{5/2} \sin[\phi_{f_{5/2}} - \phi_{d_{3/2}}]$$

$$b_2 = - s_{1/2}\, d_{3/2} \sin[\phi_{d_{3/2}} - \phi_{s_{1/2}}]$$
$$+ 0.7143\, p_{3/2}\, f_{5/2} \sin[\phi_{f_{5/2}} - \phi_{p_{3/2}}]$$

$$b_3 = -1.155\, s_{1/2}\, f_{5/2} \sin[\phi_{f_{5/2}} - \phi_{s_{1/2}}]$$
$$+ 1.386\, d_{3/2}\, p_{3/2} \sin[\phi_{p_{3/2}} - \phi_{d_{3/2}}]$$
$$- 0.2309\, d_{3/2}\, f_{5/2} \sin[\phi_{f_{5/2}} - \phi_{d_{3/2}}]$$

$$b_4 = -1.714\, p_{3/2}\, f_{5/2} \sin[\phi_{f_{5/2}} - \phi_{p_{3/2}}]$$

Only the relative phases may be determined. The amplitudes and relative phases were fit to the angular distribution data via non-linear least squares.

Turner's [Turn80] analysis of the analogue reaction suggested the possibility of multiple E2 solutions; therefore, the chi-square as a function of the E2 cross section was calculated. At 11 MeV the value of $\sigma(f_{5/2})$ was varied from zero to ten percent of the total cross section in one percent steps. The value of $\sigma(p_{3/2})$ was varied from zero to twenty percent of the total cross section in one percent steps. The two E1 amplitudes and the three relative phases were then fit with non-linear least squares to yield the minimum chi-square. This procedure resulted in 231 values of chi-square. Contours of equal chi-square were calculated [Bell77] and may be found in Figure 6-2. Two regions of solution are seen, one with a small amount of σ(E2) and the second with σ(E2) of fifteen to twenty percent. Unfortunately the chi-square surface is too shallow to claim with confidence a true solution at either location. The behavior of chi-square only shows that the E2 cross section is less than twenty percent.

This behavior was surprising because in Turner's analysis of the analogue reaction there exists well defined E2 solutions. The uncertainties in both sets of data are similar. It appears that the amount of E2 radiation is not enough to determine reliably the two E2 amplitudes and relative phases. The natural choice was to drop one of the E2 matrix elements from the analysis. The direct-semidirect calculation, §7-d, predicted that the magnitude of the $f_{5/2}$ matrix element would surpass the magnitude of the $p_{3/2}$ matrix element by up to a factor of ten in this energy region. The analysis was continued using

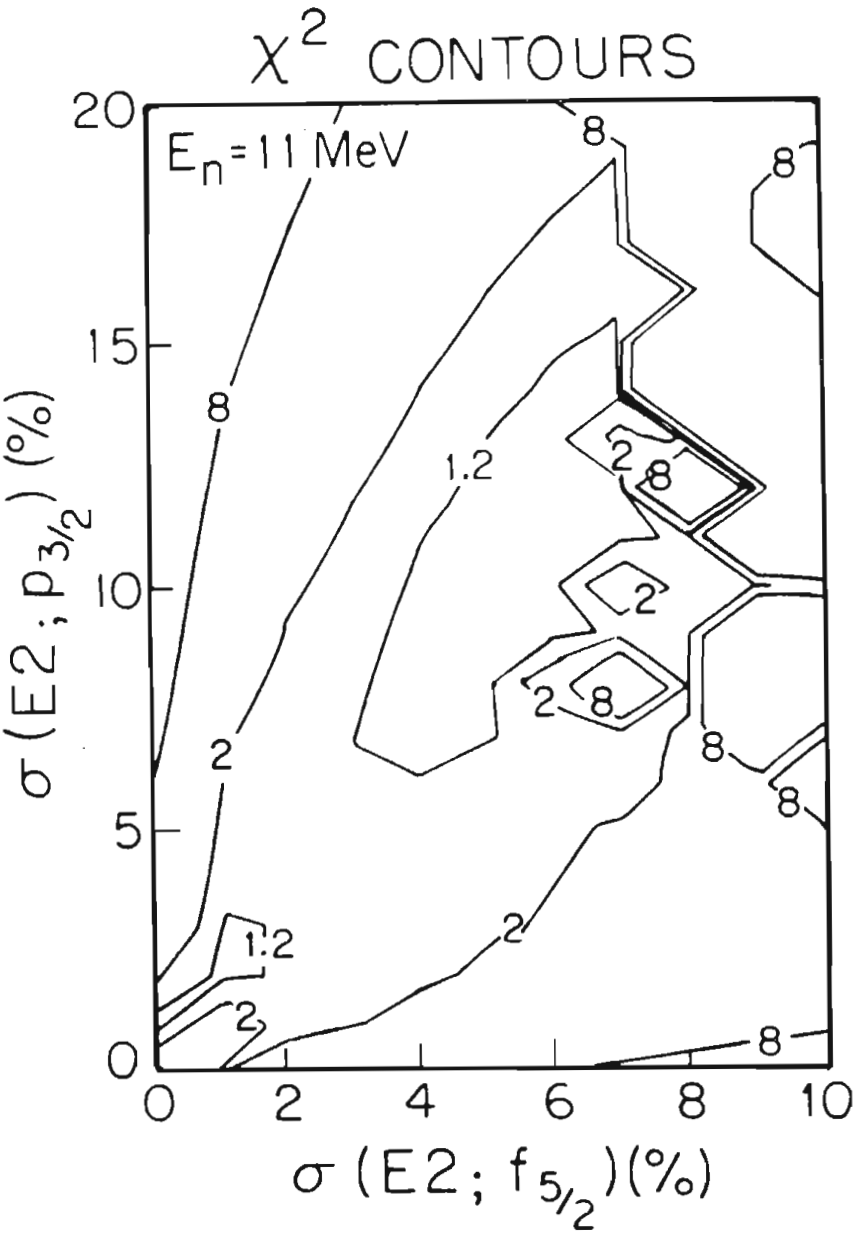

Figure 6-2 Reduced chi-square as a function of E2 cross section at 11 MeV. Two E1 amplitudes and three relative phases were fit via least squares to the angular distribution data using Equation 6-5, while the two E2 amplitudes were held constant. The chi-square surface is discussed in the text.

Table 6-2 E1-E2 solutions for the $^{13}C(n_{pol},\gamma_0)^{14}C$ reaction. Two E1 amplitudes, the $f_{5/2}$ E2 amplitude and two relative phases were fit via least squares to the angular distribution data using Equation 6-5. The cross sections are defined as:

$$\sigma(s_{1/2}) = |s_{1/2}|^2$$
$$\sigma(d_{3/2}) = 2\,|d_{3/2}|^2$$
$$\sigma(f_{5/2}) = 3\,|f_{5/2}|^2.$$

E_n (MeV)	$\sigma(s_{1/2})$ (%)	$\sigma(d_{3/2})$ (%)	$\phi_d - \phi_s$ (deg)	$\sigma(f_{5/2})$ (%)	$\phi_f - \phi_s$ (deg)	χ^2_n
7.75	33.8(81)	66.0(87)	-106(5)	0.2(2)	110(42)	0.6
9.2	9.1(42)	89.8(45)	-66(7)	1.1(8)	207(8)	1.3
10.2	14.9(44)	81.7(50)	-65(5)	3.4(13)	198(6)	1.7
11.	10.0(24)	89.8(27)	-64(4)	0.2(1)	143(28)	1.3
12.	27.7(202)	71.3(207)	-43(7)	1.0(6)	176(27)	2.0

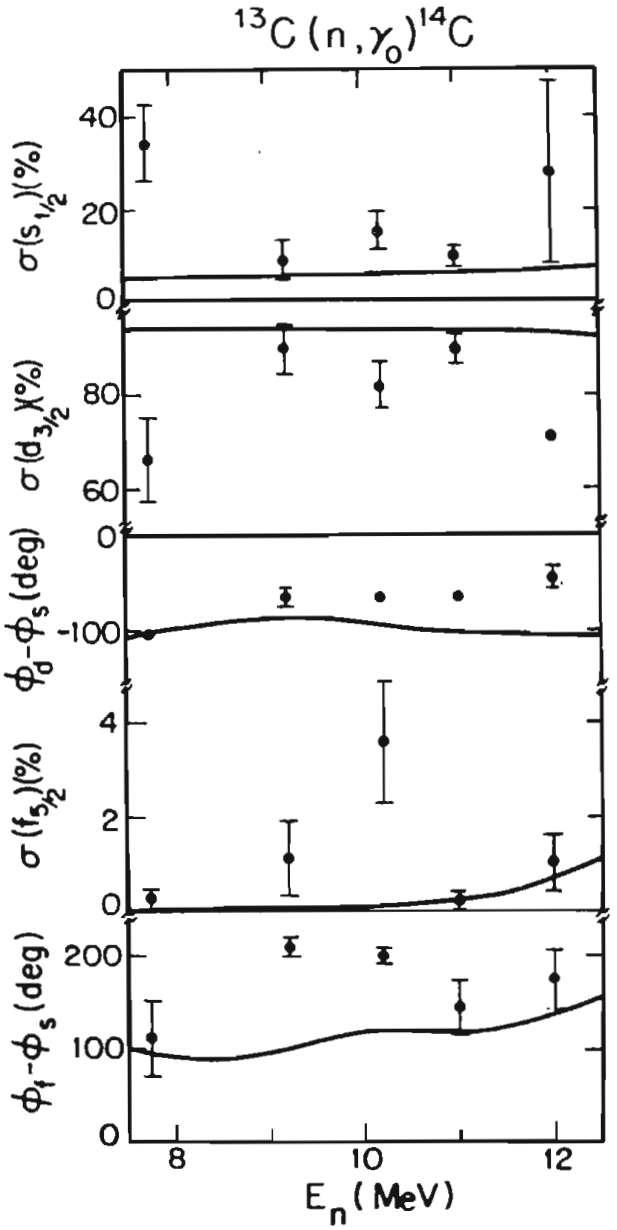

Figure 6-3 E1-E2 solutions for the $^{13}C(n_{pol},\gamma_0)^{14}C$ reaction. Two E1 amplitudes, the $f_{5/2}$ E2 amplitude and three relative phases were fit via least squares to the angular distribution data using Equation 6-5.

the $f_{5/2}$ E2 matrix element alone. Table 6-2 and Figure 6-3 contain the results of that analysis. The corresponding Legendre expansion coefficients may be found in Table D-1.

The large (on the order of one percent) values of the E2 cross section at 9.2 and 10.2 MeV were interesting as they arose from the structure in the b_1 coefficient as a function of energy. There is no corresponding structure in the a_3 or b_3 coefficients. This suggested that the structure in the b_1 coefficient is possibly the result of M1 radiation.

For M1 radiation there exist two complex transition matrix elements, $p_{1/2} \exp[\, i\, \phi_{p_{1/2}}\,]$ and $p'_{3/2} \exp[\, i\, \phi_{p'_{3/2}}\,]$. The $p_{1/2}$ matrix element describes the transition between two wave functions which differ only in their principle quantum number. The M1 operator has no radial dependence; therefore, the $p_{1/2}$ matrix element is identically zero by the orthogonality of eigenfunctions with different principal quantum numbers. Included in the analysis was the $f_{5/2}$ E2 matrix element. The $p_{3/2}$ E2 matrix element was still assumed to be small enough to be ignored. The resulting E1-E2-M1 angular distribution equations are

6-6
$$a_0 = s_{1/2}^2 + 2\, d_{3/2}^2 + 2\, p_{3/2}'^2 + 3\, f_{5/2}^2$$

$$a_1 = 2\, s_{1/2}\, p'_{3/2} \cos[\, \varphi_{p'_{3/2}} - \varphi_{s_{1/2}}\,] - 2\, d_{3/2}\, p'_{3/2} \cos[\, \varphi_{p'_{3/2}} - \varphi_{d_{3/2}}\,] + 6.235\, d_{3/2}\, f_{5/2} \cos[\, \varphi_{f_{5/2}} - \varphi_{d_{3/2}}\,]$$

6-6 Continued.

$$a_2 = - d_{3/2}^2 - p_{3/2}'^2 + 1.714 f_{5/2}^2$$
$$- 2 s_{1/2} d_{3/2} \cos[\varphi_{d_{3/2}} - \varphi_{s_{1/2}}]$$
$$- 3.464 p_{3/2}' f_{5/2} \cos[\varphi_{p_{3/2}'} - \varphi_{f_{5/2}}]$$

$$a_3 = - 3.464 s_{1/2} f_{5/2} \cos[\varphi_{f_{5/2}} - \varphi_{s_{1/2}}]$$
$$- 2.771 d_{3/2} f_{5/2} \cos[\varphi_{f_{5/2}} - \varphi_{d_{3/2}}]$$

$$a_4 = - 1.714 f_{5/2}^2$$

$$b_1 = - s_{1/2} p_{3/2}' \sin[\varphi_{p_{3/2}'} - \varphi_{s_{1/2}}]$$
$$+ 4 d_{3/2} p_{3/2}' \sin[\varphi_{p_{3/2}'} - \varphi_{d_{3/2}}]$$
$$+ 3.118 d_{3/2} f_{5/2} \sin[\varphi_{f_{5/2}} - \varphi_{d_{3/2}}]$$

$$b_2 = - s_{1/2} d_{3/2} \sin[\varphi_{d_{3/2}} - \varphi_{s_{1/2}}]$$
$$+ 2.887 p_{3/2}' f_{5/2} \sin[\varphi_{p_{3/2}'} - \varphi_{f_{5/2}}]$$

$$b_3 = - 1.155 s_{1/2} f_{5/2} \sin[\varphi_{f_{5/2}} - \varphi_{s_{1/2}}]$$
$$- 0.2309 d_{3/2} f_{5/2} \sin[\varphi_{f_{5/2}} - \varphi_{d_{3/2}}]$$

$$b_4 = 0$$

The chi-square as a function of E2 and M1 cross section was calculated for the 10.2 MeV angular distribution. The value of $\sigma(f_{5/2})$ was varied from zero to ten percent of the total cross section in one percent steps. The value of $\sigma(p'_{3/2})$ was varied from zero to twenty percent of the total cross section in one percent steps. The two E1 matrix elements and the three relative phases were fit with non-linear least squares to yield the minimum chi-square. Contours of equal chi-square were calculated and may be found in Figure 6-4. Two regions of solution were seen, one with a total non-E1 cross section of about three percent and the second with a total non-E1 cross section of about eleven percent. As in the E2 case, the shallowness of the chi-square surface does not allow one to claim a true solution at either minimum. The valley running from approximately one percent M1 to over twenty percent M1 shows the degeneracy in the E1-M1 matrix elements. This E1-M1 degeneracy implies that polarized neutron capture angular distributions at a single energy cannot determine the E1-M1 cross section ratio.

Snover and others [Snov79] used the energy dependence of the angular distributions of polarized proton capture in the $^{15}N(p_{pol},\gamma_0)^{16}O$ reaction to break the E1-M1 degeneracy. They found that some angular distributions had minimum reduced chi-squares in the range of five to twenty, suggesting that an E1-E2 analysis was insufficient. They included an M1 term in their analysis. The absolute (μb) E1 and E2 amplitudes measured just above and below the suspect angular distributions were projected into the energy region by a straight line

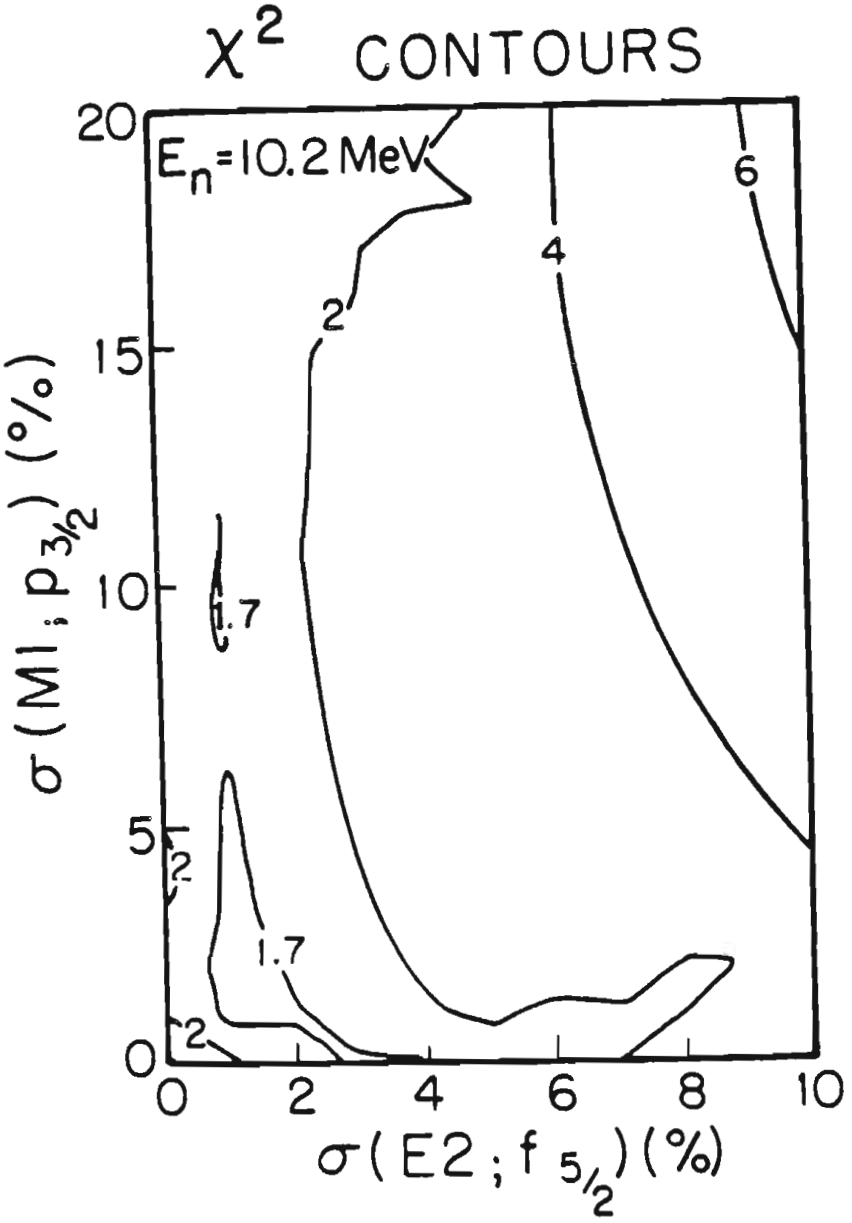

Figure 6-4 Reduced chi-square as a function of E2 and M1 cross section at 10.2 MeV. Two E1 amplitudes and three relative phases were fit via least squares to the angular distribution data using Equation 6-6, while the E2 and M1 amplitudes were held constant. The chi-square surface is discussed in the text.

[Snov80b]. The excess cross section was assumed to be M1. The M1 phase was varied to yield the minimum chi-square. The improved value of chi-square was not reported.

In a similar manner, the E2 matrix element was held constant over 9.2 and 10.2 MeV to the 11 MeV value of 0.2 % The search for the minimum chi-square included the two E1 amplitudes, the M1 amplitude and two relative phases. The search was made in the region of three percent non-E1 radiation. The results are presented in Table 6-3. The corresponding Legendre expansion coefficients may be found in Table D-1.

The M1 search did not produce fits with significantly improved chi-squares over the E2 fits. Thus the results are consistent with an interpretation of one to three percent E2, or one to two percent M1 with two tenths percent E2.

Table 6-3 E1-E2-M1 solutions for the $^{13}C(n_{pol},\gamma_0)^{14}C$ reaction. Two E1 amplitudes, the $p'_{3/2}$ M1 amplitude and two relative phases were fit via least squares to the angular distribution data using Equation 6-6. The $f_{5/2}$ E2 T-matrix element was held constant to the value measured at 11 MeV, that is, at $\sigma(f_{5/2}) = 0.2$ % and $\phi_{f_{5/2}} - \phi_{s_{1/2}} = 143^{o}$. The cross sections are defined as:

$$\sigma(s_{1/2}) = |s_{1/2}|^2$$
$$\sigma(d_{3/2}) = 2\,|d_{3/2}|^2$$
$$\sigma(f_{5/2}) = 3\,|f_{5/2}|^2$$
$$\sigma(p'_{3/2}) = 2\,|p'_{3/2}|^2.$$

E_n (MeV)	$\sigma(s_{1/2})$ (%)	$\sigma(d_{3/2})$ (%)	$\phi_d - \phi_s$ (deg)	$\sigma(p'_{3/2})$ (%)	$\phi_p - \phi_s$ (deg)	χ^2_n
9.2	8.5(40)	89.0(47)	-67(7)	2.3(12)	126(12)	1.4
10.2	14.9(50)	82.5(57)	-69(5)	2.4(12)	206(11)	1.6

7 COMPARISON TO THEORY

7-a Sum Rules. The sum rule is a model-independent conservation law which gives the total integrated absorption cross section [Hayw70]. Thus the measure of photonuclear absorptive strength is the sum rule. For electric dipole (E1) absorption, the classical dipole sum rule, based upon the kinetic energy term in the nuclear Hamiltonian is shown in Equation 7-1.

$$\int \sigma_{\gamma}(E1)\, dE_{\gamma} = 60 \frac{N\,Z}{A} \quad mb \cdot MeV \tag{7-1}$$

In the case of ^{14}C the sum rule absorptive strength is 206 mb·MeV. To calculate the fraction of the E1 absorptive strength measured in the (γ,n_0) channel, the detail balanced (γ,n_0) total cross section of Figure 3-9 was integrated using the trapezoidal rule. The total cross section was assumed to be approximately all E1. The integral's range was from E_{γ} = 13.4 to 21.2 MeV and yielded an absorptive strength of 27.3(6) mb·MeV. Thus this channel, (γ,n_0), exhausts 13.3(3) % of the classical dipole sum.

The measure of the E2 absorptive strength is the the Gell-Mann and Telegdi [Gell53] isoscalar energy weighted sum rule (IS-EWSR) which is presented in Equation 7-2.

$$7\text{-}2 \qquad \int \frac{\sigma_\gamma(E2)}{E_\gamma^2}\, dE_\gamma = \frac{\pi^2}{137}\,\frac{A}{12}\,\frac{\langle r_0^2\rangle}{938} \quad fm^2\cdot MeV^{-1}$$

Here there is a choice of values for the mean of the square of the nuclear radius, $\langle r_0^2\rangle$. C.W. deJager and others [deJa74] obtained $\langle r_0^2\rangle = 6.66$ fm^2 in ^{14}N using electron scattering. Another value for $\langle r_0^2\rangle$ may be obtained using a constant radial wave function up to the nuclear radius, $R = 1.2\ A^{1/3}$ fm^2. This results in $\langle r_0^2\rangle = 3/5\ R^2$ or for ^{14}C, $\langle r_0^2\rangle = 5.02$ fm^2. The (e,e) value differs from the constant radial wave function value by approximately 25 %, so that although the (e,e) $\langle r_0^2\rangle$ was used in the isoscalar energy weighted E2 sum rule for the following discussion, the results may be scaled up by 1.25 if the second choice of $\langle r_0^2\rangle$ is preferred. The isoscalar energy weighted E2 sum rule absorptive strength is $5.97\ 10^{-4}$ fm$^2\cdot$MeV^{-1} (5.97 μb$\cdot$MeV^{-1}).

To calculate the fraction of the isoscalar E2 absorptive strength measured in the (γ,n_0) channel, the detail balanced (γ,n_0) total cross section of Figure 3-9 was weighted by the measured E2 fraction, $f_{E2}(E_n)$ or $f'_{E2}(E_n)$, and integrated using the trapezoidal rule. The E2 fraction for the E1-E2 analysis was taken from Table 6-2 and is presented in Equation 7-3.

7-3

$$f_{E2}(E_n) = \begin{cases} 0.002(\ 2); & 5.6 \leq E_n < 8.5 \\ 0.011(\ 8); & 8.5 \leq E_n < 9.7 \\ 0.034(13); & 9.7 \leq E_n < 10.6 \\ 0.002(\ 1); & 10.6 \leq E_n < 11.5 \\ 0.010(\ 6); & 11.5 \leq E_n < 14.0 \end{cases}$$

The E2 fraction for the E1-E2-M1 analysis was taken from Table 6-2 also, except for the E2 fractions at 9.2 and 10.2 MeV, which were taken from Table 6-3. The resulting E2 fraction is presented in Equation 7-4.

7-4

$$f'_{E2}(E_n) = \begin{cases} 0.002(\ 2); & 5.6 \leq E_n < 8.5 \\ 0.002(\ 1); & 8.5 \leq E_n < 9.7 \\ 0.002(\ 1); & 9.7 \leq E_n < 10.6 \\ 0.002(\ 1); & 10.6 \leq E_n < 11.5 \\ 0.010(\ 6); & 11.5 \leq E_n < 14.0 \end{cases}$$

The isoscalar energy weighted E2 absorptive strengths are 0.74(9) and 0.30(4) $\mu b \cdot MeV^{-1}$ for the E1-E2 and the E1-E2-M1 analyses respectively. They exhaust 12 % and 5 % of the sum rule absorptive strength respectively.

7-b Comparison with Shell Model. The state of shell model calculations did not allow a detailed comparison of the observed E1 cross section with the calculated dipole absorptive strengths. A rough measure of comparison was made by calculating the weighted means, $\bar{E}_\gamma$, and standard deviations, ΔE_γ, of the observed and calculated distributions of strengths. Table E-1 presents the weighted means and standard deviations of Vergados's [Verg75] and Kissner's [Kiss73, Kiss79] calculations and the measured data. The weighted means and standard deviations were calculated according to Equations 7-5 and 7-6.

7-5
$$\bar{E}_\gamma = \frac{\int E_\gamma \, w(E_\gamma) \, dE_\gamma}{\int w(E_\gamma) \, dE_\gamma}$$

7-6
$$(\Delta E_\gamma)^2 = \frac{\int (E_\gamma - \bar{E}_\gamma)^2 \, w(E_\gamma) \, dE_\gamma}{\int w(E_\gamma) \, dE_\gamma}$$

These integrals were evaluated using three values for the weighting function, $w(E_\gamma)$; Vergados' reduced transition probabilities, Kissner's absorptive strength values, and the detail balanced (γ,n_0) total cross sections of the measured data. The range of integration for these moments corresponded with the energy range of the observed data, E_γ = 13.4 to 21.2 MeV. The predictions of both calculations are in good

agreement with the mean energy and standard deviation of the T=0 component of the dipole absorptive strength distribution.

In §7-b the ratio of the T=0 and T=1 strengths, $\Sigma(^{14}C)$ / $\Sigma(^{14}N^*)$, was found to be smaller than predicted by isospin coupling arguments. Both shell model calculations predict the strengths in each component. Vergados predicts that $\Sigma(^{14}N^*)$ should exhaust 10 % the classical dipole sum rule absorptive strength in the (γ,p_0) channel, in excellent agreement with the 11 % measured by Turner [Turn80]. However, Vergados also predicts that $\Sigma(^{14}C)$ in the (γ,n_0) channel should exhaust 20 % the classical dipole sum rule absorptive strength as compared with the 13 % observed. Kissner, on the other hand, predicts that $\Sigma(^{14}C)$ in the (γ,n_0) channel should exhaust 15 % of the absorptive strength, in good agreement with the 13 % observed. However, he also predicted that $\Sigma(^{14}N^*)$ in the (γ,p_0) channel should exhaust 6 % of the sum rule absorptive strength as compared with the 11 % Turner observed.

7-c Comparison of T=0 and T=1 Isospin Components. Turner's [Turn80] $^{13}C(p,\gamma_1)^{14}N^*$ (0^+ T=1) reaction yield, Figure 7-1, was converted into total cross section, and then via detailed balance to the (γ,p_0) total cross section. The (γ,p_0) total cross section was integrated using the trapezoidal rule assuming that approximately all the cross section was E1. Only the portion of the $^{14}N^*$ yield from E_γ = 13.4 to 21.2 MeV was used in evaluating the integral. The T=1 absorptive strength in $^{14}N^*$ was found to be 22.0(5) mb·MeV, exhausting 11 % of the classical dipole sum rule absorptive strength. The ratio

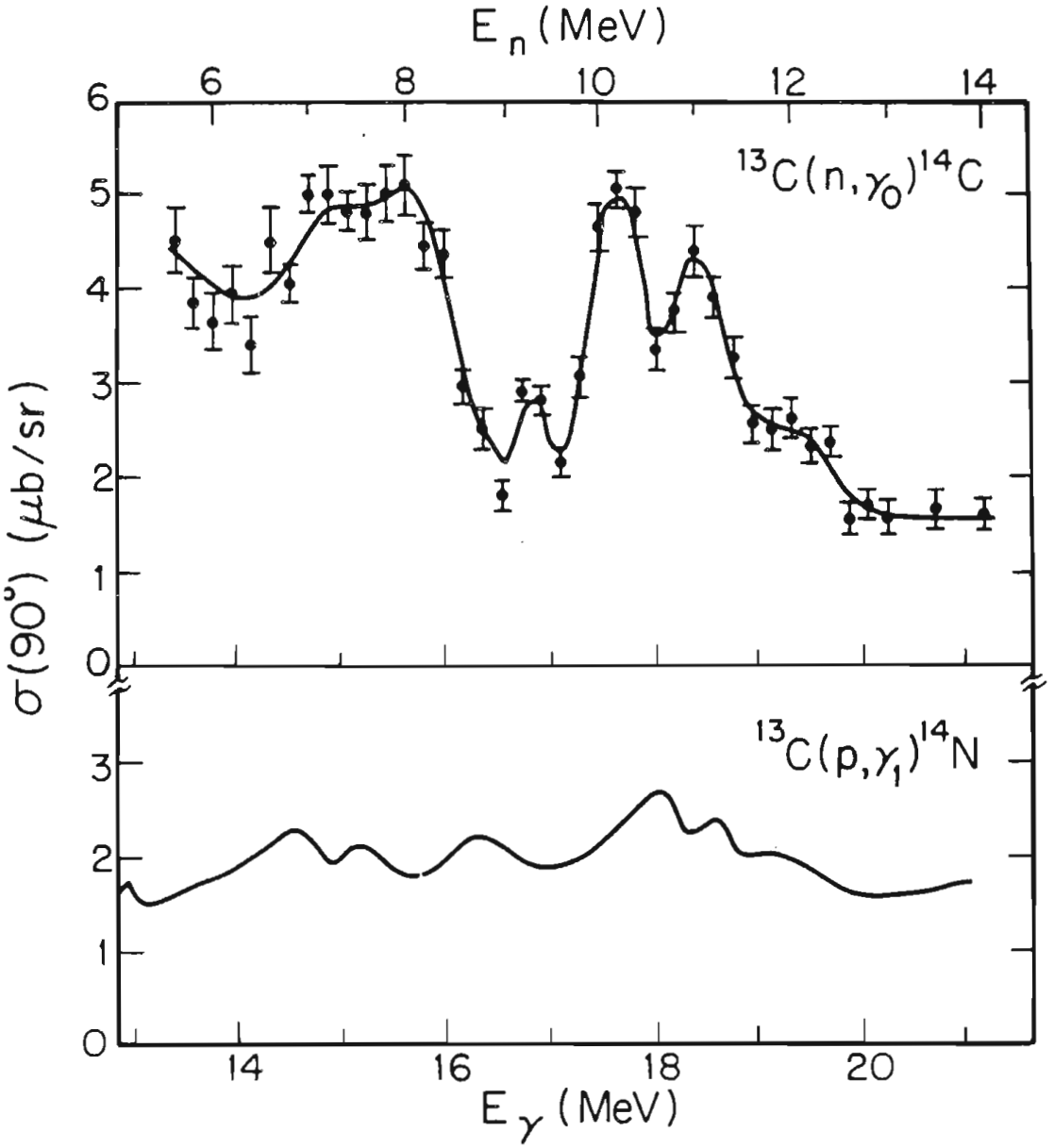

Figure 7-1 The 90° yield curve for both the $^{13}C(n,\gamma_0)^{14}C$ and $^{13}C(p,\gamma_1)^{14}N^*$ (0^+ T=1) reactions. Both yield curves are plotted as a function of γ-ray energy.

$\Sigma(^{14}C)$ / $\Sigma(^{14}N^*)$ was 1.24(4), which is half the 2.5 that the isospin arguments of §1-c would have suggested.

There were several possibilities why the observed ratio was so small. The predicted strength ratio applied to the entire energy space. The expectation was that if the integral was over a large enough region, the energy dependence should average out and leave one with the strength ratio of the entire giant dipole region. Vergados' shell model calculation agreed with the expected strength ratio; however, over the examined energy region his calculated ratio was 2. This implied that the energy region integrated was too small to be representative. Both the Kissner and Vergados shell model calculations show E1 strength above and below the energy region examined, but not enough to seriously affect the observed ratio.

Unfortunately, as seen in §7-b, the shell model calculations of Kissner and Vergados do not aid in the understanding of the failure of the isospin coupling arguments to predict the observed absorptive strength ratio of the (γ,p_0) and the (γ,n_0) channels. This disagreement leaves open the question of missing or excess absorptive strength.

7-d Direct-Semidirect Model. A direct-semidirect model code by H. Kitazawa [Kita80] was used to fit the $^{13}C(n_{pol},\gamma_0)^{14}C$ reaction data. The parameters of the calculation are shown in Table E-2. The continuum wave functions for the unbounded neutron were calculated via an optical model using the parameter set of Watson and others [Wats69]. An alternate set of parameters supplied by Richter and Parish [Rich68] was not used. This set uses an energy dependent real well potential and an

imaginary surface potential. The Watson spin orbit potential strength is held constant at 5.5 MeV. The radius and diffuseness parameters are not functions of energy. The bound state wave functions were calculated using a standard Woods-Saxon well shape. The well depth was modified until the binding energy of the neutron was correct. The radius and diffuseness parameters, and the spin orbit well depth were the same as the Watson real well potential parameters. The spectroscopic factor was taken from the tables of Cohen and Kurath [Cohe67]. E. Hayward [Hayw70] supplied the effective charge formulae.

An attempt was made to use the surface form factors of Equations 7-7 and 7-8 for the E1 and E2 semidirect capture.

7-7
$$V_c^1(r) = 1/40 \quad \varepsilon_1 \; V \; \alpha \; R_0^2 \left[- \frac{df(r)}{dr} \right] Y_{1\mu}^*(\Omega) \; \tau_z$$

7-8
$$V_c^2(r) = \frac{\hbar^2 \; V \; \varepsilon_2}{2m \; E_r} \left[- \frac{df(r)}{dr} \right] Y_{2\mu}^*(\Omega)$$

However, the measured Legendre expansion coefficients could not be fit with reasonable resonance parameters. The semidirect analysis was continued using the volume form factors of Equations 7-9 and 7-10.

$$7\text{-}9 \qquad V_c^1(r) = 1/8 \;\; \varepsilon_1 \; V \; \alpha \; r \; f(r) \; Y_{1\mu}^*(\Omega) \; \tau_z$$

$$7\text{-}10 \qquad V_c^2(r) = \frac{7 \; \hbar^2 \; V \; \varepsilon_2}{2m \; E_r \; R_0^2} \; r^2 \; f(r) \; Y_{2\mu}^*(\Omega)$$

In both cases f(r) is the Wood-Saxon potential form of $(1+\exp[(r-R_0)/a])^{-1}$. The radius and diffuseness parameters were taken to be the same as the Watson real well potential parameters. The strength of the isovector E1 form factor is the same order as is the size of the symmetry potential, V_1, in ^{14}C measured by Byrd and others [Byrd81]. Even though Byrd's symmetry potential behaved erratically as a function of energy, the isovector E1 form factor was held constant.

The Byrd measurement of the symmetry potential in ^{14}C included an imaginary term, W_1. An effort to add this imaginary term to the E1 form factor skewed the cross section yield up at low energies and down at the higher energies. Although this could be counteracted by changing other model parameters, the $\sigma(s_{1/2})$ to $\sigma(d_{3/2})$ ratio was increased so that the a_2 coefficient was too small by ~ 30 %. Thus a complex form factor was not used in the direct-semidirect fit.

Two E1 resonances were used in an ad hoc fashion to fit the measured yield curve. The strengths, positions, and widths of these two resonances were varied to produce the best fit to the observed data. Also, an isoscalar E2 resonance was added to fit the odd terms in the

polynomial expansions of the angular distributions of cross section and analyzing power. As seen in Figure 7-2, the direct-semidirect model did a good job in describing the $^{13}C(n_{pol},\gamma_0)^{14}C$ reaction data.

The direct-semidirect calculation which fit to the $^{13}C(n_{pol},\gamma_0)^{14}C$ reaction data was converted into a calculation for the $^{13}C(p_{pol},\gamma_1)^{14}N^*$ (0^+ T=1) reaction by changing the charge of the incident particle, the binding energy of the particle (E_B = 5.3 MeV), the E1 and E2 effective charges for protons (ε_1 = 0.50 and ε_2 = 0.89), and the spectroscopic factor (C^2S = 0.85). The Watson optical model parameters for ^{13}C + p were also used, see Table E-3. The shape and the magnitude of the E1 resonance were changed to fit the $^{13}C(p,\gamma_1)^{14}N^*$ (0^+ T=1) reaction yield curve. The flat behavior of the $^{13}C(p,\gamma_1)^{14}N^*$ (0^+ T=1) reaction yield curve leads to the unreasonable value for the E1 absorptive strength of 270 %. The semidirect formulation assumes the resonance has a Lorentzian shape, Equation 1-7, which is not necessarily the correct shape for light nuclei, §1-a. The proper interpretation of this absorptive strength parameter is that it is just an ad hoc fitting parameter. The E2 resonance parameters were unchanged.

The observed polynomial expansion coefficients, Figure 7-2, were fit fairly well considering no effort was made to change the model parameters specifically for the $^{13}C(p_{pol},\gamma_1)^{14}N^*$ (0^+ T=1) reaction case. The fit to the E2 cross section strongly suggests that the collective E2 absorptive strength seen in the $^{13}C(n_{pol},\gamma_0)^{14}C$ reaction

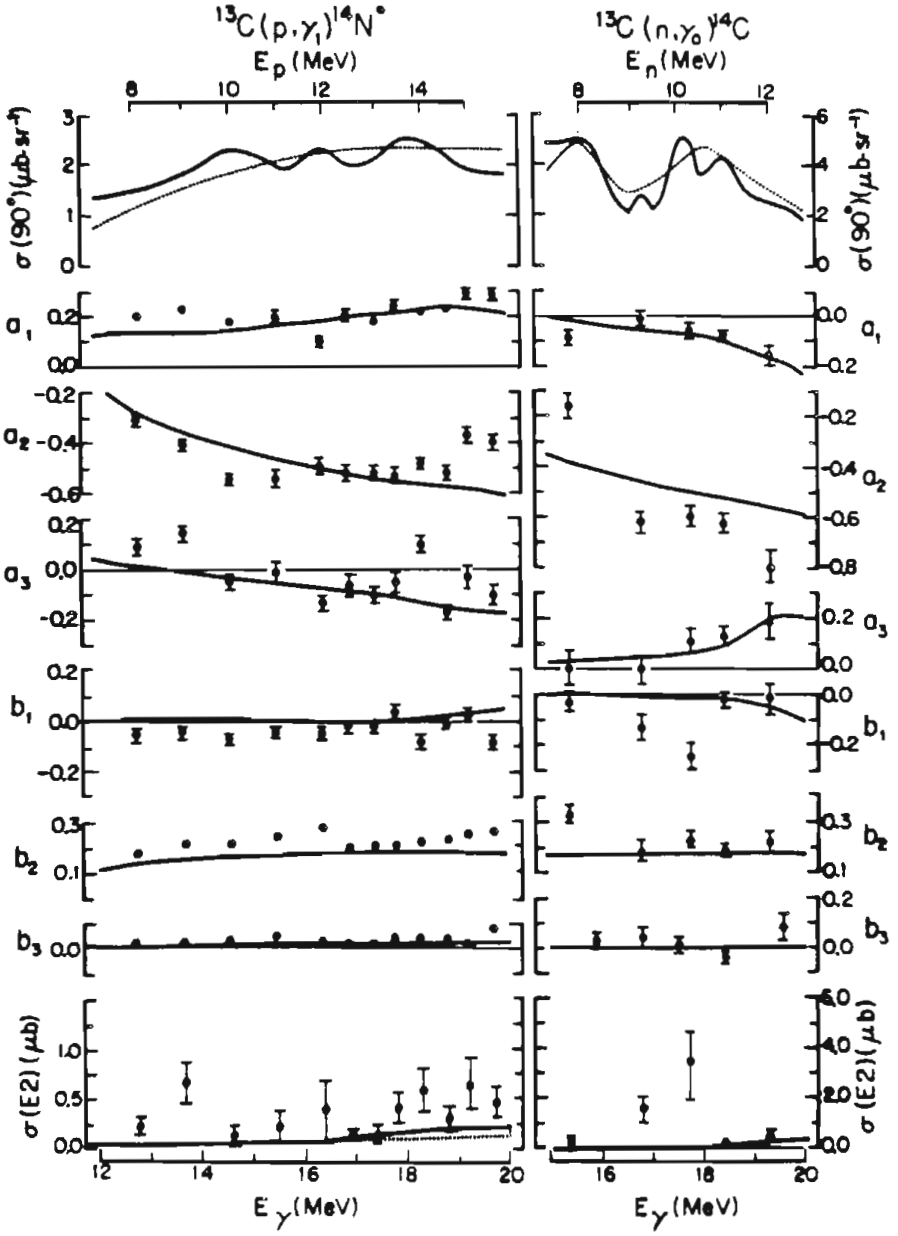

Figure 7-2 The 90° yields, Legendre expansion coefficients, and E2 cross sections for the $^{13}C(n_{pol},\gamma_0)^{14}C$ and the $^{13}C(p_{pol},\gamma_1)^{14}N^*$ (0^+ T=1) reactions. The solid lines are the direct-semidirect calculations described in the text. The dotted lines in the E2 cross section frame are direct capture calculations.

is consistent with the E2 absorptive strength observed in the $^{13}C(p_{pol},\gamma_1)^{14}N^*$ (0^+ T=1) reaction that was in excess of that predicted by direct capture alone. This is good indirect evidence that the isoscalar E2 resonance is actually being observed, but it is premature to claim this since there are only measurements on the low energy side of the suspected isoscalar E2 resonance.

In summary, the direct-semidirect model produces a reasonable description of the E1 and E2 absorptive strength seen in both the $^{13}C(n_{pol},\gamma_0)^{14}C$ and the $^{13}C(p_{pol},\gamma_1)^{14}N^*$ (0^+ T=1) reactions. Both 90^o excitation functions should be extended to E_γ energies of 25 MeV. Angular distributions of cross section and analyzing power should also be measured at these higher energies to obtain the E2 absorptive strength over the suspected resonance. The $^{13}C(n,\gamma_0)^{14}C$ reaction cross section drops by a factor of two between E_n = 12 and 14 MeV. If this trend continues, measuring these higher energy angular distributions will take significantly more resources. However, these measurements must be made to confirm the presence of the isoscalar E2 resonance.

8 REFERENCES

Abra64 M. Abramowitz and T.A. Stegun, Editors
Applied Mathematics Series - 55 ("AMS-55")
Handbook of Mathematical Functions with Formulas, Graphs and Mathematical Tables.
U.S. Department of Commerce
National Bureau of Standards, 1964.

Auch79 G.F. Auchampauch, S. Plattard and N.W. Hill
Neutron Total Cross-Section Measurements of ^{9}Be, $^{10,11}B$, and $^{12,13}C$ from 1.0 to 14 MeV Using the $^{9}Be(d,n)^{10}B$ Reaction as a "White" Neutron Source
Nucl. Sci. Engr. 69 (1979) 30

Bald61 A.M. Baldin, V.I. Goldanskii and I.L. Rosenthal
Kinematics of Nuclear Reactions
Oxford Press, London, 1961

Bars70 H.H. Barschall and W. Haeberli, Editors
Polarization Phenomena in Nuclear Reactions
Wisconsin Press, Madison, 1970

Bell77 Bell Laboratories
Documents for Use with GR-Z
Murray Hill, NJ 07974
August, 1977

Bert80 Fred E. Bertrand, Editor

Giant Multipole Resonances

Harwood Academic, New York, 1980

Bevi69 Philip R. Bevington

Data Reduction and Error Analysis for the Physical Sciences.

McGraw-Hill, New York, 1969.

Beye81 A.G. Beyerle

Double Differential Continuum Neutron Scattering Cross Sections in Iron and Nickel for Incident Neutron Energies of 7.5, 10 and 12 MeV

Ph.D. Dissertation, N.C. State University, 1981

Brow64 G.E. Brown

Direct and Semi-Direct (p,γ) and (n,γ) Reactions

Nucl. Phys. 57 (1964) 339

Byrd81 R.C. Byrd, C.E. Floyd, K. Murphy, P.P. Guss, R.L. Walter and S.R. Cotanch

Measurement and Lane-Model Analysis of Cross Sections for the $^{13}C(n,p)^{13}N$ and $^{15}N(p,n)^{15}O$ Reactions

Nucl. Phys. A351 (1981) 189

Came77 C.P. Cameron

The Giant Dipole Resonance Region of ^{31}P: Polarized and Unpolarized Proton Capture Measurements

Ph.D. Dissertation, Duke University, 1977

Cleg70 T.B. Clegg, G.A. Bissenger, W. Haeberli and P.A. Ouin

Lamb-Shift Polarized Ion Sources for Tandem Accelerators at Wisconsin and Triangle Universities Nuclear Laboratory

in [Bars70]

Clem65a C.F. Clemet, A.M. Lane and J.A. Rook

Radiative Capture by Excitation of Collective Vibrations: (I) Theory

Nucl. Phys. 66 (1965) 273

Clem65b C.F. Clemet, A.M. Lane and J.A. Rook

Radiative Capture by Excitation of Collective Vibrations: (II) Calculation

Nucl. Phys. 66 (1965) 273

Cohe76 S. Cohen and D. Kurath

Spectroscopic Factors for the 1p Shell

Nucl. Phys. A101 (1967) 1

Cota78 S.R. Cotanch

Private Communication, 1978

deBo78 C. de Boor

A Practical Guide to Splines

Springer-Verlag, New York, 1978

deJa74 C.W. de Jager, L.H. de Vries, and L.C. de Vries

Nuclear Charge- and Magnetization-Density-Distributions Parameters from Elastic Electron Scattering

At. Data and Nucl. Data Tab. 14 (1974) 479

Dros78 M. Drosg

Unified Absolute Differential Cross Section for Neutron Production by the Hydrogen Isotopes for Charged-Particle Energies Between 6 and 17 MeV

Nucl. Sci. Engr. 67 (1978) 190

Endt62 P.M. Endt, M. Demer and P.B. Smith, Editors

Nuclear Reactions

Wiley-Interscience, New York, 1962

Fal170 S. Fallieros and B. Goulard

Isovector Excitations in Nuclei

Nucl. Phys. A147 (1970) 593

Ful162 E.G. Fuller and E. Hayward

The Giant Resonance of the Nuclear Photoeffect

in [Endt62]

Gell53 M. Gell-Mann and V.L. Telgdi
Consequences of Charge Independence for Nuclear Reactions Involving Photons
Phys. Rev. 91 (1953) 169

Glav74 H.F. Glavish
Private Communication, 1974

Hann80 S.S. Hanna
Overview of Giant Resonances with Emphasis on Recent E1 Results in [Bert80]

Hayw70 E. Hayward
Photonuclear Reactions
U.S. Natl. Bur. Stand. Monograph No. 118
Washington, DC, 1970

Hogu79 H.H. Hogue and S. El-Kadi
Private Communication, 1979

Jens79 M.J. Jensen, D.R. Tilley, H.R. Weller, N.R. Roberson, S.A. Wender and T.B. Clegg
Polarized-Neutron Capture in the Giant-Resonance Region of ^{41}Ca
Phys. Rev. Lett. 43 (1979) 609

Kiss73 H.R. Kissner, R.A. Eramzhyan and H.U. Jager
On the Decay of the Photoresonance in ^{14}N and ^{14}C Nuclei
Nucl. Phys. A207 (1973) 78

Kiss79 H.R. Kissner and R.A. Eramzhyan

Collective Resonances with Isospin T = 2, 1 and 0 in Photoreactions, Low − q Electron Scattering and Radiative Pion Capture on A = 14 Nuclei.

Nucl. Phys. A326 (1979) 289

Kita80 H. Kitazawa

Private Communication, 1980

Lika76 A. Likar, M. Potokar and F. Cvelbar

Angular Distribution of γ Rays from the Radiative Capture of Fast Neutrons

Nucl. Phys. A280 (1977) 49

Liso73 P.W. Lisowski

The Transfer Polarization of the $D(d,n)^3He$ Reaction and the Scattering of Polarized Neutrons from ^4He and ^3He

Ph.D. Dissertation, Duke University, 1973

Liso75 P.W. Lisowski, R.L. Walter, C.E. Busch and T.B. Clegg

Polarization Transfer in the $^2H(d_{pol},n_{pol})^3He$ Reaction at $\theta = 0^o$

Nucl. Phys. A242 (1975) 298

Lush65 A.A. Lushnikov and D.E. Zaretksy

Giant Resonance in Heavy Nuclei

Nucl. Phys. 66 (1965) 35

McBr77 Robert Chism McBroom
Proton Radiative Capture by Tritium Below 30 MeV.
Ph.D. Dissertation, University of Florida, 1977.

Poto77 M. Potokar, A. Likar, M. Budnar and F. Cvelbar
Analysis of Fast Neutron Capture Data Based on the Refined Direct-Semidirect Model
Nucl. Phys. A277 (1977) 29

Pres75 M.A. Preston and R.K. Bhadur
The Structure of the Nucleus
Addison-Wesley, Reading, 1975

Rich68 A. Richter and L.J. Parish
Compound-Nucleus Effects in (p,n) Charge-Exchange Reactions in Light Nuclei
Phys. Rev. Lett. 21 (1968) 1824

Robe78 N.R. Roberson
Private Communication, 1978

Seyl79 R.G. Seyler and H.R. Weller
Angular Distribution Theory for Particle-Capture-Gamma Reactions
Phys. Rev. C 20 2 (1979) 453

Snov79 K.A. Snover, P.G. Ikossi and T.A. Trainor
Observation of Magnetic Dipole Strength in ^{16}O
Phys. Rev. Lett. 43 2 (1979) 117

Snov80a K.A. Snover, P.G. Ikossi, E.G. Adelberger and K.T. Lesko
Unique determination of the Amplitude and Phase for the Population of the Giant Dipole Resonance in the reaction $^{12}C(p_{pol},\gamma_0)^{14}N$
Phys. Rev. Lett. 44 (1980) 927

Snov80b K.A. Snover
Private Communication, 1980

Stor70 E. Storm and H.I. Israel
Photon Cross Sections from 1 keV to 100 MeV for elements Z = 1 to Z = 100.
Nucl. Data Tab. 7 6 (1970) 565

Suff68 M. Suffert, W. Feldman, J. Mahieux and S.S. Hanna
One-Crystal NaI Spectrometer
Nucl. Inst. Meth. 63 (1968) 1

Trai74 T.A. Trainor, T.B. Clegg and P.W. Lisowski
The Tensor Analyzing Power A_{zz} at $\theta = 0^{o}$ for the $^{3}He(d_{pol},p)^{4}He$ Reaction
Nucl. Phys. A220 (1974) 533

TUNL80 Triangle Universities Nuclear Laboratory
Annual Report
TUNL XIX (1980) 100

Turn78 J.D. Turner
The Giant Dipole Resonance Region of ^{14}N: Polarized and Unpolarized Proton Capture Measurements
Ph.D. Dissertation, Duke University, 1978

Turn80 J.D. Turner, N.R. Roberson, S.A. Wender, H.R. Weller and D.R. Tilley
Polarized Proton Capture on ^{13}C
Phys. Rev. C 21 2 (1980) 525

Uber71 H. Uberall
Electron Scattering from Complex Nuclei
Academic Press, New York, 1971

Verg75 J.D. Vergados
The $T = T_z + 2$ GDR and the Dipole States of the $A = 6$ and 14 Nuclei.
Nucl. Phys. A239 (1975) 271

Warb69 E.K. Warburton and J. Wenesner
The Role of Isospin in Electromagnetic Transitions
in [Wilk69]

Wats69 B.A. Watson, P.P. Singh and R.E. Segel
Optical-Model Analysis of Nucleon Scattering from 1p-Shell Nuclei between 10 and 50 MeV
Phys. Rev. 182 4 (1969) 977

Well78 H.R. Weller, R.A. Blue, P.L. von Behren, N.R. Roberson C.R. Gould D.R. Tilley and S.A. Wender
Angular Distributions Measurements for Radiative Capture of Fast Neutrons by ^{40}Ca
Phys. Rev. C 17 (1978) 1260

Well80 H.R. Weller and N.R. Roberson
Capture Reactions with Protons, Neutrons, and Alpha Particles
Rev. Mod. Phys. 52 4 (1980) 699

Wend78 S.A. Wender, N.R. Roberson, M. Potokar, H.R. Weller and D.R. Tilley
Quadrupole Radiation in Fast-Neutron Capture on ^{40}Ca
Phys. Rev. Lett. 41 (1978) 1217

Wend80 S.A. Wender, C.E. Floyd, T.B. Clegg and W.R. Wylie
A High Efficiency Bunching System for Polarized Beams
Nucl. Inst. Meth. 174 (1980) 341

Wend81 S.A. Wender

A High Efficiency Bunching System for the TUNL Polarized Ion Source

IEEE Tran. Nucl. Sci. NS-28 (1981) 1465

Wilk69 D.H. Wilkinson, Editor

Isospin in Nuclear Physics

North Holland, Amsterdam, 1969

APPENDIX A EXPERIMENTAL EQUIPMENT AND METHODOLOGY

Table A-1 NaI energy spectra line-shape fitting functions. The following is the functional form of the line-shape fitting function used with the TUNL 254 by 254 mm NaI detection system. The two line-shape parameter sets used were designed by R.C. McBroom [McBr77] and J.D. Turner [Turn78].

$$S_i = \begin{cases} \exp[\, c_1+c_2 i+c_3 i^2+c_4 i^3 \,]: & i \leq 294 \\ \exp[\, c_5+c_6 i+c_7 i^2+c_8 i^3 \,]: & i \geq 294 \end{cases}$$

Coefficient	Low-Rejection	High-Rejection
c_1	-3.6393	$-2.1858\ 10^{+1}$
c_2	$8.9809\ 10^{-2}$	$1.9262\ 10^{-1}$
c_3	$-4.8943\ 10^{-4}$	$-6.2133\ 10^{-4}$
c_4	$9.1427\ 10^{-7}$	$8.8137\ 10^{-7}$
c_5	$1.4269\ 10^{+3}$	$1.4269\ 10^{+3}$
c_6	$-1.4676\ 10^{+1}$	$-1.4675\ 10^{+1}$
c_7	$5.0242\ 10^{-2}$	$5.0238\ 10^{-2}$
c_8	$-5.7104\ 10^{-5}$	$-5.7108\ 10^{-5}$

APPENDIX B EXCITATION FUNCTION

Table B-1 The raw data for the excitation function of the $^{13}C(n,\gamma_0)^{14}C$ reaction.

E_n (MeV)	Q_b (mC)	Gas Cell Pressure (psig)	Accidental Coin. Rate (%)	Σ_{n,γ_0} (counts)	Σ_{bkgr} (counts)	Rejection Mode
5.6	3.00	14.1	4.5	173	2	High
5.8	4.80	14.2	3.9	248	6	High
6.0	3.00	14.2	4.8	148	3	High
6.2	3.00	14.2	5.1	162	2	High
6.4	3.00	14.3	4.9	144	2	High
6.6	3.00	14.3	5.0	195	3	High
6.8	3.00	14.1	5.9	188	2	High
6.8	3.00	14.3	5.1	171	3	High
7.0	3.00	14.3	5.7	224	2	High
7.0	3.00	14.3	1.4	317	3	Low
7.2	3.00	14.3	1.2	324	3	Low
7.4	3.00	14.1	6.2	232	3	High
7.4	3.00	14.1	1.4	318	2	Low
7.4	3.00	14.3	1.1	310	2	Low
7.6	3.00	14.4	1.3	321	2	Low
7.8	3.00	14.4	1.4	343	2	Low

Table B-1 Continued.

E_n (MeV)	Q_b (mC)	Gas Cell Pressure (psig)	Accidental Coin. Rate (%)	Σ_{n,γ_0} (counts)	Σ_{bkgr} (counts)	Rejection Mode
8.0	3.00	14.4	1.5	353	2	Low
8.2	3.00	14.4	1.6	312	1	Low
8.4	3.00	14.4	1.6	310	2	Low
8.6	3.00	14.5	1.5	214	1	Low
8.8	3.00	14.5	1.6	186	1	Low
9.0	3.00	14.5	1.6	135	2	Low
9.2	3.00	14.4	1.8	244	2	Low
9.2	3.00	15.0	0.7	211	3	Low
9.2	3.00	14.6	1.5	212	3	Low
9.4	3.00	14.6	4.9	232	16	Low
9.4	3.00	14.9	0.8	213	3	Low
9.6	3.00	14.9	0.9	173	3	Low
9.8	3.00	14.9	1.0	243	2	Low
10.0	3.00	14.8	1.1	373	3	Low
10.2	3.00	14.8	1.1	440	2	Low
10.2	3.00	14.5	2.3	365	3	Low

Table B-1 Continued.

E_n (MeV)	Q_b (mC)	Gas Cell Pressure (psig)	Accidental Coin. Rate (%)	Σ_{n,γ_0} (counts)	Σ_{bkgr} (counts)	Rejection Mode
10.4	3.00	14.8	1.5	388	2	Low
10.6	3.00	14.8	1.9	275	4	Low
10.8	3.00	14.8	2.0	304	1	Low
11.0	3.00	14.8	2.2	358	3	Low
11.2	3.00	14.8	2.4	319	3	Low
11.4	3.00	14.7	2.6	267	2	Low
11.6	3.00	14.7	2.8	208	3	Low
11.8	3.00	14.7	3.0	206	3	Low
12.0	3.00	14.7	3.1	215	4	Low
12.2	3.00	14.7	3.5	189	2	Low
12.4	3.00	14.6	4.8	190	2	Low
12.6	2.86	14.6	4.0	121	2	Low
12.8	3.00	14.6	3.2	139	2	Low
13.0	3.00	14.6	3.6	129	3	Low
13.5	2.40	14.6	5.5	128	27	Low
14.0	3.00	14.6	6.4	130	4	Low

Table B-2 The 90^{o} cross section of the $^{13}C(n,\gamma_0)^{14}C$ reaction. The uncertainties represent one standard deviation of the statistical error.

E_n (MeV)	$\sigma(90^{o})$ ($\mu b \cdot sr^{-1}$)	E_n (MeV)	$\sigma(90^{o})$ ($\mu b \cdot sr^{-1}$)	E_n (MeV)	$\sigma(90^{o})$ ($\mu b \cdot sr^{-1}$)
5.6	4.59(35)	8.4	4.33(25)	11.2	3.90(22)
5.8	3.92(26)	8.6	2.94(20)	11.4	3.27(20)
6.0	3.69(31)	8.8	2.52(19)	11.6	2.53(18)
6.2	3.98(32)	9.0	1.79(16)	11.8	2.50(18)
6.4	3.42(29)	9.2	2.90(11)	12.0	2.60(18)
6.6	4.49(33)	9.4	2.81(14)	12.2	2.31(17)
6.8	4.05(22)	9.6	2.17(17)	12.4	2.36(17)
7.0	4.98(22)	9.8	3.05(20)	12.6	1.56(15)
7.2	5.00(28)	10.0	4.65(24)	12.8	1.70(15)
7.4	4.82(17)	10.2	5.05(18)	13.0	1.57(14)
7.6	4.77(27)	10.4	4.80(25)	13.5	1.61(20)
7.8	5.02(27)	10.6	3.37(21)	14.0	1.63(15)
8.0	5.09(27)	10.8	3.75(22)		
8.2	4.44(25)	11.0	4.39(23)		

Table B-3 The total cross section of the $^{13}C(n,\gamma_0)^{14}C$ reaction. The uncertainties represent one standard deviation of the statistical error.

E_n (MeV)	σ_{n,γ_0} (μb)	E_n (MeV)	σ_{n,γ_0} (μb)	E_n (MeV)	σ_{n,γ_0} (μb)
5.6	50.3(38)	8.4	43.5(25)	11.2	37.3(21)
5.8	42.7(28)	8.6	29.4(20)	11.4	31.3(19)
6.0	39.9(34)	8.8	25.1(19)	11.6	24.1(17)
6.2	42.7(34)	9.0	17.8(16)	11.8	23.8(17)
6.4	36.4(31)	9.2	28.6(11)	12.0	24.7(17)
6.6	47.5(35)	9.4	27.7(14)	12.2	21.9(16)
6.8	42.6(23)	9.6	21.3(17)	12.4	22.4(16)
7.0	52.0(23)	9.8	29.8(20)	12.6	14.8(14)
7.2	51.9(29)	10.0	45.3(23)	12.8	16.1(14)
7.4	49.8(18)	10.2	49.0(18)	13.0	14.8(13)
7.6	49.0(28)	10.4	46.5(24)	13.5	15.2(19)
7.8	51.3(28)	10.6	32.5(20)	14.0	15.4(14)
8.0	51.7(27)	10.8	36.1(21)		
8.2	44.9(25)	11.0	42.1(22)		

Table B-4 The total cross section of the $^{14}C(\gamma,n_0)^{13}C$ reaction from detail balance. The uncertainties represent one standard deviation of the statistical error.

E_γ (MeV)	σ_{γ,n_0} (mb)	E_γ (MeV)	σ_{γ,n_0} (mb)	E_γ (MeV)	σ_{γ,n_0} (mb)
13.4	5.10(39)	16.0	4.64(27)	18.6	3.93(22)
13.6	4.36(29)	16.2	3.14(21)	18.8	3.28(20)
13.7	4.10(34)	16.3	2.68(20)	18.9	2.53(18)
13.9	4.42(35)	16.5	1.89(17)	19.1	2.48(18)
14.1	3.79(32)	16.7	3.05(12)	19.3	2.57(18)
14.3	4.96(36)	16.9	2.95(15)	19.5	2.28(17)
14.5	4.47(24)	17.1	2.27(18)	19.7	2.32(17)
14.7	5.48(24)	17.3	3.17(21)	19.9	1.52(15)
14.9	5.48(31)	17.5	4.81(25)	20.0	1.66(15)
15.0	5.27(19)	17.6	5.20(19)	20.2	1.52(14)
15.2	5.19(29)	17.8	4.92(26)	20.7	1.55(19)
15.4	5.44(29)	18.0	3.44(21)	21.2	1.55(14)
15.6	5.50(29)	18.2	3.81(22)		
15.8	4.78(27)	18.4	4.44(23)		

APPENDIX C ANGULAR DISTRIBUTIONS

Table C-1 Deuterium gas cell pressures used in measuring angular distributions of cross sections and analyzing powers with the resulting neutron energy spread. E_n was the neutron energy for 0^o neutrons produced at the center of the gas cell. ΔE_n was the difference in energy between the 0^o neutrons produced at the front and back of the gas cell. These values were calculated by the code Kadel, §2-b.

E_n (MeV)	Pressure (psig)	ΔE_n (MeV)
7.75	60.0	0.40
9.2	75.0	0.37
10.2	75.0	0.33
11.	75.0	0.30
12.	75.0	0.27

Table C-2 Observed cross section and analyzing power angular distributions for the $^{13}C(n_{pol},\gamma_0)^{14}C$ reaction at neutron energies of 7.75, 9.2, 10.2, 11 and 12 MeV. The uncertainties represent one standard deviation of the statistical error.

E_n	θ	$\sigma(\theta)/A_0$	$A_y(\theta)$	$A_y(\theta)\sigma(\theta)/A_0$
7.75	35	0.87(6)		
	45	0.91(5)	0.54(9)	0.49(8)
	55	0.92(4)	0.50(8)	0.47(8)
	70		0.22(8)	0.22(8)
	90	1.08(5)	0.06(10)	0.06(11)
	110	1.15(6)	-0.34(9)	-0.37(10)
	125	1.00(6)	-0.45(9)	-0.48(10)
	141	1.00(4)	-0.43(7)	-0.43(7)
	150	0.96(6)		
9.2	35	0.69(8)		
	40	0.69(8)		
	45	0.80(4)		

Table C-2 Continued.

E_n	θ	$\sigma(\theta)/A_0$	$A_y(\theta)$	$A_y(\theta)\sigma(\theta)/A_0$
9.2	Continued.			
	55	1.06(4)	0.29(10)	0.29(10)
	70	1.23(5)	-0.03(10)	-0.03(12)
	90	1.25(3)	-0.12(7)	-0.16(9)
	110	1.25(5)	-0.21(9)	-0.25(11)
	125	1.06(4)	-0.39(10)	-0.43(11)
	140	0.72(5)	-0.31(14)	-0.24(11)
	150	0.64(6)		
10.2	30	0.55(6)		
	35	0.77(6)		
	45	0.73(6)	0.18(11)	0.14(9)
	60	0.99(5)	0.15(9)	0.15(9)
	70	1.18(6)	0.01(10)	0.01(11)
	90	1.27(5)	-0.17(9)	-0.22(12)
	110	1.29(4)	-0.46(7)	-0.58(9)
	125	1.02(4)	-0.32(11)	-0.35(12)
	135	0.91(4)		
	141	0.82(5)	-0.67(11)	-0.53(9)
	145	0.87(7)		
	150	0.54(5)		

Table C-2 Continued.

E_n	θ	$\sigma(\theta)/A_0$	$A_y(\theta)$	$A_y(\theta)\sigma(\theta)/A_0$
11.	35	0.64(3)		
	45	0.77(3)	0.29(7)	0.22(5)
	55	0.89(4)	0.23(8)	0.21(7)
	70	1.12(3)	0.22(5)	0.25(6)
	90	1.33(3)	0.11(5)	0.15(7)
	110	1.28(3)	-0.25(5)	-0.32(7)
	125	1.09(5)	-0.21(7)	-0.23(8)
	141	0.79(4)	-0.40(9)	-0.32(7)
	150	0.65(4)		
12.	35	0.46(7)		
	45	0.68(7)		
	55	0.83(4)	0.46(13)	0.39(11)
	70	1.21(4)	0.30(12)	0.34(13)
	90	1.35(4)	-0.13(9)	-0.19(13)
	110	1.41(4)	-0.23(10)	-0.32(13)
	125	1.26(5)	-0.26(12)	-0.31(14)
	140	0.78(3)	-0.31(14)	-0.25(11)
	150	0.58(8)		

Table C-3 Observed and finite-geometry corrected cross section and analyzing power angular distribution Legendre expansion coefficients for the $^{13}C(n_{pol},\gamma_0)^{14}C$ reaction, with $n_{max} = k_{max} = 2$. The uncertainties represent one standard deviation of the statistical error. The finite-geometry corrections are discussed in §5-b.

E_n (MeV)		Legendre Coefficients		
		Observed	Corrected	χ^2_n
7.75	a_1	-0.09(3)	-0.09(3)	0.5
	a_2	-0.16(5)	-0.16(5)	
	b_1	0.00(4)	-0.03(4)	0.4
	b_2	0.32(3)	0.33(3)	
9.2	a_1	-0.02(3)	-0.01(3)	1.6
	a_2	-0.64(4)	-0.62(4)	
	b_1	-0.11(5)	-0.13(5)	0.8
	b_2	0.20(4)	0.18(4)	

Table C-3 Continued.

E_n (MeV)		Legendre Coefficients Observed	Corrected	χ^2_n
10.2	a_1	-0.07(2)	-0.07(2)	2.4
	a_2	-0.62(4)	-0.61(4)	
	b_1	-0.24(4)	-0.24(5)	1.1
	b_2	0.24(3)	0.23(3)	
11.	a_1	-0.01(2)	-0.09(2)	1.6
	a_2	-0.65(3)	-0.63(3)	
	b_1	0.01(3)	-0.02(3)	2.4
	b_2	0.20(2)	0.19(2)	
12.	a_1	-0.24(3)	-0.22(3)	3.8
	a_2	-0.88(5)	-0.84(5)	
	b_1	0.01(6)	-0.02(6)	1.2
	b_2	0.25(4)	0.22(4)	

Table C-4 Observed and finite-geometry corrected cross section and analyzing power angular distribution Legendre expansion coefficients for the $^{13}C(n_{pol},\gamma_0)^{14}C$ reaction, with $n_{max} = k_{max} = 3$. The uncertainties represent one standard deviation of the statistical error. The finite-geometry corrections are discussed in §5-b.

E_n (MeV)		Legendre Coefficients		
		Observed	Corrected	χ^2_n
7.75	a_1	-0.08(3)	-0.08(3)	0.6
	a_2	-0.15(6)	-0.15(6)	
	a_3	0.05(8)	0.05(8)	
	b_1	-0.01(4)	-0.05(4)	0.1
	b_2	0.32(3)	0.33(3)	
	b_3	0.02(3)	0.03(3)	
9.2	a_1	-0.02(3)	0.00(3)	1.9
	a_2	-0.64(5)	-0.61(5)	
	a_3	0.01(6)	0.01(6)	
	b_1	-0.10(5)	-0.12(5)	0.7
	b_2	0.21(4)	0.20(4)	
	b_3	0.05(4)	0.04(4)	

Table C-4 Continued.

E_n (MeV)		Legendre Coefficients Observed	Corrected	χ^2_n
10.2	a_1	-0.06(2)	-0.06(3)	2.2
	a_2	-0.61(4)	-0.60(4)	
	a_3	0.13(6)	0.11(5)	
	b_1	-0.25(5)	-0.24(5)	1.3
	b_2	0.25(3)	0.24(3)	
	b_3	0.00(3)	0.01(3)	
11.	a_1	-0.09(2)	-0.08(2)	0.2
	a_2	-0.64(3)	-0.63(3)	
	a_3	0.14(4)	0.13(4)	
	b_1	0.00(3)	-0.01(3)	2.2
	b_2	0.20(2)	0.19(2)	
	b_3	-0.03(2)	-0.04(2)	
12.	a_1	-0.16(4)	-0.16(4)	3.0
	a_2	-0.82(5)	-0.80(6)	
	a_3	0.22(6)	0.19(7)	
	b_1	0.01(6)	-0.02(6)	0.5
	b_2	0.28(5)	0.25(5)	
	b_3	0.08(5)	0.08(5)	

Table C-5 Observed and finite-geometry corrected cross section and analyzing power angular distribution Legendre expansion coefficients for the $^{13}C(n_{pol},\gamma_0)^{14}C$ reaction, with $n_{max} = k_{max} = 4$. The uncertainties represent one standard deviation of the statistical error. The finite-geometry corrections are discussed in §5-b.

E_n (MeV)		Legendre Coefficients		
		Observed	Corrected	χ^2_n
7.75	a_1	-0.07(3)	-0.07(3)	0.5
	a_2	-0.12(7)	-0.11(7)	
	a_3	0.05(8)	0.05(8)	
	a_4	0.08(9)	0.08(9)	
	b_1	-0.01(4)	-0.05(4)	0.1
	b_2	0.32(6)	0.32(3)	
	b_3	-0.05(3)	0.04(3)	
	b_4	0.00(3)	0.01(3)	

Table C-5 Continued.

E_n (MeV)	Legendre Coefficients	Observed	Corrected	χ^2_n
9.2	a_1	-0.04(3)	-0.03(3)	1.5
	a_2	-0.73(7)	-0.71(7)	
	a_3	-0.03(7)	-0.03(7)	
	a_4	-0.15(8)	-0.15(8)	
	b_1	-0.09(5)	-0.11(6)	0.9
	b_2	0.23(5)	0.22(6)	
	b_3	0.07(5)	0.06(5)	
	b_4	0.03(5)	0.03(5)	
10.2	a_1	-0.06(2)	-0.06(3)	2.5
	a_2	-0.62(5)	-0.61(5)	
	a_3	0.12(6)	0.11(5)	
	a_4	0.01(8)	-0.01(7)	
	b_1	-0.25(5)	-0.24(5)	1.6
	b_2	0.25(3)	0.23(3)	
	b_3	0.00(3)	0.00(3)	
	b_4	-0.02(3)	-0.02(3)	

Table C-5 Continued.

E_n (MeV)	Legendre Coefficients	Observed	Corrected	χ_n^2
11.	a_1	-0.08(2)	-0.08(2)	0.1
	a_2	-0.62(4)	-0.61(4)	
	a_3	0.14(4)	0.13(4)	
	a_4	0.05(6)	0.04(6)	
	b_1	0.00(3)	-0.02(3)	2.2
	b_2	0.19(2)	0.18(2)	
	b_3	-0.05(2)	-0.04(2)	
	b_4	-0.03(2)	-0.03(2)	
12.	a_1	-0.19(4)	-0.18(4)	2.8
	a_2	-0.94(8)	-0.91(8)	
	a_3	0.21(7)	0.17(7)	
	a_4	-0.18(9)	-0.18(9)	
	b_1	-0.01(6)	-0.04(6)	0.5
	b_2	0.26(6)	0.23(6)	
	b_3	0.06(6)	0.05(6)	
	b_4	-0.04(6)	-0.04(6)	

APPENDIX D TRANSITION MATRIX ELEMENT ANALYSIS

Table D-1 Cross section and analyzing power angular distribution Legendre expansion coefficients for the $^{13}C(n_{pol},\gamma_0)^{14}C$ reaction, corresponding to the matrix element solutions found in Tables 6-2 and 6-3. The uncertainties are taken from Table C-5.

E_n (MeV)		---Legendre Coefficients--- E1-E2	E1-E2-M1
7.75	a_1	-0.07(3)	
	a_2	-0.15(7)	
	a_3	0.05(8)	
	a_4	0.00(9)	
	b_1	-0.03(4)	
	b_2	0.32(3)	
	b_3	-0.01(3)	
	b_4	0.00(3)	

Table D-1 Continued.

E_n (MeV)		---Legendre Coefficients--- E1-E2	E1-E2-M1
9.2	a_1	0.01(3)	0.01(3)
	a_2	-0.61(7)	-0.60(7)
	a_3	0.05(7)	0.06(7)
	a_4	-0.01(8)	0.00(8)
	b_1	-0.12(6)	-0.13(6)
	b_2	0.19(6)	0.18(6)
	b_3	0.02(5)	0.00(5)
	b_4	0.00(5)	0.00(5)
10.2	a_1	-0.05(3)	-0.07(3)
	a_2	-0.60(5)	-0.61(5)
	a_3	0.16(5)	0.02(5)
	a_4	-0.02(7)	0.00(7)
	b_1	-0.21(5)	-0.24(5)
	b_2	0.22(3)	0.23(3)
	b_3	0.03(3)	0.00(3)
	b_4	0.00(3)	0.00(3)

Table D-1 Continued.

E_n (MeV)		——Legendre Coefficients—— E1-E2	E1-E2-M1
11.	a_1	-0.10(2)	
	a_2	-0.63(4)	
	a_3	0.07(4)	
	a_4	0.00(6)	
	b_1	-0.03(3)	
	b_2	0.19(2)	
	b_3	0.00(2)	
	b_4	0.00(2)	
12.	a_1	-0.16(4)	
	a_2	-0.81(8)	
	a_3	0.18(7)	
	a_4	-0.01(9)	
	b_1	-0.07(6)	
	b_2	0.22(6)	
	b_3	0.00(6)	
	b_4	0.00(6)	

APPENDIX E COMPARISON TO THEORY

Table E-1 The weighted means and standard deviations of the E1 absorptive strength distribution of the $^{13}C(n,\gamma_0)^{14}C$ reaction.

Source	$\bar{E}_\gamma$ (MeV)	ΔE_γ (MeV)
Kissner [Kiss73]	15.8	1.2
Vergados [Verg75]	17.3	1.7
Observed	16.3	2.0

Table E-2 Direct-Semidirect Model Parameters used to fit the $^{13}C(n_{pol},\gamma_0)^{14}C$ data.

Potential Parameters Used to Generate the

Continuum Wave Function [Wats69]:

Real Well:

$$V = 60.0 - 27\,\frac{N-Z}{A} - 0.3\,E_{c.m.}\ \text{MeV}$$

$r = 1.14$ fm

$a = 0.57$ fm

Imaginary Surface:

$$W_s = W_s(E) - 10\,\frac{N-Z}{A}\ \text{MeV}$$

$$W_s(E) = \begin{cases} 0.64\,E_{c.m.}; & E_{c.m.} \leq 13.8\ \text{MeV} \\ 9.60 - 0.06\,E_{c.m.}; & E_{c.m.} > 13.8\ \text{MeV} \end{cases}$$

$r = 1.14$ fm

$a = 0.50$ fm

Spin Orbit

$V_{so} = 5.5$ MeV

$r = 1.14$ fm

$a = 0.57$ fm

Table E-2 Continued.

Coulomb Radius: $r_c = 1.14$ fm

Potential Parameters Used to Generate the

Bound State Wave Function:

$V = 53.1$ MeV at $E_n = 11.0$ MeV

$E_B = -8.2$ MeV

$r = 1.14$ fm

$a = 0.57$ fm

$V_{so} = 5.5$ MeV

$C^2S = 1.7$ (Spectroscopic Factor)

Effective Charges:

$$\varepsilon_1 = \frac{-Z_t}{1 + A_t} = -0.43$$

$$\varepsilon_2 = \frac{Z_t}{(1 + A_t)^2} = 0.03$$

Semidirect Form Factors:

Electric Dipole:

Isovector Volume Coupling Form Factor:

$V = 80$ MeV [Byrd81]

$r = 1.14$ fm

$a = 0.57$ fm

Table E-2 Continued.

Semidirect Form Factors (continued):

Electric Dipole (continued):

Resonance:

Position: 15.1 MeV 17.7 MeV

Width: 2.0 MeV 2.0 MeV

Fraction of Classical Sum Rule

Strength: 0.35 0.25

Electric Quadrupole:

Isoscalar Volume Coupling Form Factor:

V = 53 MeV

r = 1.14 fm

a = 0.57 fm

Resonance:

Position: 20.0 MeV

Width: 4.0 MeV

Fraction of Energy Weighted Sum Rule

Strength: 0.4

Table E-3 Direct-Semidirect Model Parameters used to fit the $^{13}C(p_{pol},\gamma_1)^{14}N^*$ (0^+ T=1) data.

Potential Parameters Used to Generate the

Continuum Wave Function [Wats69]:

Real Well:

$$V = 60.0 + 0.4\,\frac{Z}{A^{1/3}} + 27\,\frac{N-Z}{A} - 0.3\,E_{c.m.}\ \text{MeV}$$

$r = 1.14$ fm

$a = 0.57$ fm

Imaginary Surface:

$$W_s = W_s(E) + 10\,\frac{N-Z}{A}\ \text{MeV}$$

$$W_s(E) = \begin{cases} 0.64\,E_{c.m.}; & E_{c.m.} \leq 13.8\ \text{MeV} \\ 9.60 - 0.06\,E_{c.m.}; & E_{c.m.} > 13.8\ \text{MeV} \end{cases}$$

$r = 1.14$ fm

$a = 0.50$ fm

Spin Orbit

$V_{so} = 5.5$ MeV

$r = 1.14$ fm

$a = 0.57$ fm

Table E-3 Continued.

Coulomb Radius: $r_c = 1.14$ fm

Potential Parameters Used to Generate the

Bound State Wave Function:

$E_B = -5.3$ MeV

$r = 1.14$ fm

$a = 0.57$ fm

$V_{so} = 5.5$ MeV

$C^2S = 0.85$ (Spectroscopic Factor)

Effective Charges:

$$\varepsilon_1 = \frac{N_t}{1 + A_t} = 0.50$$

$$\varepsilon_2 = \frac{A_t^2 + Z_t}{(1 + A_t)^2} = 0.89$$

Semidirect Form Factors:

Electric Dipole:

Isovector Volume Coupling Form Factor:

$V = 80$ MeV [Byrd81]

$r = 1.14$ fm

$a = 0.57$ fm

Table E-3 Continued.

Semidirect Form Factors (continued):

Electric Dipole (continued):

Resonance:

Position: 16.4 MeV

Width: 14.0 MeV

Fraction of Classical Sum Rule Strength:

2.70

Electric Quadrupole:

Isoscalar Volume Coupling Form Factor:

V = 53 MeV

r = 1.14 fm

a = 0.57 fm

Resonance:

Position: 20.0 MeV

Width: 4.0 MeV

Fraction of Energy Weighted Sum Rule Strength:

0.4
